Eruption dynamics during Plinian eruptions: Insights from the stratigraphic variations of deposit structures and pumice textures of the Minoan eruption (Santorini, Greece) and the Laacher See eruption (East Eifel, Germany)

Dissertation

zur Erlangung des Doktorgrades
der Mathematisch-Naturwissenschaftlichen Fakultät
der Christian-Albrechts-Universität
zu Kiel

Vorgelegt von
Nico-Alexander Urbanski

Kiel, Dezember 2003

Table of contents

Fig. 5.2: Median mass vs. shape parameters formfactor, solidity and elongation. The LST samples with shape parameters comparable to the Minoan shape parameter are labeled with their sample numbers and the corresponding bed in brackets. The gray fields describe the range of LST shape parameters. For all plots power regressions (black line) and correlation coefficients (r2) for all samples are displayed.

Fig. 5.3: Median grain size vs. shape parameters formfactor, solidity and elongation. The LST samples with shape parameters comparable to the Minoan shape parameter are labeled with their sample numbers and the corresponding bed in brackets. The gray fields describe the range of LST shape parameters. For a) and b) the linear regression (black line) and correlation coefficients of all samples are displayed. For c) the regression and correlation coefficients of all samples (0.191), Minoan and MLST samples (0.674) and LLST samples (0.387) are displayed.

Fig.5.4: Processes intended to exert effect on clast shpes and clast surface appearence. On the left side the prosesses are listed that result in more elongated, angular and rough clast shapes, on the right processes that result in more shperical, rounded and smooth clast shapes.

Abstract

The in situ observation of conduit processes as well as eruption dynamics during major Plinian eruptions is still almost impossible, however, understanding these processes is essential to enhance hazard mitigation and risk reduction near active volcanoes. While numerical modeling of transport processes during Plinian eruptions gives insight into the importance of various physical processes, the validation of these models is still rather difficult. Here we set out to reconstruct the conditions in the conduit during Plinian eruptions through a detailed analysis of the fall deposits of two major Plinian eruptions (Minoan eruption as the chemically homogeneous and the Plinian phases of the Laacher See eruption (LLST and MLST-B/C) as chemically heterogeneous endmember) focussing on the stratigraphic variation of deposit structures (granulometry, modal composition, clast shape parameters) and pumice textures (clast density, permeability, vesicle size distribution) in combination with chemical data and intensive parameters. Changes in the aforementioned parameters reflect changing transport conditions like the granulometric data of the fall deposit being an indicator for fragmentation and eruption intensity or the acceleration of the melt being controlled by degassing that is mirrored in the pumice density and vesicle size distribution.

Based on the detailed analysis of the deposit structure and pumice texture the Minoan eruption can be subdivided into three dynamically distinct phases. The **first phase** (opening phase) started with a decompression event, triggering a first nucleation event. The entire phase was characterized by elevated shear-intensity and degassing while the mass eruption rate and eruption column height increased. The pumice textures (vesicle size distribution and pumice density) indicate that the ascent velocity increased during this phase, resulting in a supersaturation of the melt that caused a second nucleation event in the conduit. Early in the **second phase** we observe a brief decline of the eruption column height, of the mass eruption rate, of the ascent velocity and of the degree of degassing that was preceded by an increased fragmentation intensity and a drop in viscosity at the fragmentation horizon that occurred during the transition from phase 1 to phase 2. After this intermittent period early in phase 2 all parameters listed above increased again and degassing reached a steady state until the end of the Plinian eruption. During the **third phase** a significant increase of both andesitic scoria and hydrothermally altered lithic clasts is observed in the erupted mixture indicating an increasing influence of the andesitic melt component on conduit flow and eruption dynamics as well as enhanced conduit erosion. Both effects led to an increasing fragmentation intensity and to shattering of the edifice, while eruption column height, viscosity and shear intensity decreased. Shattering the edifice opened up pathways for water that started entering the

conduit thereby initiating the transition to the following MIN-B phase of phreatomagmatic explosions.

The Laacher See eruption and deposit are more complicated as the eruption is fed from a chemically zoned magma chamber with frequent phreatomagmatic, ash flow phases interrupting the Plinian phases. The first Plinian phase was the **LLST** phase, characterized by high shear intensity and degree of degassing throughout the entire phase and a collapse event at its end. Further the erupted magma represented the volatile enriched and felsic cupola of the magma chamber. The following eruption phase (MLST-A) was characterized by phreatomagmatic pulses and Plinian fallout and was followed by a phase of intense ash flow eruption (onset of MLST-B). Thereafter the next Plinian phase established during The **MLST-B** phase, characterized by an oscillating eruption column and repeated partial eruption column collapses and ash flows and corresponding coignimbrite ashes incorporated in the fall deposit. The instability of this phase was caused by a decreasing pre-eruptive water content and degree of degassing resulting in mass eruption rates close to the transition of sustained to collapsing eruption columns. This phase merged into the next **MLST-C** phase, characterized by a successive increase in banded and dense gray pumice. This change of the dominant pumice clast composition was caused both by tapping less evolved regions of the magma reservoir and an increase in water-magma interaction that took place in the conduit. These changes were accompanied by an oscillating eruption column and eruption of ash flows during the latest MLST-C phase (C3). The fluctuations of the eruption column height was influenced by the admixing ratio of the less evolved magma and the access of water into the conduit that altered the conduit flow. Based on the deposit structure and the dense pumice clasts distribution this phase is interpreted to have marked a transition from Plinian to phreatoplinian eruption style.

The data collected by means of various methods and their simultaneous interpretation demonstrates that deposit structure and pumice texture are indeed a powerful tool to constrain and reconstruct the temporal variation of conduit flow and eruption dynamics during major Plinian eruptions. It was found that the chemically homogeneous deposits are much easier to invert for conduit flow processes and eruptions dynamics because viscosity is a major factor controlling transport properties of the melt. With the viscosity being fixed parameters like conduit geometry, or shifting of the fragmentation horizon can be constrained much better.

Combing the clast shape parameter and the median of the pumice grain size distributions respectively pumice clast mass data from both eruptions some interesting and new insight

can be gained into the interpretation of clast shape parameters. Clast shape parameters are commonly interpreted as a measure of the shear intensity in the conduit. The linear trends displayed by both eruptions in plots of median vs. shape parameter indicate that the clast shapes are affected by additional processes after the fragmentation of the magma. Combining the shape parameters with results of conduit flow models and characteristics of the corresponding deposits points towards a clast shape dependence on the fragmentation level height in the conduit, average mass of juvenile clasts and amount of lithic clasts erupted.

Zusammenfassung

Plinianische Eruptionen in dicht besiedelten Gebieten der Erde zählen zu den größten bekannten Naturkatastrophen und ein nachhaltiger Schutz von Menschenleben und wirtschaftlichen Gütern vor dieser Naturgefahr erfordert ein genaues Verständnis der Eruptionsdynamik. Leider ist bis heute eine *in situ* Beobachtung plinianischer Eruptionen nahezu unmöglich, aber numerische Modelle geben einen gewissen Einblick in Transportprozesse im Schlot und in der Eruptionssäule sowie Aufschluß über die Bedeutung verschiedener physikalischer Prozesse. Eine Bestätigung dieser Modelle ist jedoch schwierig. Daher wurden in dieser Arbeit die Fallablagerungen von zwei verschiedenen Plinianischen Eruptionen (Minoische Eruption als chemisch homogenes Endglied und die Plinianischen Phasen (LLST und MLST-B/C) der Laacher See Eruption als chemisch heterogenes Endglied) detailliert untersucht. Hierbei lag der Schwerpunkt auf der Untersuchung der Veränderungen der Ablagerungsstrukturen (Granulometrie, modale Zusammensetzung, Klastenformen) und der Bimsgefüge (Dichte der Klasten, Permeabilität, Blasengrößenverteilung). Diese Daten wurden mit chemischen Analysen der Ablagerung und der Eruptionssäulenhöhe und Masseneruptionsrate der Eruptionen kombiniert. Die verschiedenen Parameter spiegeln die sich verändernden Transportbedingungen während der Eruption wider: So sind z.B. die granulometrischen Daten der Fallablagerung ein Maß für die Fragmentierungsintensität und die Eruptionssäulenhöhe bzw. Masseneruptionsrate; die Beschleunigung der Schmelze wird von der Entgasung kontrolliert, die sich aus der Dichte und Blasengrößenverteilung der Bimsklasten rekonstruieren läßt.

Die Minoische Eruption kann aufgrund der detaillierten Untersuchung von Ablagerungs-struktur und Bimsgefüge dynamisch in drei Phasen unterteilt werden. Die **erste Phase** (Öffnungsphase) begann mit einem Dekompressionsereignis, welches mit einer ersten Blasennukleationsphase einherging. Die gesamte erste Phase war durch eine erhöhte Scher- und Entgasungsrate, bei gleichzeitiger Zunahme der Eruptionssäulenhöhe und Masseneruptionsrate gekennzeichnet. Die Bimsgefüge (Blasengrößenverteilung und Dichte der Bimse) legen nahe, daß die Aufstiegsgeschwindigkeit während dieser Phase zunahm. Dies führte zu einer Übersättigung der Schmelze und einem zweiten Nukleationsereignis. Zu Beginn der **zweiten Phase** beobachtet man eine Zunahme der Fragmentierungsintensität und Abnahme der Viskosität am Übergang von Phase 1 zu Phase 2. Die Eruptionssäulenhöhe, Masseneruptionsrate, Aufstiegsgeschwindigkeit und Entgasungsrate nahmen danach kurzzeitig ab, um dann jedoch wieder zuzunehmen. Nun stellte sich eine konstante Entgasungsrate ein, die bis zum Ende der Plinianischen Eruption anhielt. Während der **dritten Phase** nahm die Häufigkeit von andesitischen Schlacken und hydrothermal

alterierten Nebengesteinsklasten signifikant zu. Dies deutet auf einen zunehmenden Einfluß der andesitischen Schmelzkomponente und Schloterosionprozessen auf die Eruptions- und Schlotdynamik hin. Es folgte eine weitere Zunahme der Fragmentierungsintensität und der Zerrüttung des Vulkangebäudes, während die Eruptionssäulenhöhe, Viskosität und Scherrate abnahmen. Die Zerrüttung des Vulkangebäudes ermöglichte das Eindringen von Wasser in den Schlot und löste dadurch den Übergang zur nachfolgenden phreatomagmatischen MIN-B Phase aus.

Die Laacher See Eruption und ihre Ablagerungen sind viel komplexer, da die Eruption aus einer chemisch zonierten Magmakammer erfolgte, und die Plinianischen Phasen zudem häufig von phreatomagmatischen Phasen und pyroklastsichen Strömen unterbrochen wurden. Die erste Plinianische Phase war die **LLST** Phase, die durch eine hohe Scher- und Entgasungsrate während der gesamten Phase, sowie einem Kollaps des Schlots, oder des Magmakammerdachs am Ende der Phase gekennzeichnet war. Weiterhin repräsentiert das eruptierte Magma die an Volatilen angereicherte und differenzierte Dachregion der Magmakammer. Die nachfolgende Eruptionsphase (MLST-A) war durch abwechselnde phreatomagmatische Explosionen und Plinianische Eruptionen gekennzeichnet, darauf folgte eine Phase (Anfang von MLST-B), die von Ascheströmen dominiert wurde.Danach begann die nächste Plinianische Phase (**MLST-B)**, die durch eine oszillierende Eruptionssäule gekennzeichnet war, die zudem mehrfach kollabierte. Die dadurch entstandenen Ascheströme bzw. Aschewolken wurden in die Fallablagerung eingebettet. Die Instabilität der Eruptionssäule während dieser Phase wurde von einem abnehmenden Wassergehalt in der Magmakammer und einer abnehmenden Entgasungsrate ausgelöst. Während dieser Phase lag die Masseneruptionsrate nahe am Stabilitätslimit für Plinianische Eruptionssäulen, was die oszillierende und häufig kollabierende Eruptionssäule erklärt. Diese MLST-B Phase ging ohne Unterbrechung in die nachfolgende **MLST-C** Phase über, während der zunehmend gebänderte und dichte, graue Bimse eruptiert wurden. Dieser Wechsel in der dominierenden Bimsklastenzusammensetzung hatte zwei Gründe, erstens die zunehmende Förderung einer weniger differenzierten Schmelze aus tiefer gelegenen Regionen der Magmakammer und zweitens die Zunahme des Wasser-Magma Kontaktes im Schlot. Diese Veränderungen fallen zeitlich mit einer starken Schwankung der Eruptionssäulenhöhe und gegen Ende der MLST-C Phase (C3) mit der Eruption von Ascheströmen zusammen. Die Schwankungen der Eruptionssäulehöhe wurden vom Einmischungsverhältnis der weniger differenzierten Schmelze und dem Zustrom von Wasser in den Schlot beeinflußt. Basierend auf den Ablagerungsstrukturen und der Verteilung der dichten, grauen Bimsklasten, die in dieser Phase auftraten, wird diese als ein Übergang vom Plinianischen zum phreatoplinianischen Eruptionstyp interpretiert.

Die mittels verschiedener Methoden gesammelten Daten und deren gemeinsame Interpretation zeigen, daß Ablagerungsstrukturen und Bimsgefüge tatsächlich ein geeignetes Mittel sind, um die zeitlichen Veränderungen der Schlotströmung und Eruptionsdynamik bei Plinianischen Eruptionen zu rekonstruieren. Vorteilhaft für diese Rekonstruktion ist das Vorhandensein einer chemisch homogenen Ablagerung, aus der sich viel einfacher die Schlotströmungsprozesse und Eruptionsdynamik bestimmen lassen, da die Variabilität der Viskosität ein wesentlicher die Transporteigenschaften der Schmelze kontrollierender Faktor ist. Bleibt die Viskosität mehr oder weniger konstant können Parameter wie Schlotgeometrie, oder Verschiebungen des Fragmentierungshorizontes viel besser bestimmt werden.

Aus der linearen Abhängigkeit der Klastenformparameter von dem Median der Bimskorngrößenverteilungen, bzw. der Masse der Bimsklasten beider Eruptionen lassen sich neue, interessante Erkenntnisse bezüglich der Interpretation von Klastenformen ableiten. Die Klastenform wird oft als ein Maß für die Scherrate im Schlot betrachtet. Die lineare Abhängigkeit des Medians von Klastenformparametern legt nahe, daß die Klastenformen von weiteren postfragmentären Prozessen kontrolliert werden. Die Kombination der Klastenformparameter mit den Ergebnissen numerischer Schlottransportmodelle und den Eigenschaften der entsprechenden Ablagerungen deutet darauf hin, daß die Klastenformen von der Höhe des Fragmentierungshorizontes im Schlot, der mittleren Masse der juvenilen Klasten und dem Anteil der eruptierten Nebengesteinsklasten abhängen.

1. Introduction

Plinian eruptions are the most vigorous and dangerous volcanic eruptions. Commonly these eruption are concentrated along the convergent margins of the lithospheric plates, where evolved and water rich magmas are generated. However, Plinian eruptions occur in intra-plate settings related to hotspots, like oceanic islands (e.g. Canary Islands) or continental intra-plate volcanoes (e.g. Laacher See).

Plinian eruptions are characterized by gas thrust regions and the formation of sustained, convective eruption columns, rising several tens of kilometers up in the atmosphere (up to 35 km; Cioni et al., 2000). Tephra is transported through the convective part of the column into a mushroom shaped umbrella region of the column and dispersed widely around the eruption center. Many Plinian eruptions are accompanied or followed by pyroclastic flows, representing the major threat for in part densely populated areas in the vicinity of explosive volcanoes are. A better understanding of Plinian eruptions is thus of great interest, especially to understand the variation of conduit dynamics and their influence on column evolution and stability.

1.1 Previous work

Magma composition, the amount of dissolved volatile components in the magma and the style of degassing determine the explosivity of volcanic eruptions. One of the most striking evidences for the degassing of a magma during explosive eruptions are the highly vesicular pumice clasts, showing vesicularities up to 90 vol% (Gardner et al., 1996). The process of degassing and vesiculation of magmas can, of course, not be observed directly. Therefore the dynamic processes taking place during ascent of the melt in the conduit are a major topic of research. Relevant processes have been modeled by numerical calculations (e.g. Papale, 1998; Mader, 1998; Jaupart, 2000), analogue experiments (e.g. Mader, 1998; Dingwell, 1998a) and determined from the deposits of these eruptions (e.g. Sparks et al. 1997; Rosi, 1998; Houghton et al., 2000; Jurado-Chichay and Walker, 2001), the main result being that the rising magma goes through three phases of ascent: pre-fragmentation, fragmentation and post-fragmentation (Fig. 1.1).

Pre-fragmentation processes

During rise of a magma from the magma chamber to the fragmentation horizon significant changes take place, especially rapid decompression. This decompression

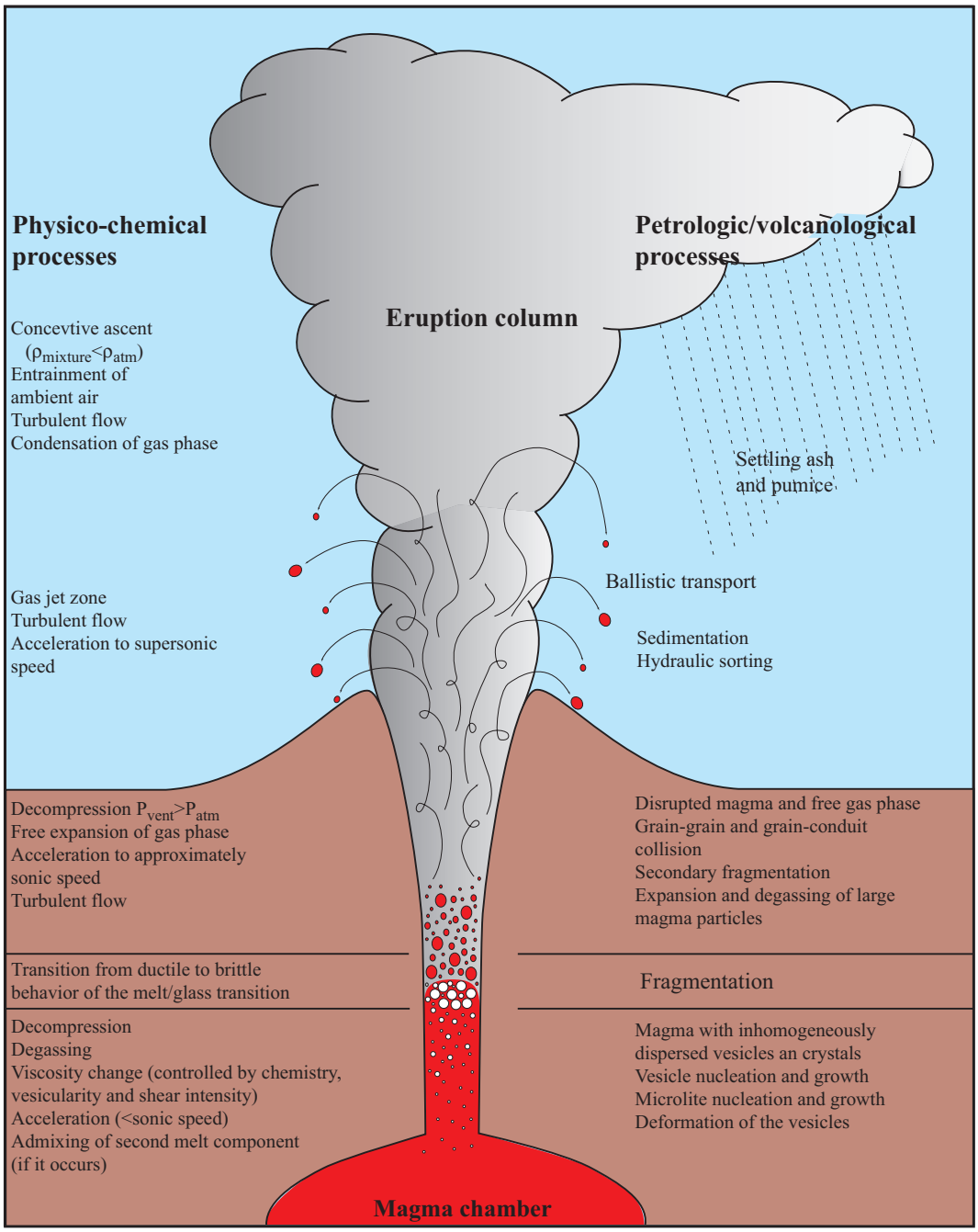

Fig. 1.1: Schematic diagram summarizing the pre fragmentation and post fragmentation processes during a Plinian eruption. On the left side the physico-chemical changes of the melt and mixture are briefly described. On the right the processes that influence the deposits and clast features are summarized.

affects the physico-chemical properties of the melt (e.g. Sparks et al., 1994, Dingwell, 1998a; 1998b).

1. The decompression causes volatile saturation. The volatiles begin to exsolve if the degree of supersaturation is exceeded and vesicles are formed in the melt.
2. Exsolution of gas causes a drop of the liquidus temperature and results in the growth and nucleation of minerals (phenocrysts and microlites).
3. The vesicles in the magma grow by decompression and diffusion.
4. The increase in volume caused by vesicle growth accelerates the melt-vesicle mixture in the conduit.

These physico-chemical changes also affect the rheological properties and the flow dynamics in the conduit. Degassing and vesiculation changes the viscosity of the melt-vesicle mixture. Loss of volatiles results in a viscosity increase (Sparks et al., 1994). Vesicles up to 50 vol% result in a lower viscosity (e.g. e.g. Bagdassarov and Dingwell, 1992; 1993; Manga and Loewenberg, 2001; Llevellin et al. 2002). Shear rate significantly influences the viscosity of vesicle-bearing melts, because vesicles loose their capability to deform if the strain rate exceeds the relaxation time of the melt, and therefore increase the viscosity (Dingwell, 1997; 1998b).

Numerical models are applied to gain insights in the conduit flow processes. These models are mainly based on conservation equations (continuity, energy and momentum) and equations describing the physical parameters of the melt. The resulting models can be separated into two essential approaches

1. A system of equations describing the growth of a single bubble in a defined sphere of influence (Sparks ,1978; Bottinga & Javoy, 1990; Proussevitch et al., 1994; Barclay et al., 1995; Toramaru , 1995; Proussevitch and Sahagian, 1996).
2. One-dimensional, steady-state, isothermal flow models of a homogeneous fluid with Newtonian viscosity, rising in a vertical conduit with constant diameter under a lithostatic pressure gradient. (Wilson et al., 1980; Buresti and Casarosa, 1989; Mastin and Ghiorso, 2000).

The latter kind of models were improved to a second generation of steady-state, non-homogeneous models that involve thermal and mechanical differences between the different phases, velocity and viscosity changes along the conduit and the non-isothermal conditions in the conduit (Vergniolle and Jaupart, 1986; Dobran, 1992; Papale and Dobran, 1994). Unsteady homogeneous models focus on the temporal variations of eruption dynamics and take time-dependent transport equations into account (Turcotte et al., 1990; Alidibirov, 1994; Ramos, 1995). The most recent models combine both the steady and unsteady approach and result in multiple solutions for the same set of conditions, explaining sudden variations of eruption intensity in explosive eruptions (Melnik, 2000; Slezin, 2003). All models result in a set of solutions that describe the physical parameters at the conduit outlet (e.g. ejection speed, mass eruption rate) and their variation in dependence of the starting parameters of the eruption. A further change common during large Plinian eruptions is the mixing of two melts of different viscosity in the conduit, also altering the conduit flow regime significantly (Freundt and Tait, 1986). Chemical gradients in magma chambers also influence the conduit and eruption dynamics as well as changes in conduit diameter and syn-eruptive water content (e.g. Wilson, 1980; Wilson et al. 1980; Neri et al., 1998, Papale et al. 1998, Papale and Polacci, 1999).

Fragmentation processes

The fragmentation of the ascending melt is the most dramatic change that takes place in the conduit. It marks the transition from a continuous one-phase flow regime of the magma (melt, vesicles and crystals) to a two-phase flow of disrupted melt fragments dispersed in a gas jet that is confined in the conduit. The fragmentation is accompanied by a drastic decrease of viscosity, approximating the viscosity of the gas phase, size dependent quenching of the majority of the clasts generated and expansion of the gas phase, resulting in an acceleration of the gas-melt mixture.

The process of fragmentation has to be modeled both with analogue and numerical approaches. The analogue models focus on the clast populations generated by fragmentation processes (e.g. Kaminski and Jaupart, 1998; Martel et al., 2000; 2001), or try to simulate fragmentation models with analogue material (e.g. Mader et al., 1994; Alidibirov and Panov, 1998). The numerical models distinguish four possible fragmentation mechanisms (Fig. 1.2).

1. The model of Sparks (1978) predicts that a melt that contains ~75 vol% vesicles disrupts because of melt film thinning.
2. Mungall et al. (1996) proposed that the degassing of a melt leads an expansion of the vesicle walls resulting in microfractures that lead to the disruption of the foamed magma in combination with the overpressure inside of the vesicle.
3. Alidibirov (1994) suggests that a fragmentation wave propagates downward into the conduit filled with an almost or entirely solidified magma. This fragmentation wave is triggered by a decompression event (like collapse of a lava dome) leading to an increasing pressure difference along the vesicle walls that mechanically fail when their strain resistance is exceeded.
4. Papale (1999) focuses on a strain-induced fragmentation criterion, which is achieved when the strain rate exceeds the relaxation time of the melt. In this case the glass transition is achieved and the result is a brittle failure of the vesicle walls.

The four models point towards the most important question concerning fragmentation. Is the fragmentation process taking place under ductile or brittle conditions? The first model (Sparks, 1978) is the only one that applies to purely ductile conditions, but also inherits a basic problem of inconsistency of models and observations, because most pumices show a wider range of vesicularity (Gardner et al., 1996; Melnik, 1999) than assumed by the model of Sparks (1978). The other three models are representing a brittle fragmentation (Alidibirov, 1994; Papale, 1999) or a mixture of brittle and ductile fragmentation (Mungall et al., 1996). Whether brittle or ductile fragmentation is taking place during Plinian eruptions is still unknown. Intense studies of the deposits of Plinian eruptions and

the textures of their pumice clasts can reveal information about the kind of fragmentation. Only a few studies tried to decipher the fragmentation process (and conduit dynamics) from the deposits and pumice textures (e.g. Klug and Cashman, 1996; Gardner et al., 1996, Gardner et al. 1998; Polacci et al., 2001; Klug et al., 2002). Many studies focussed on the distinction of magmatic and phreatomagmatic fragmentation (e.g. Dellino et al., 2001; Mastrolorenzo et al. 2001).

Post fragmentation processes

After the fragmentation the gas-melt mixture accelerates in the conduit and undergoes

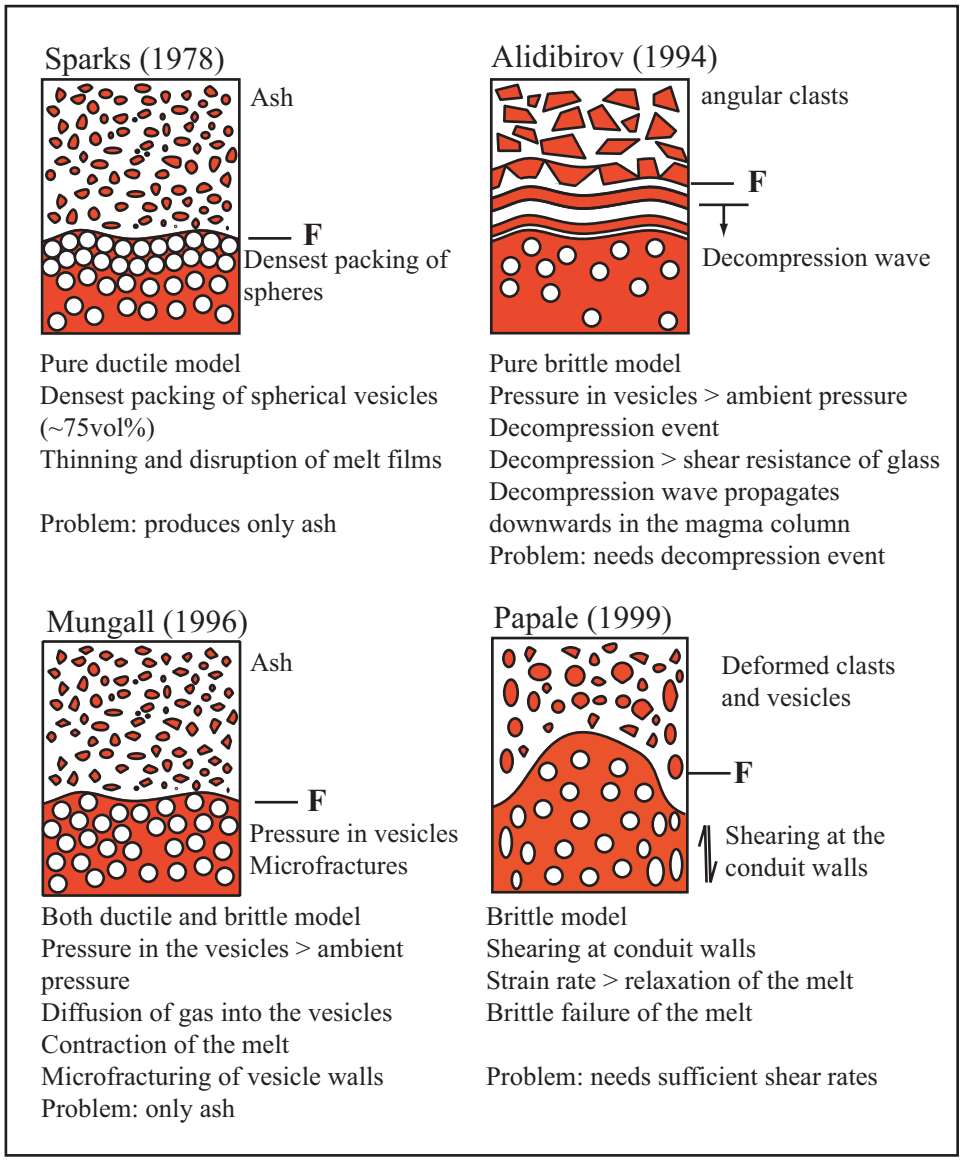

Fig. 1.2: Schematic sketch of the four fragmentation models described in the text, with their main features and problems described. **F** marks the fragmentation level.

further expansion while it is decompressed to nearly atmospheric pressure at the conduit exit (Kaminski and Jaupart, 1997). At the conduit exit the speed commonly reaches the local sonic speed (so-called choked flow condition) of the gas-particle mixture and a jet that enters the atmosphere is generated. The hot expanding mixture entrains ambient air

lowering the density of the eruptive jet. Given that this process is effective enough the erupted material starts to rise convectively into the atmosphere (eruption column density < atmospheric density), reaching several tens of kilometers in height until the mixture density equals the density of the atmosphere (neutral buoyancy). At this point the tephra spreads laterally in an umbrella shaped region. Settling processes begin and tephra is deposited over large areas (e.g. Sparks et al. 1997, Carey and Bursik, 2000). The distribution of the tephra is significantly influenced by the prevailing winds in the atmospheric layers penetrated by the eruption column (Carey and Sparks, 1986). Several eruption parameters can be deduced from the resulting fall deposits. The major parameters are eruption column height (maximum clast size), volume of erupted tephra and mass eruption rate (e.g. Rosi, 1998).

Though it is assumed that the majority of the clasts generated during fragmentation are quenched instantly larger pumice clasts suffer further degassing and textural alterations in the eruption column (e.g. Kaminski and Jaupart, 1997; Tait et al., 1998; Hort and Gardner, 1999). Further the collision of the particles in the turbulent flow enhances a secondary fragmentation of the brittle clasts, slightly altering the size distribution of the clast population generated at the fragmentation level (Kaminski and Jaupart, 1998).

1.2 Aims of the study

The melt goes through a textural maturation and development during these three aforementioned phases which can be observed in the textures of resulting pumice clasts. Therefore the examination of the stratigraphic changes of pumice textures (respectively the temporal change during the eruption) is an unique method to compile information on the temporal change of the dynamic processes during a Plinian eruption. Therefore, the aim of this study is to carry out a combined investigation of textural, physical and chemical characteristics of pumice clasts (vesicle size distributions, clast shape parameters, density, permeability) and structural features of the deposit (grain-size distribution (GSD), maximum clast size, modal composition). For all features their stratigraphic variation is determined. This combination of different datasets has not been applied that detailed to Plinian fall deposits yet. This helps to achieve information about the processes controlling the eruptions dynamics and what parameters may be responsible for significant dynamic changes (e.g. leading to column collapses). This results in a better hazard assessment for densely populated volcanic regions and enhances the opportunity to predict the behavior of Plinian eruption columns during an eruption.

The two deposits investigated in this study are the Plinian phase A of the Minoan eruption, Santorin (Greece) and fallout sequences of the Laacher See eruption, East-Eifel (Germany). The two deposits were chosen because they differ in chemical composition and the chemical homogeneity of the melt erupted. Therefore they reflect two endmembers concerning the chemical zonation of the magma chamber (Laacher See eruption reflecting the well zoned type and the Minoan eruption the homogeneous type). Thus the control of chemical composition on the conduit processes may be deciphered from the different datasets derived from the two deposits. Further the datasets can provide information on how fragmentation takes place under special conditions in the conduit and which physical model maybe closest to the natural processes.

2. Methods applied in this study

Maximum clast size

During field work on Santorini and in the East Eifel, next to the sampling, the maximum clast size (MCS) was determined by quantifying the long axis for 3 to 5 distinct pumice and lithic clasts for each stage. The stages were defined on Santorini by separating the deposit in ten equal portions at three different localities, where the MCS variations were determined. In the East Eifel the stages were defined based on the deposit structures in a pumice pit south of Nickenich and represent single beds. The MCS variation of the Laacher See deposit was determined only at this locality. The mean MCS was calculated and standard deviation was taken as mean error for the average values.

Grain size distribution

The grain size distribution (GSD) was determined by wet sieving of the fall deposits bulk samples. The grain-size ranges of >32 mm to 0.063 mm were separated and weighted. The grain-size distributions are shown for each section in the data graphs. The GSD data was also used to determine median and sorting of each stage.

Modal composition

The modal compositions were either determined by counting the distinct clast types in the outcrop or by estimating the volume percentages of each bed (see Appendix; only applied for LST in the Nickenich pit). In the latter case only percentage ranges were determined (e.g. 1- 5 %). The field data of modal composition are therefore imprecise and weight percentages of the different clast types for each stage were determined later for the essential lapilli size ranges by hand picking and weighting each modal fraction. These data are taken into account for the variation of modes during the Plinian phases of Santorini and Laacher See volcano. The modal data was used to generate the combined GSD and pumice GSD data sets, and the median and sorting coefficient of the latter.

Density

The densities were determined for the essential lapilli size range (32-16 mm) of the different pumice types by the Archimedes method. The clasts were first weighted and then sealed by evacuation and welding them in plastic foil. Then the sealed clasts were dipped in a water basin and the displaced amount of water was weighted to evaluate the volume of the sealed clasts. This procedure was repeated five times per clast. The volume of the foil was determined by its known thickness and size of the plastic foil used for each clast. The densities were determined for up to 10 clasts of each type and stage (if

enough clasts were available). For the Laacher See sequence also weighted average densities were calculated based on the modal abundance of the juvenile components.

Permeability

The permeability of selected clasts was determined with a simple method used for the permeability determination of soil samples in the Institute of Soil Science and Plant Nutrition at the CAU, Kiel (Fig. 2.1). The permeability measurements were carried out with cores drilled out of pumice bombs and larger pumice clasts (>32-16 mm). Two core sizes were drilled depending on the clast size. The larger cores are 40 mm in diameter and the smaller ones 25 mm. The cores were wrapped with plastic foil, fixed in plastic tubes and sealed with silicone, to avoid air flowing around the sample. The sample is closely fixed in the sample holder and pressurized air flows through the sample. The flow rates are measured by a set of flowmeters and the pressure exerted on the sample is measured with a water filled pipette connected to the base of the sample. The data (pressure at the sample base, flow rates, sample mean length and sample surface) were used to calculate the K_L value using the following equation (Institute of Soil Science and Plant Nutrition staff, pers. comm.): $K_L = \rho_l * g *(\Delta V * l / \Delta t * \Delta p * A)$, where ρ_l is the density of the ambient air, g is the gravitational acceleration, ΔV is the volume of air flown through the sample during the time Δt, l is the length of the sample core, A is the surface of the sample core, and Δp is the pressure difference across the sample. The resulting K_L has an unit of m s^{-1}. To get the K_0 [m^2] a derivation the Darcy equation: $K_0 = K_L * (\eta_l * (\rho_l/g))$ was applied, where η_l is the viscosity of air at ambient temperature.

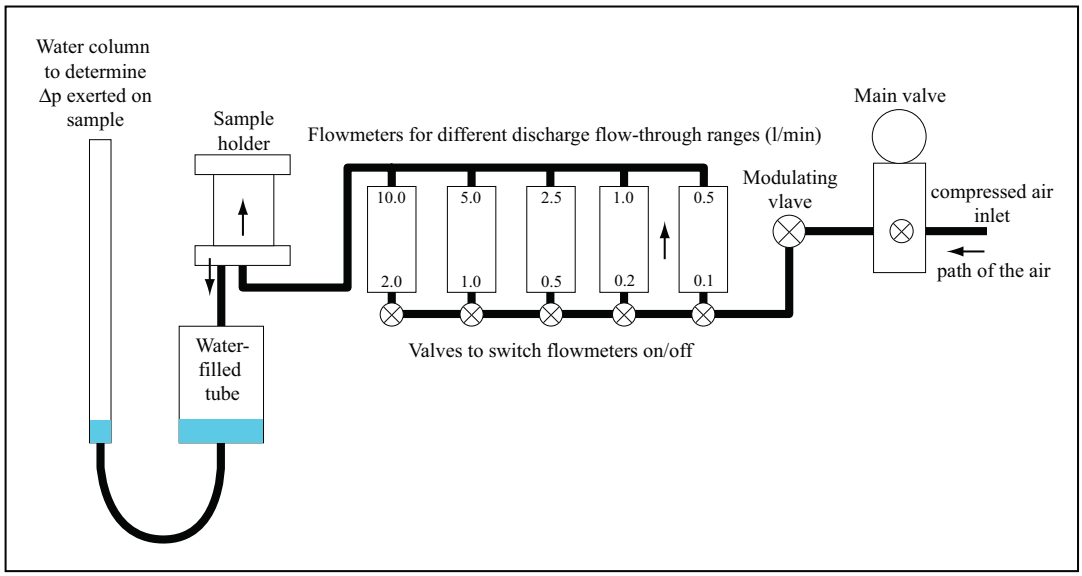

Fig. 2.1: Setup of the permeameter of the Institute of soil science and plant nutrition at the CAU, Kiel that was applied for the permeability measurements.

Chemical analyses and viscosity calculations

Whole rock analyses of major (SiO_2, TiO_2, Al_2O_3, Fe_2O_3, MnO, MgO, CaO, Na_2O, K_2O, P_2O_5) and trace elements (Ba, Co, Cr, Ce, La, Nb, Ga, Pb, Pr, Rb, Sr, Th, V, Y, Zr, Zn, Ni) were carried out by XRF (Phillips PW 1480). H_2O and CO_2 were analyzed with IR-Photometer (Rosemount CSA 5003). The fresh pumice samples were hand picked from the 2-1 mm size fraction and ground in an agate mortar. The fresh and not pumice contaminated mafic scoria samples were hand picked from all size ranges and ground in planetary mill (Fritsch Pulverisette). Based on the chemical analyses the viscosity was calculated (Shaw, 1972). For this calculations an Excel spreadsheet by courtesy of A. Freundt was apllied.

Clast shape analyses

The clast shape analysis were carried out at digital images of at least 70 single clasts per sample. The images were taken with a Polaroid digital camera (DMC 1) mounted on a Leica MZ8 Stereomicroscope. The gained digital images were processed using professional image processing software (Photoshop 5.5 and 6.0), by applying an unsharp mask filter and increasing the contrast of the image. The resulting images were processed further by hand to erase the shadows of the particles in the processed images. These images were analyzed with the DIAna Image analyses software to determine the particles parameters (area, circumference, long axis, short axis and convex envelope) needed to calculate the shape parameters formfactor, solidity and elongation.

Pumice textures

The pumice texture data (vesicle distribution data) were gained from carbon coated thin sections of 32-16 mm sized pumice clasts with known density. The thin section images were captured with a CamScan CS24 SEM. The BSE images were taken with 15 kV and 1.96 A. Of each thin section images were taken with both 25x and 100x magnification. The single images were combined for each magnification to a patchwork image covering 7.4×10^7 and 2.2×10^8 μm^2 for the 25x magnification and the 100x magnification images representing a part of this area. The patchwork images were processed with a professional image processing software and the vesicle walls were redrawn by hand to enhance the contrast and enabling threshold capturing with NIH java applet image analyses software. The threshold images (8-bit; black and white) were analyzed with the DIAna image analyses software to retrieve the vesicle parameters (area, circumference). The area data was used to calculate equivalent diameters and corresponding vesicle volumes, assuming perfect spherical shape. These data and the count numbers were used to generate volume

distribution plots, cumulative number density plots and to deduce the volume based median variation.

Conduit flow model calculations

Conduit flow model calculations were carried out by using the conflow freeware program of Mastin and Ghiorso (2000). The input parameters (conduit diameters, initial speed, input pressure, and depth) were constant for each eruption. The magma composition settings (major element composition, pre-eruptive volatile content, phenocryst content, and temperature) were taken from the chemical compositions described in the corresponding sections and shown in the appendix. A specified pressure gradient was applied for the calculations.

3. Minoan Eruption

The Minoan eruption took place on the Aegean archipelago of Santorini, which consists of two major (Thera and Therasia) and three minor islands (Aspronisi, Nea and Palaea Kameni). The archipelago is located on the continental Aegaen microplate, mainly consisting of alpine metamorphic rocks and several granitoid intrusions (Druitt et al. 1999). The large scale tectonic setting is dominated by extension, southwestward motion of the Aegean plate and subduction of the African plate in northeasterly direction beneath the European plate (Jackson, 1994). The Hellenic trench system, associated with the subduction, has two main branches and strikes NW-SE southwest off Greece (Peleponnes) and Crete. Also associated with the subduction is the Aegaean volcanic arc spreading from the Greek mainland to the east toward Kos close to Turkey, with Santorini being almost in the center of the arc. The volcanic centers of the arc are closely associated with 5 NE-SW-striking rupture zones (Papazachos and Panagiotopoulos, 1993). The predominating rock types of the arc volcanoes are andesite to dacite. Basalt and rhyolites occur especially in the eastern part of the arc. The rocks are mainly calc-alkaline, with high Al_2O_3 and medium to high K_2O content (Innocenti et al., 1981).

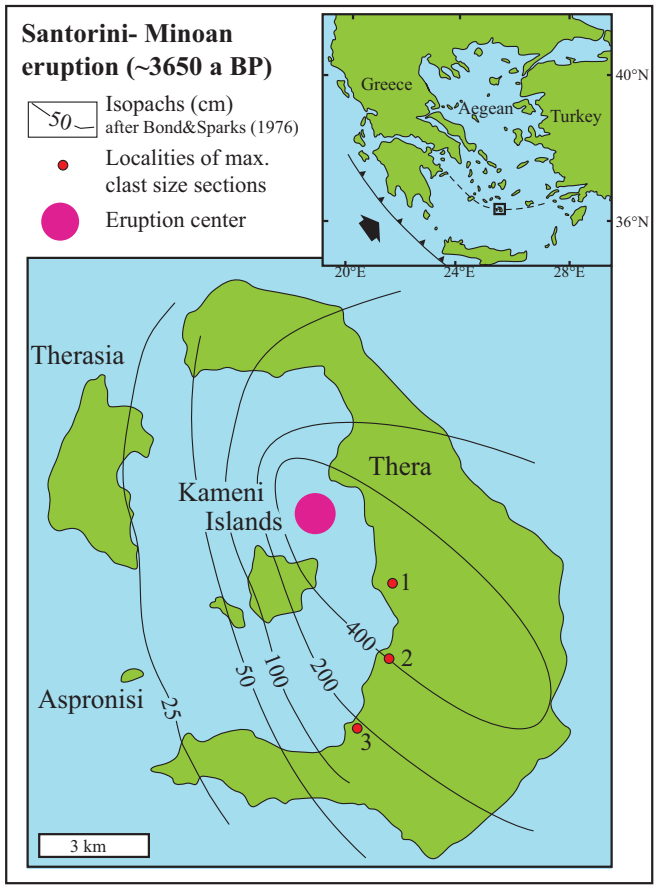

Fig. 3.1: Map of Santorini with isopachs of Plinian fallout, localities of the max. clast size sections and assumed eruption center.

Santorini is one of the largest volcanic centers of the Aegean arc. The two major islands of the archipelago form a dissected ring around the flooded caldera, in which lie the young, still active volcanic centers of Palaea and Nea Kameni. The volcanic field of Santorini has been active since mid-Pleistocene times (650 ka; Druitt et al. 1999) and was the site of repeated explosive volcanic eruptions until recent times. The more than 200 m thick sequence of pyroclastic deposits is more or less entirely exposed at the caldera walls, surrounding the central basin. The succession was deposited by 12 major and many

minor explosive eruptions, subdivided into two major cycles (Druitt et al., 1989), based on long-term changes in magma composition. At least four major explosive eruptions were accompanied by caldera collapse and formed the recent composite structure of the caldera, consisting of four basins (Druitt and Francaviglia, 1992). The repeated collapses dissected the deposits of the 12 major explosive eruptions and remains of ancient lava dome complexes, shield- and stratovolcanoes.

The Minoan eruption is the most famous of these eruptions and took place in the late bronze age, namely in the 17^{th} or 16^{th} century BC. The exact age of the eruption is still not determined precisely and the different ages were determined by either 1) archeological methods ranging from 1450 to 1500 BC , 2) radiocarbon dating indicating ages younger than 1650 BC (Friedrich et al., 1990), 3) an ice core sulphuric acid peak from South Greenland, that can be correlated with the Minoan eruption and is dated at 1645±20 BC (Hammer et al., 1987) and 4) frost damage in Irish and Californian trees dated to 1627±2 BC representing a climactic eruption that took place a year before (LaMarche and Hirschboeck, 1984; Baille and Munroe, 1988).

The rhyodacitic products of the eruption display no significant chemical and mineralogical variation. The eruption itself took place from a shallow, flooded caldera, with a central island comparable to the recent central Island. Abundant dacitic hyaloclastite blocks may represent the edifice of the former intracaldera volcano and stromatolitic blocks dispersed over the northern part of Thera are evidence for a shallow water environment surrounding the central island (e.g. Druitt and Francaviglia 1992).

Precursory activity took place in form of phreatic explosions, covering southeastern Thera with a dm thick ash layer (~10^6 m^3; Heiken and McCoy, 1984). The fact that the deposit exists throughout SE Thera, but is missing in the streets of the former city of Akrotiri, may be evidence that the precursory activity occurred prior to the main eruption long enough for the Minoan inhabitants of Akrotiri to clean the streets and leaving the island in time. This scenario would also explain the absence of human skeletons.

The main eruption has been subdivided into four phases (Bond and Sparks, 1976), starting with a Plinian phase from a subaerial vent, about 1.5 km west of Thera near Nea Kameni in the present caldera. The eruption column reached a maximum height of about 36 km and a peak discharge rate of $2.5x10^8$ kg s^{-1} and 2 km^3 magma DRE ($4x10^{12}$ kg) erupted (Sigurdsson et al., 1990). The erupted tephra was dispersed to the southeast by the prevailing winds; the deposits (Minoan A) occur throughout the archipelago with a thickness of up to 6 m. The

Fig. 3.2: Photos of the sample locality and the three maximum clast size profile localities. A: Phira Quarry and caldera rim, B: Sample and profile locality in the Phira Quarry, C: Cape Athinios profile locality, D: Cape Therma profile locality and E: Overview of Cape Therma Quarry. The units on the scale are 10 cm.

fallout deposit is slightly compositionally zoned, with andesitic blebs increasing upward in abundance. The initial phase ended with a first intrusion of water into the vent region and the resulting deposit (so called phreatomagmatic break) at the top of Minoan A that shortly interrupted the fallout deposition. This water-magma interaction continued during phase 2 of the eruption, which was characterized by large scale water access to the vent and multiple

vigorous phreatomagmatic eruptions and the emplacement of surge deposits, up to 12 m thick (Minoan B). The water ingress into the vent possibly marked the beginning subsidence of the caldera, increasing the fracturing of the vent region and successive destruction of the central volcano. Deposition from the Plinian eruption column continued, because thin fallout beds are interlayered with the cross-bedded surge deposits. The deposits of phase 3 are massive tuffs with up to 10 m large hyaloclastite blocks. They are interpreted as the products of hot (≤300°C; Druitt et al., 1999) water-rich debris flows that "boiled" over the caldera rim. The deposit (Minoan C) is up to 55 m thick at the caldera rim and wedges out rapidly. Phase 4 erupted hot (300- 350°C; Druitt et al., 1999) pyroclastic flows, covering the entire archipelago and building an apron all around the outer coastline of Thera and Therasia. Here the deposits (Minoan D) are up to 40 m thick and contain segregation pipes and interstratified coarse-grained lag breccias in the ignimbrite. The ignimbrite is covered in a few locations by fluvial gravel caused by flash-floods following the eruption, either caused by heavy rainfall or tsunamis generated by caldera collapse. The eruption discharged about 30 km³ rhyodacitic magma, with the bulk represented as ignimbrites (Pyle, 1990).

This study focusses exclusively on the Minoan A fall deposit, sampled in detail at a location in Phira quarry. The deposit was divided into 10 intervals of equal thickness (labeled as stages) that were individually sampled and are represented by the samples MIN-A/SE1a to SE1j.

3.1. Results

3.1.1. Granulometric data

Maximum clast size

In the field the maximum clast size (MCS) variations for pumice and lithic clasts were determined at three locations on Thera (Phira Quarry, Cape Athinios and Cape Therma; locations see Figs. 3.1 and 3.2). These data (Fig. 3.3) show a consistent increase in the average size in the lower part followed by a decrease toward the phreatomagmatic break for both pumice and lithoclasts. Because the three profiles differ in detail they are described below.

Profile 1, Phira Quarry: The most proximal profile displays an increase of both pumice and lithic MCS over the lowermost four stratigraphic intervals (for pumice from 11.6 to 21.1 cm and lithics from 3.9 to 10.3 cm). The pumice MCS subsequently decreases to 17.1 cm and

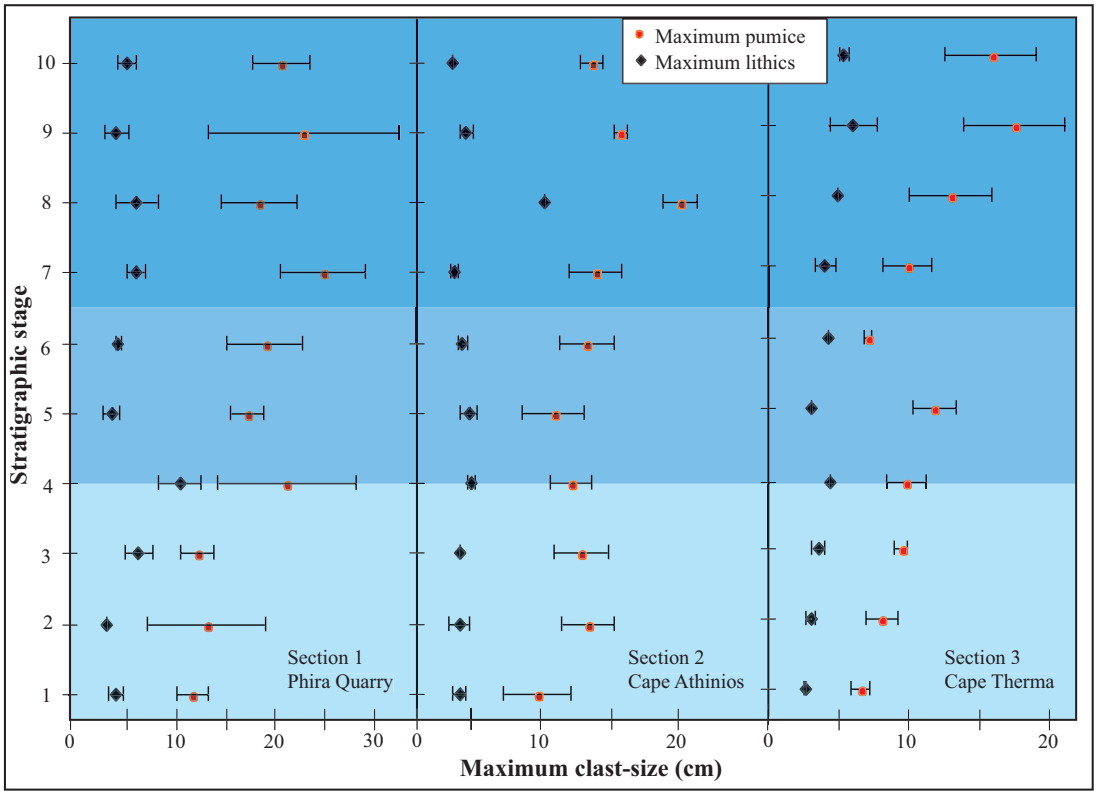

Fig. 3.3: Variation of maximum clast size vs. stratigraphic stage of the three localities. The color coding represents the three eruption phases distinguished in conclusions (see text).

increases above this minimum to the peak size of 24.8 cm at stage seven. From this point on pumice MCS decreases to 20.5 cm. The lithic MCS in contrast is almost invariant with 3.5 to 6 cm.

Profile 2, Cape Athinios: The pumice MCS abruptly increases from 8.5 to 12.1 cm at the second stage and decreases slightly to 9.7 cm at stage five. It increases to the peak size of 18.6 cm at stage eight and finally decreases to 12.4 cm towards the top. The lithic MCS is quite invariant at small sizes (about 2.5 to 3.8 cm) except a single peak size of 9 cm at stage eight.

Profile 3, Cape Therma: In the most distal profile the pumice MCS increases over the five lowermost stages from 6.1 to 11.3 cm. At stage six it decreases to 6.7 cm and subsequently increases again to a peak value of 17 cm at stage nine and decreases towards the topmost stage (15.4 cm). The lithic MCS shows an almost uniform increase from 2.2 cm to the peak size of 5.6 cm with stage nine and a subsequent decrease to 4.9 cm.

Grain size distribution

The grain size distribution (GSD) of the Minoan Plinian fall deposit has been determined for a set of samples taken at Phira Quarry (locality 1) and appears quite uniform (Fig. 3.4). The

Fig. 3.4: Stratigraphic variation of grain size distributions (original and recalculated, see text for details) of samples MIN-A/SE1a to j, representing stratigraphic stages 1 to 10.

size distribution commonly shows a clear peak at Φ –4, being constant in the lower half of the deposit. Sample SE1f shows a marked peak at Φ –5. The uppermost four samples (SE1g to SE1j) show a broader peak extending to phi-grade –3 and oscillating between Φ –3 and -

4. A fines tail successively develops from SE1d/e on next to this more diffuse peak in the distribution of the upper part.

The GSD data were restricted to the size range of Φ –5 to 2 and normalized to 100%, (Fig. 3.4) to emphasize the coarse size range variations already described. In these normalized plots the GSD data are further combined with modal analyses. This way of combined presentation shows that the GSD is significantly influenced by the modal composition of the deposit. Most striking is the peak at Φ –5 of sample SE1f which clearly can be attributed to a single accidental, dacitic lava clast in the sample (by this combined plots). The third column of Fig. 3.4 displays the distribution of the pumice without the lithics, crystal-rich clots and mafic scoria deduced from the combined data and normalized to 100%. The shift from a distinct peak to a broader double peak and the development of the fines tail is well visible in these plots. The oscillation described for the original GSD of the uppermost four samples can be attributed to the lithic component in these samples.

Median and sorting

Median and sorting coefficient (Fig. 3.5) were determined from the cumulative GSD plots of both the original GSD data and the recalculated GSD data, comprising only pumice.

The median of the original GSD first increases from SE1a to SE1e (-4.3 to –3.7) then abruptly decreases to –4.5 for SE1f. After this decrease (also visible in GSD, and caused by a large lava lithic (>32 mm) in the sample) the median increases again for the last samples (SE1g to SE1j) from –3.5 to –3.3, with a minimum of –3.7 in sample SE1i.

The median of the pumice GSD shows three distinct parts. The lowermost part (SE1a to SE1d) is characterized by an increasing median, ranging from –4.4 to –4.2. Then the median jumps to constant value of –4 for two stages (SE1e/f). This is followed by a sharp jump in median to –3.6 with SE1g and a subsequent steady increase of the median to –3.3.

The sorting coefficient of the original GSD resembles the median and increases slowly from 1.08 to 1.68 for SE1a to SE1d. Then it jumps to 3.7 for SE1e to decrease for SE1f to 1.2. The sorting coefficient slightly decreases over the last four samples from 2.7 to 2.5, with a minimum of 1.95 in sample SE1i.

The sorting coefficient of the pumice GSD also displays a threefold separation as observed for the median. Here the lowermost part (SE1a to SE1d) is characterized by a slight increase of sorting coefficient from 0.88 to 1.03. Then the coefficient jumps to 1.35 and stays relatively constant (slight decrease to 1.23) up to SE1g. The uppermost part shows a steady

increase of sorting coefficient to 1.88 with SE1j having jumped prior the increase to a lower value of 1.1 with SE1h.

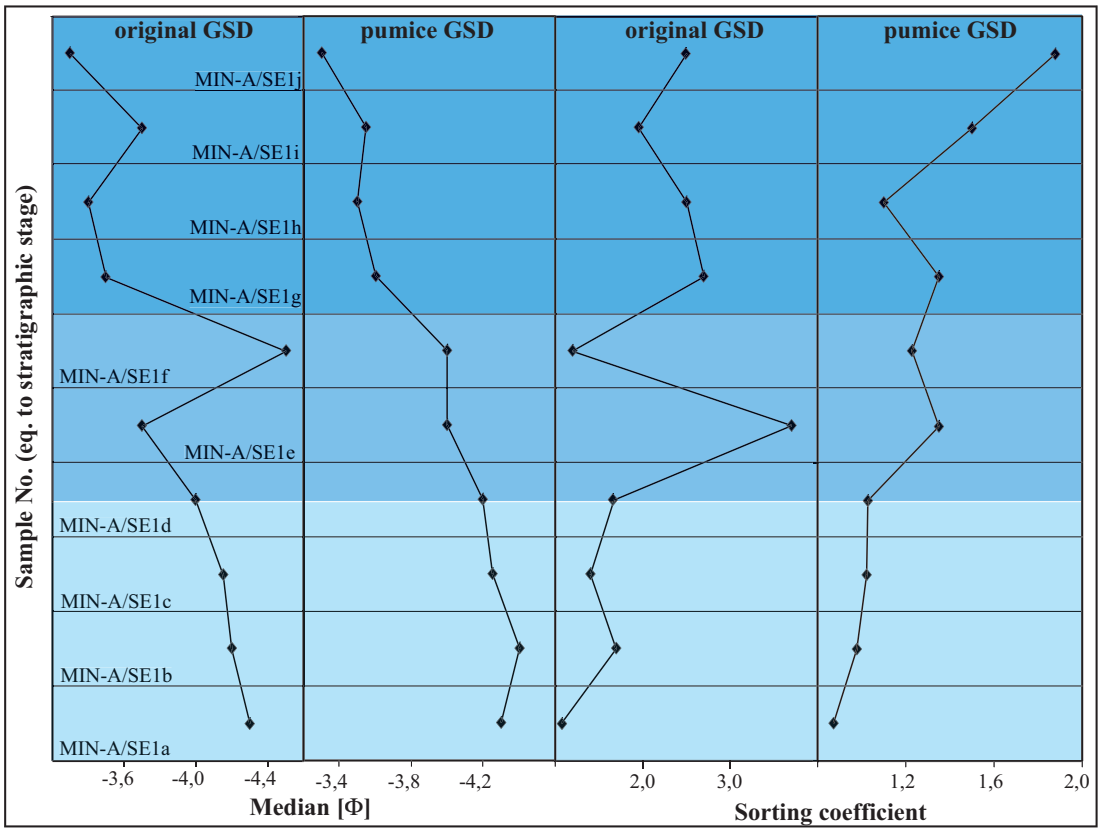

Fig. 3.5: Stratigraphic variation of median and sorting of both original grain size distribution and pumice grain size distribution.

3.1.2. Modal Composition

Modal compositions were determined for the size range >32 mm to 4 mm (Φ grades –5 to –2) and the data are presented in Fig. 3.6 for 32-16 mm size range (essential lapilli) as well as the entire size range analyzed (labeled as global composition). The other size ranges (16-4 mm) are given in the appendix and are not discussed in detail here.

Several clast types were distinguished from each other; pumice (rhyodacitic pumice, with round to ovoid bubbles), tube-pumice, clots of crystal-rich juvenile material (with less then 5% bubbles), mafic scoria (lava blebs of basaltic andesitic to andesitic composition (Druitt et al. 1999)), lava lithics (clasts of aphyric, dacitic lava), hydrothermally altered lithics (reddish lithics of undistinguished type) and misc. lithics (lithics that are not part of the others).

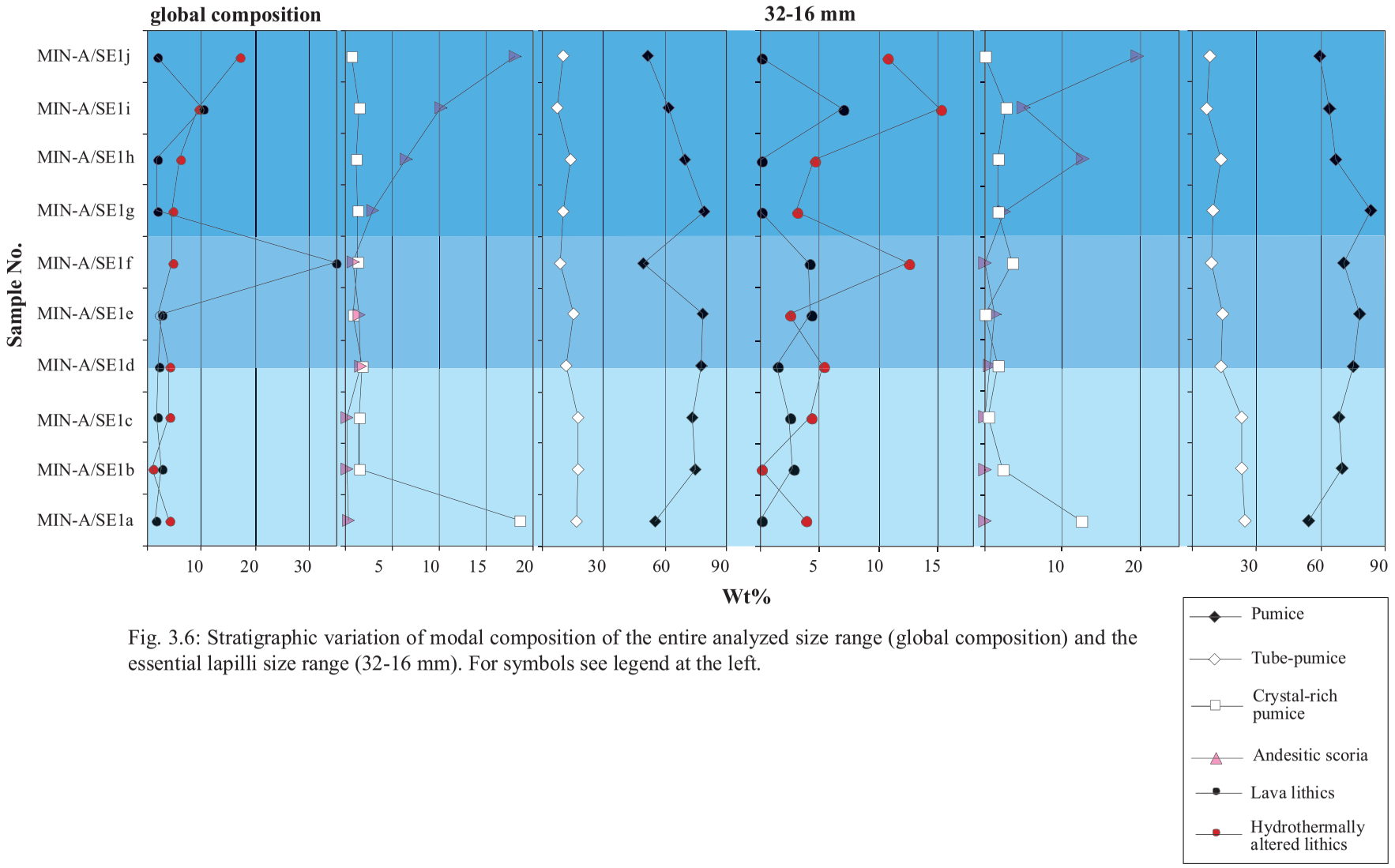

Fig. 3.6: Stratigraphic variation of modal composition of the entire analyzed size range (global composition) and the essential lapilli size range (32-16 mm). For symbols see legend at the left.

Pumice clasts dominate and comprise >50 wt% up to 87 wt%. The pumice content increases significantly from SE1a to SE1b (55 wt% to 75 wt%) and then remains quite stable at about 80 wt% for the samples SE1c on, to decrease steadily from 79 wt% in SE1g to 51 wt% towards the top of the profile. The minimum in SE1f composition results from a single lithic clast >32 mm.
Tube-pumice is only abundant in the lower three samples (SE1a to SE1c) and constitutes ~17 wt% of the composition. In the upper part of the deposit tube-pumice makes up only 7 to 15 wt%. This trend is more pronounced in the essential lapilli, with a decrease from 23-24 wt% to 7-14 wt% in the same samples.

The crystal-rich clots and mafic scoria behave exactly opposite to each other in global and essential size range. While the white altered clasts show a maximum of 18.5 wt% in the global composition and 12 wt% in the essential lapilli of the lowest sample SE1a and are very rare in the upper part (global: <2 wt%; essential lapilli: <3 wt%) the mafic scoria is rare or absent in the lower part of the deposit (≤2 wt%). It increases steadily from ~3 wt% in SE1g on to 18 wt% in global composition and 14 wt% in essential lapilli towards the top of the fall deposit.

The lithic component of the deposit commonly makes up <10 wt% of the deposit. The lava lithics show no clear trend and oscillate at low abundance between 1.3 and 2.6 wt% in global composition and between 0 and 7 wt% in essential lapilli. A few peaks with higher amounts (~10 wt% and ~35 wt%) in SE1f and SE1i, caused by single lava clasts in the size range >32 cm.
The altered lithics comprise between 1 and 4 wt%. But from the sample SE1f upward their abundance increases gradually from 4.6 wt% to 16.8 wt% at the top. In the essential lapilli range altered lithics are in part more abundant in the lower samples with 0 to 5.2 wt%. But their abundance also increases from SE1f on (4.5 to 12.5 wt%). The increase is not as linear. The misc. lithics make up always less than 3 wt% or are absent.

The major trends in modal composition also occur in the other size ranges and no size dependence was observed. The only exception is the size range >32 mm. But in this size range the amount of clasts is limited and is therefore not considered to be representative.

3.1.3. Density

The density was determined of ten pumice and tube-pumice clasts of each stratigraphic stage of the deposit (Fig 3.7). The pumice density is higher at the base of the section with about 680 kg/m³ (SE1a to SE1c, stages 1 to 3). The pumice density then decreases abruptly. Tube-pumice density decreases successively within the same samples from 705 to 383 kg/m³. The density minimum is at SE1d (stage 4) with 326 kg/m³ for pumice and 244 kg/m³ for tube-pumice. Density increases again to 413 kg/m³ for pumice and 412 kg/m³ for tube-pumice. From sample SE1f on density stays stable at values around 288 to 315 kg/m³ for pumice and 296 to 320 kg/m³ for tube-pumice. Only the last sample deviates form this trend with a density increase to 387 kg/m³ for pumice and a decrease to 265 kg/m³ for tube-pumice.

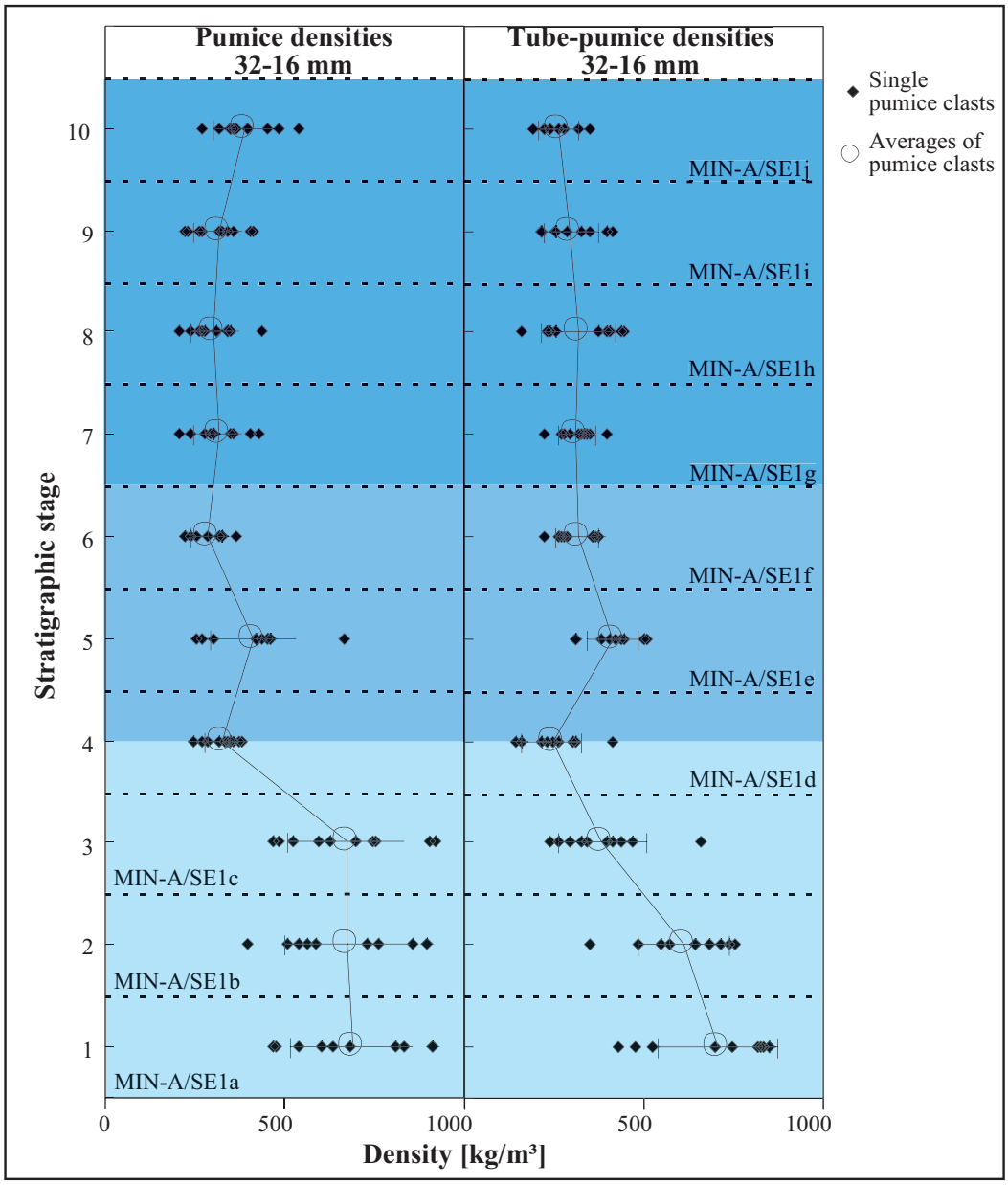

Fig. 3.7: Stratigraphic variation of pumice and tube-pumice clasts density.

The density is a measure for the vesicularity of the sample if the density of the melt is known. Taking a density of 2500 kg/m³ for the unvesiculated magma (Wilson and Houghton, 1990) the vesciularity of the pumice and tube pumice varies between 71.8 % and 89.4 % for the entire section. This vesicularity variation lies in the range common for pumice of explosive eruptions (e.g. Gardner et al., 1996; Melnik, 1999)

3.1.4. Permeability

Permeability was determined for one to four samples per stage, depending on the availability of clasts large enough for sample preparation (Fig. 3.8). The permeability decreases from $8.9x10^{-12}$ to $1.9x10^{-12}$ m^2 over three first stages (SE1a to SE1c). Above this decrease the permeability oscillates between $6.2x10^{-12}$ and $1.9x10^{-12}$ m^2 over stages four to nine. At the last stage the permeability jumps to $1.3x10^{-12}$ m^2. The extraordinarily high permeability ($3.1x10^{-11}$ m^2) observed at stage six (representing SE1f) is caused by a highly vesiculated tube-pumice with a permeability of $1.1x10^{-10}$ m^2. Rejecting this clast a permeability of $4.9x10^{-12}$ m^2 is found for stage six, placing it in the range described for this stratigraphic range.

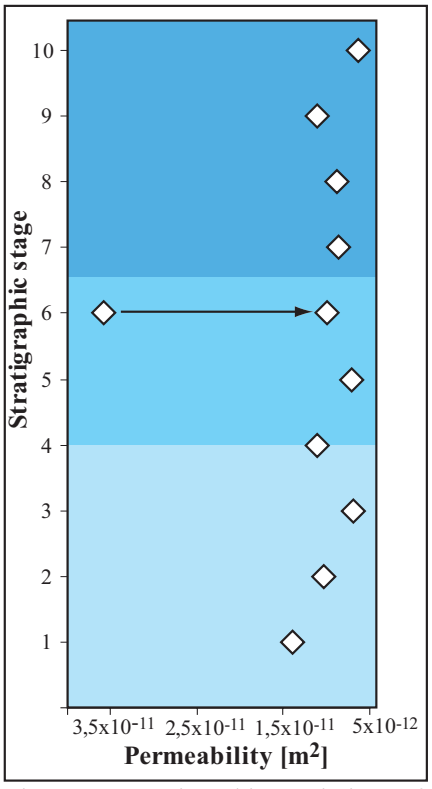

Fig. 3.8: Stratigraphic variation of average permeability for each stage. The arrow at stage 6 marks the shift of the average permeability, rejecting the highly permeable tube-pumice (see text).

3.1.5. Shape parameters of clasts

The three shape parameters formfactor, solidity and elongation were determined for at least 70 clasts in the 1-2 mm grain size range for each stage. This grain size was selected because the clasts are commonly not fragmented at deposition, contrasting with the larger, angular clasts. For each shape parameter both the average values and standard deviations and the binned frequency distribution over the range of values are shown in Figs. 3.9 and 3.10.

Formfactor

The formfactor is the ratio of the clast area to the area of an equivalent circle and thus is a measure for the grade of circularity of the clast. A perfectly circular shape is represented by a

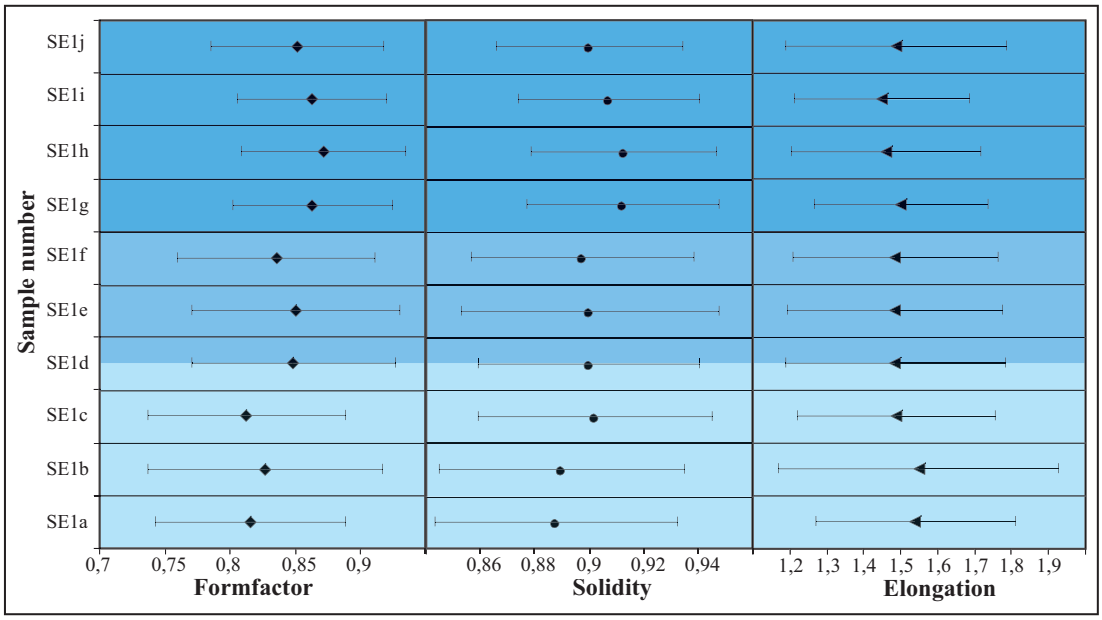

Fig. 3.9: Stratigraphic variation of the pumice clast shape parameters formfactor, solidity and elongation. The standard deviation 2σ is displayed as error bars.

formfactor of 1. The mean values of formfactor are <0.9 over the entire stratigraphy. In the lowermost three samples (SE1a to SE1c) the mean value of formfactor is between 0.81 and 0.82 and jumps to mean values between 0.83 and 0.85 for the following three samples (SE1d to SE1f). The last four samples (SE1g to SE1j) display the highest mean values of formfactor between 0.85 and 0.87. The peak mean value of 0.87 is reached in sample SE1h and steadily decreases from this sample towards the top of the profile. The uppermost four samples display a smaller standard deviation (0.056 to 0.066) compared to the samples below (0.072 to 0.089). This is also observed in the frequency distributions (Fig. 3.10) which display an upward decrease in the abundance of clasts with a formfactor <0.85, while the count peak oscillates between 0.85 and 0.90.

Solidity

The solidity is the ratio of the clast area to the area of convex envelope (the area confined by a rubber-band wrapped around the clast) and is a measure for the particle smoothness. This measure of smoothness is equivalent to the angularity or roundness of clasts as commonly used in sedimentology to describe clast shapes (e.g. Russell and Taylor, 1937). The solidity of 1 represents a perfectly smooth and well-rounded clast. The mean values of solidity increases from 0.89 for the lowermost two samples (SE1a and SE1b) to 0.90 for the four subsequent samples. The highest values of solidity between 0.90 and 0.91 occur in the uppermost four samples with the peak value in sample SE1h. From this peak value of 0.9129 the solidity decrases again to 0.90 towards the top of the section. The standard deviation decreases from values between 0.040 and 0.047 at the lowermost part of the section to values from 0.033 to 0.035 in the uppermost four samples. This narrower range of values of solidity

is also displayed in the frequency distributions (Fig. 3.10), where the abundance of clasts with a solidity <0.90 decreases upwards. The peak is at a value of 0.90 in all samples.

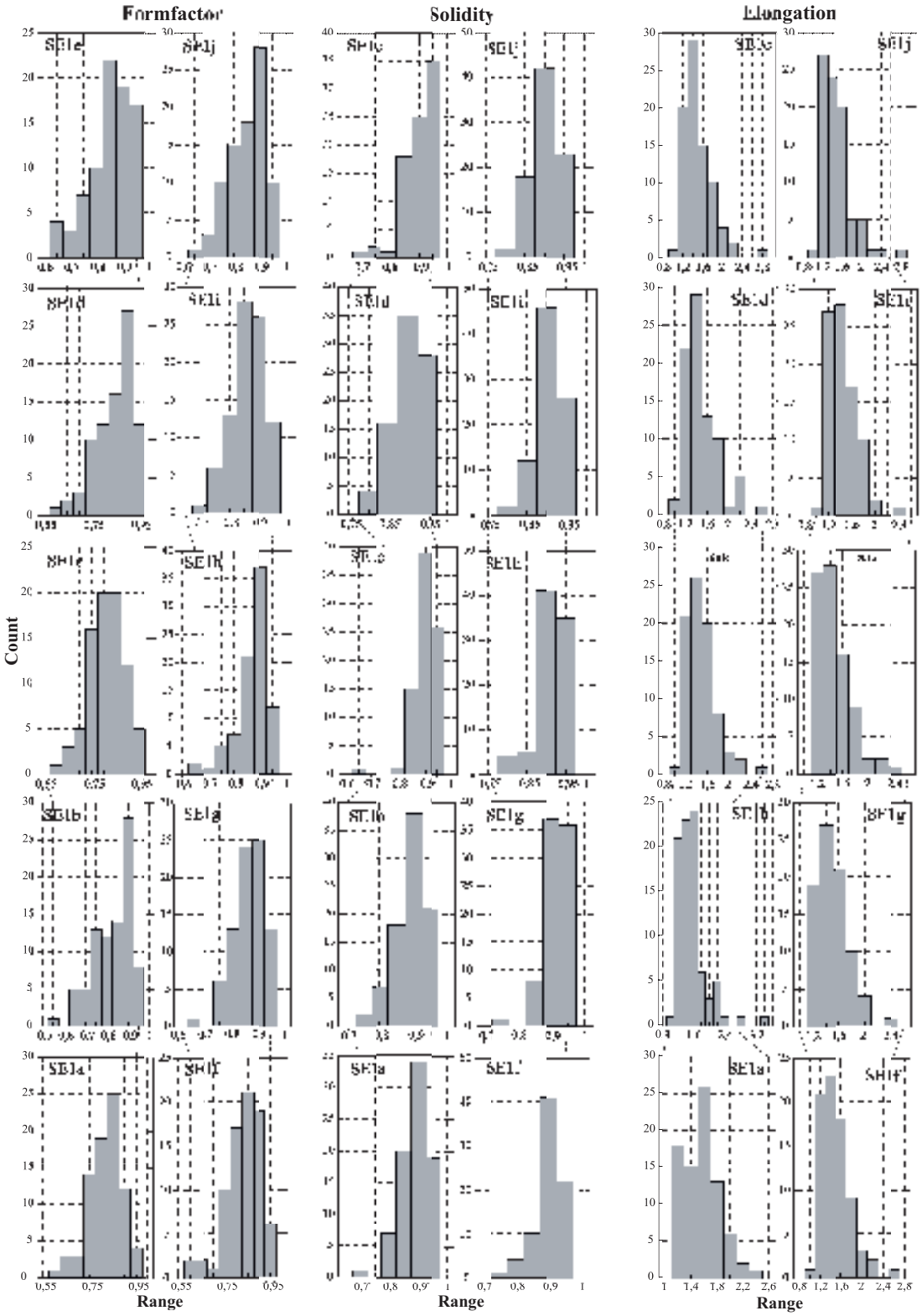

Fig. 3.10: Binned frequency distribution of pumice clast shape parameters formfactor, solidity and elongation.

Elongation

Elongation is the ratio of long to short axis of the analyzed clasts and is a measure for the deviation of the clast shape from a perfect circle, represented by an elongation value of 1. All elongation mean values are >1. The highest values of elongation (1.54 to 1.55) occur at the base of the section within samples SE1a and SE1b. Above these stages the values remain ≤1.5 and reach their minimum in sample SE1i with the value of 1.45. The standard deviation is quite stable over the entire profile with values between 0.23 and 0.30 and only the sample SE1b has a higher value of 0.37. The frequency distributions (Fig. 3.10) display a peak moving from values around 1.6 at the base towards values between 1.2 and 1.4 in the upper samples. Also an upward decrease in abundance of the number of clasts with an elongation value >2 is observed.

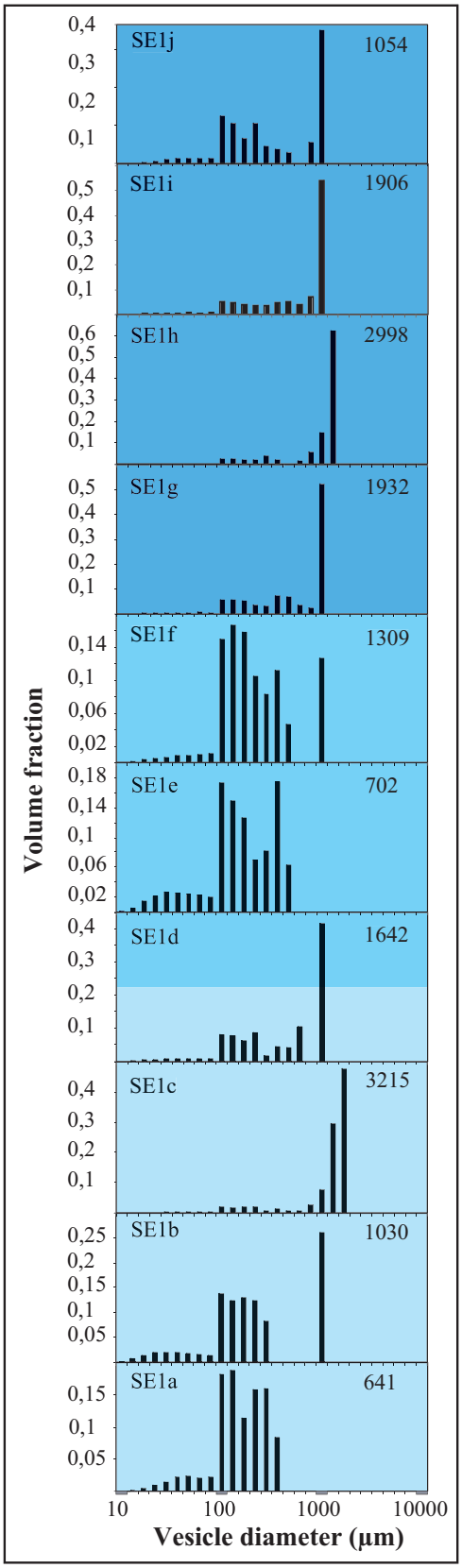

Fig. 3.11: Stratigraphic variation of vesicle volume distribution. The value at the right is the maximum vesicle size of the sample.

3.1.6. Vesicle size distribution

Vesicle volume distribution

The vesicle size distributions (VSD) are presented as volume distributions (Fig. 3.10) and are both uni- and typically polymodal. The volume distributions of the Minoan Eruption shows polymodal distributions at the base (SE1a and b), center (SE1e and f) and top (SE1j) of the section. These polymodal distributions show major peaks at equivalent diameters (representing the diameter of a circle with an area equivalent to the area determined for the vesicle) of 100-600 µm and minor at 1000 µm. Only in SE1b and j the major peaks occur at 1000 µm. All other samples (SE1c, d and g to i) are unimodal and show a major peak at larger diameters (1000 to

3000 µm). Another feature of the VSD, deduced from the volume distribution is the maximum vesicle equivalent diameter which shows a significant variation (see Fig. 3.11). It increases from a maximum eq. diameter of 641 µm at SE1a to 3215 µm at SE1c. Above this peak the maximum eq. diameter decreases again to 702 µ in SE1e and increases again to 2998 µm in SE1h. Towards the top of the section the eq. maximum diameter decreases again to 1054 µm.

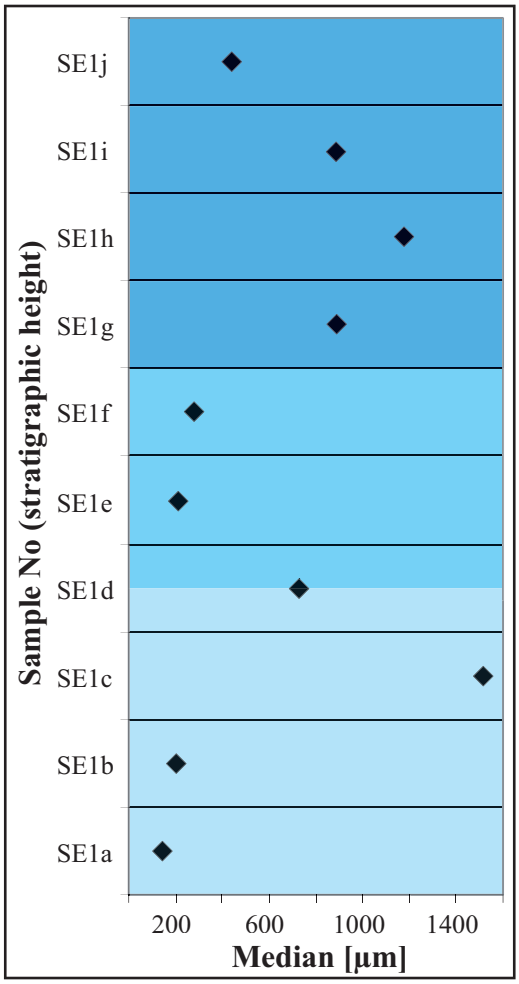

Fig. 3.12: Stratigraphic variation of the volume-based median vesicle size.

Volume-based median diameter

The variation of the VSD can also be described by the volume-based median vesicle diameter (Fig. 3.12), deduced from the cumulative volume distribution by determination of the diameter at a volume fraction of 0.5. The determined median diameter increases significantly from 145 to 1514 µm from SE1 a to c and decreases subsequently to 214 and 282 at stages SE1e and f. Then the median diameter increases to 1175 µm at SE1h and decreases towards the top to 437 µm.

Cumulative number densities

The cumulative vesicle number densities (Fig. 3.13) are a proxy for the bubble nucleation through time. Here the number density of vesicles larger than a given size (N_v>L) is presented as a function of logarithmic vesicle size L. The number density of the samples is the intercept of each curve with log L=1 (with L being the vesicle diameter and 10 µm representing the small size limit of the applied imaging technique). The resulting number densities lack the numbers of vesicles of the size between 1 and 9 µm and may, therefore, be slightly underestimated, but contain information about the relative variation of number density and give a rough estimate on the nucleation through time.

The number density comprises a small range from 1.8 to 9.6×10^5 cm^{-3}, with the lowermost two samples covering the entire range. The number density increases from SE1a to SE1b. In SE1c the number density decreases to 2.2×10^5 cm^{-3} and increases to 6.3 and 6.6×10^5 cm^{-3} in

SE1d and e. Then number density decreases to $4.7x10^5$ cm^{-3} in SE1f, increases to $6.3x10^5$ cm^{-3} in SE1g and decreases again to $4.5x10^5$ cm^{-3} in SE1h. Number density jumps up to $8.3x10^5$ cm^{-3} in SE1i and down to $2.1x10^5$ cm^{-3} in SE1j.

The log L vs. log N_v>L plot shows that the vesicle population in the Minoan pumice clasts define a power law trend. This power law size distributions are observed in both experimentally generated foams (Blower et al., 2002) and magmatic systems (e.g. Gaonac'h et al., 1996; Blower et al., 2001). Power law distributions (here described by the logarithmic relation $N_V>L \propto L^{-D}$) are characterized by their fractal dimension D (also called power law exponent). The power law is commonly only valid for a restricted range of vesicle sizes and does not fit for smallest and largest vesicles in the population.

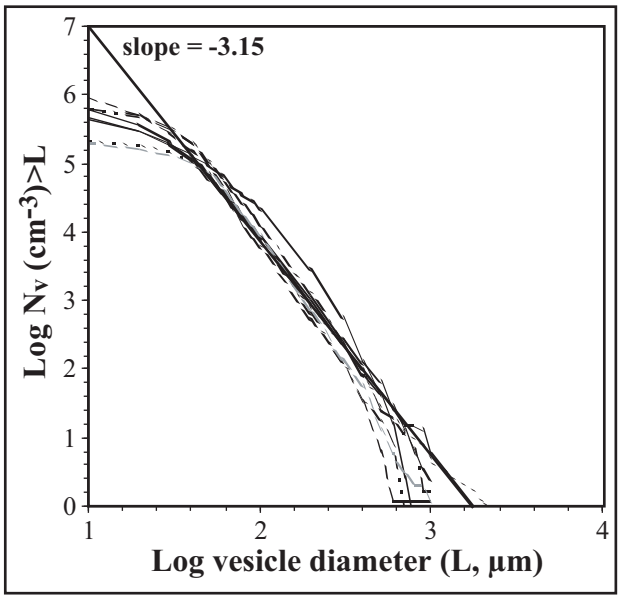

Fig. 3.13: Cumulative number densities (N_V>L) of all samples (dotted lines). The thick line represents the average of all samples and has a slope of -3.15 and is the best fit to the large size vesicles of all samples.

Vesicles of all Minoan pumice clasts define a single power law trend with an average slope of –3.15 (range from –2.7 to –3.5), representing an average fractal dimension D=3.15. The values of D of the clasts show an increase from 3 to 3.5 at stages SE1a and b, then decrease to 2.7 in SE1c and subsequently increase to 3.4 at SE1f. The value of D decreases to 2.8 in Se1h and increases to 3.1 towards the top of the section. All samples deviate from the power law trend at small vesicle sizes (<80 µm) where they define exponential trends (Blower et al., 2001).

3.1.7. Chemistry/Viscosity

Rhyodacitic pumice

The chemical bulk rock variation of pumice is very small with a slight, continous increase of e.g. SiO_2-content from 70.1 to 71.7 wt% (Fig. 3.14) in agreement with other published data (e.g. Driutt el al., 1999). The other major elements also show that a slightly more evolved magma erupted at the end of the Plinian phase (Appendix A-1-9). The water content of the pumice clasts constantly increases over the section from 3.5 to 3.9 wt%. The water contents

are considered being representative for the matrix glass water content due to the low crystal content (lacking an OH-Phase) and the fresh unaltered material (lacking diagenetic water). The bulk rock water content is, also, comparable to that of matrix glass analyses (e.g. Michaud et al., 2000; own unpublished data). Therefore these data were used as approximation of the stratigraphic variation of the water content of the magma at the moment of quenching (fragmentation). The temperature of the magma was determined by Cotrell et al. (1999) to be 885±7°C (using magnetite-ilmenite pairs) and a pre-eruptive water content of 6 wt% is assumed (e.g. Druitt el al. 1999). This results in a viscosity range of the rhyodacitic melt from $6x10^3$ to $8x10^3$ Pa s (calculated after Shaw, 1972).

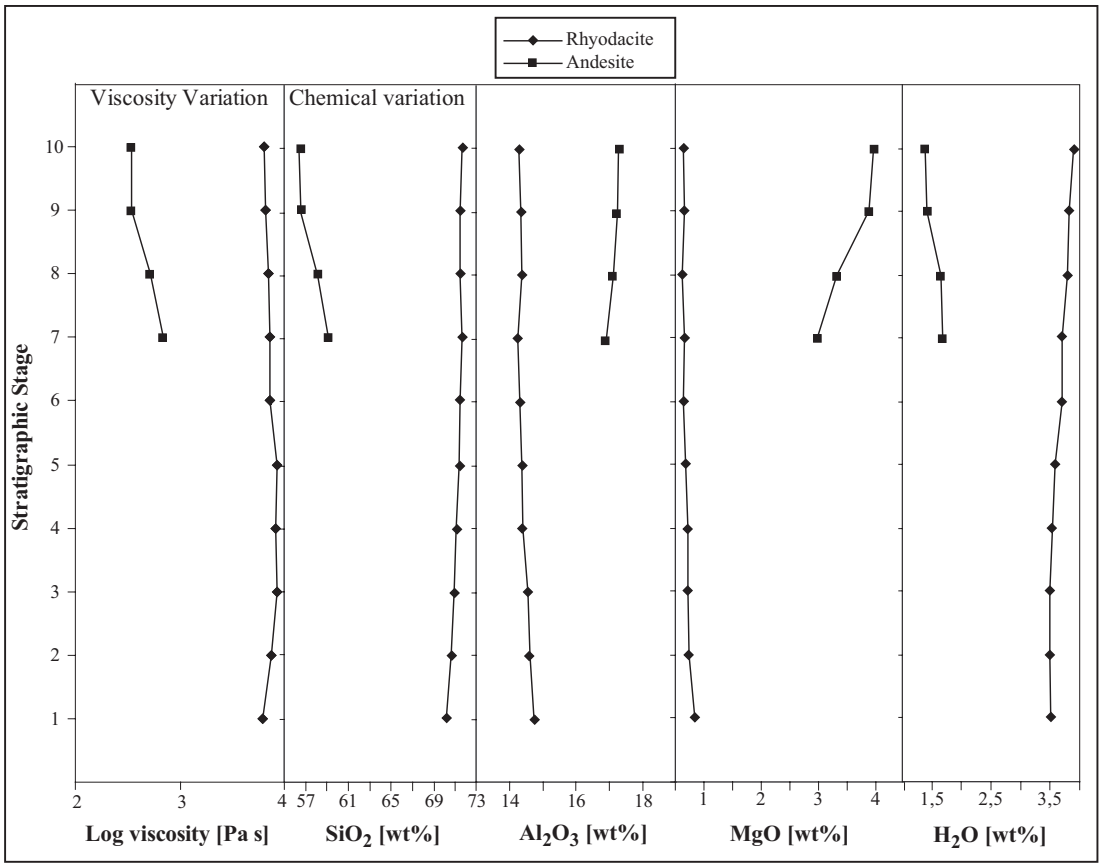

Fig. 3.14: Stratigraphic variation of calculated melt viscosity and selcted element oxide components (SiO_2, Al_2O_3, MgO and H_2O), being representative for the compositional range of both rhyodacite and andesite magma erupted during Minoan eruption.

Andesitic scoria

The andesitic scoria range widely in composition with SiO_2-content ranging from 56.4 to 59.2 wt% (Fig. 3.14) and become more mafic upward in the section (Appendix A-1-9). The water content decreases from 1.7 wt% to 1.4 wt%. The magma temperature of the andesitic component was determined to be 995±10°C by determination of the trapping temperatures of melt inclusions in olivine phenocrysts of andesitic scoria (Michaud et al., 2000). Electron microprobe analyses of the same melt inclusions (Michaud et al., 2000) allow an estimate of the pre-eruptive water content being 5.15±0.89 wt% (using difference method of Devine et

al., 1995). The resulting melt viscosity ranges from $3x10^2$ to $7x10^2$ Pa s (calculated after Shaw, 1972).

3.2. Discussion

3.2.1. Intensive parameters of the eruption

Eruption column height evolution

The eruption column height can be derived from the maximum pumice clast size (MCS) of the deposit (Carey and Sparks, 1986). A quantitative determination of column height variation can only be estimated because the three profiles are not sufficient to get MCS isopleth maps that are needed for column height calculation.

The MCS data indicate an increase in eruption column height at the beginning of the Plinian eruption. The MCS data of profile 1 and 3 have a minor peak in the lower third of the deposit (stages 3 and 4), indicating a first peak height of the column. Thereafter the column height decreased briefly. The data above this minimum display increasing MCS up to stages 7 to 9, indicating a second phase of rising column height. The major peak height was reached during the last third of the eruption. Thereafter the column height decreased successively till the phreatomagmatic break. The peak eruption column height was estimated by Sigurdsson et al., 1990 as 36 km for the entire Plinian phase, based on the MCS method of Carey and Sparks (1986). If this column height is represented by the peak MCS, a rough estimate of the column height variation is possible by calculating the relative mean MCS variation (averaged ratio of peak MCS to the MCS of each stage and profile). Further assuming that the MCS isopleth shape remains constant (and therefore the isopleth areas) at one locality while the MCS value changes at this locality, the variation of the relative MCS reflects the changes of eruption column height. These relative MCS suggest that the eruption column rose from ~17 to ~27 km during the first third of the eruption, then declined to ~24 km for a short period and rose again to the peak 36 km shortly before the end of the Plinian phase (Fig. 3.15a).

Mass eruption rate and erupted mass

The peak mass eruption rate ($2.5x10^8$ kg s^{-1}) and the total erupted mass ($4x10^{12}$ kg) of the Plinian phase (Sigurdsson et al., 1990) allow to calculate the duration of the eruption by dividing the total erupted mass and the mass eruption rate. This results in a minimum eruption duration of 16,000 s (267 min or 4.4 h). This estimate is definitely a minimum, because the mass eruption rate used for calculation represents a peak value and it is well

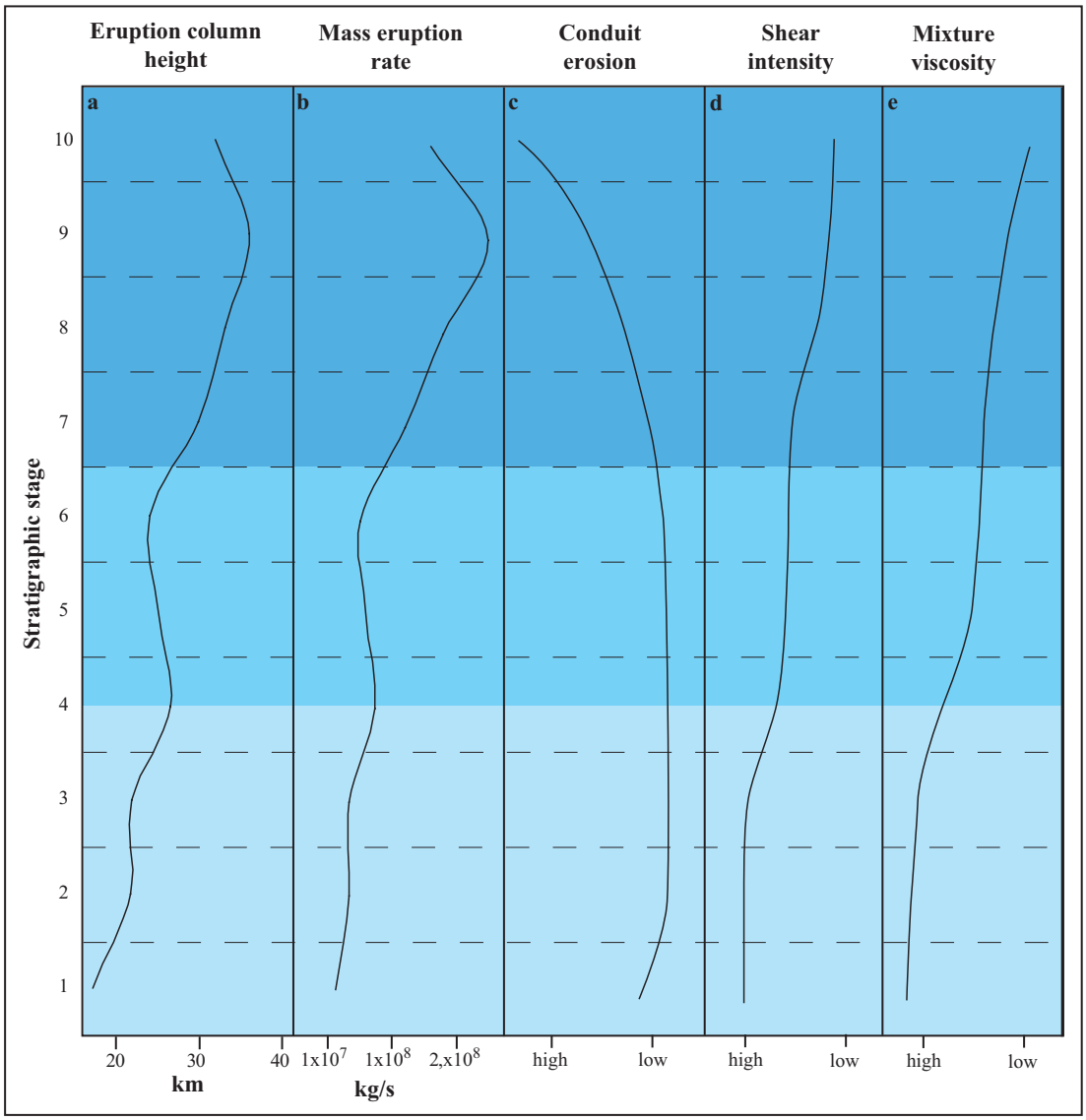

Fig. 3.15: Temporal variation of intensive parameters (a: eruption column height; b: mass eruption rate) and conduit flow parameters (c: erosion; d: shear inensity; e: melt-gas mixture viscosity). The stratigraphic stages are given as equivalent of the temporal development of the eruption.

known that an increase in mass eruption rate is common during Plinian eruptions (Sparks et al., 1997). Such increases were formerly attributed to conduit erosion (Wilson et al., 1980) but are now interpreted to be controlled by an increase of the depth of the fragmentation level and a resulting decrease of conduit wall friction and shear intensity (Sparks et al. 1997).

The relationship between eruption column height and mass eruption rate (Wilson and Walker, 1987) is used to calculate the mass eruption rates corresponding to the estimated column heights. The application of Wilson and Walker's (1987) formula resulted in a peak mass eruption rate (5.4×10^8 kg s^{-1}) that is more than twice that of the peak value (2.5×10^8 kg s^{-1}) determined by Sigurdsson et al. (1990) on basis of the maximum lithic isopleth data (Bond and Sparks, 1976; Carey and Sigurdsson, 1989). The calculated results were thus normalized to the value determined by Sigurdsson et al. (1990) for comparison purposes.

The corrected data indicate an increase of mass eruption rate during the first third of the Plinian phase from $1.3x10^7$ to $7.4x10^7$ kg s^{-1} followed by a brief decrease to $5x10^7$ kg s^{-1} and subsequent increase to the peak value of $2.5x10^8$ kg s^{-1} shortly before the end of the phase (Fig. 3.15b). Taking the calculated variation of the mass eruption rate and assuming that each stage makes up a 10^{th} of the entire deposit, the duration of each stage can be calculated. The sum of all stages results in a duration of 1410 min (23.5 h) for the entire eruption well inside the typical duration of historical Plinian eruptions (2-36 h) reported for different eruptions including Pinatubo, Mt St Helens, El Chichón and Redoubt; Smithsonian Global Volcanism Program homepage (www.volcano.si.edu/gvp/).

3.2.2. Conduit erosion

The evolution of the conduit diameter during the eruption can be deduced from the abundance of lithoclasts reflecting erosion intensity in the conduit (assuming that erosion is occurs in the conduit, Fig. 3.15c)). The low abundance of lithics in the lower deposit indicates a low intensity of conduit wall erosion during the first half of the eruption. The crystal-rich clots, representing partial melts of older granitoids which formed the roof and walls of the magma chamber (Druitt et al., 1999), are most abundant at the beginning of the Plinian eruption indicating that after the opening of the vent the crystallized shell at the top of the magma chamber was eroded.

The increase in the abundance of hydrothermally altered lithics (up to ~20 wt%) and in lithic maximum clast size in the upper half of the deposit is interpreted as a significant increase of erosion of the conduit walls (see also Taddeucci and Wohletz, 2001). This enhanced erosion, accompanied by an increase in mass eruption rate, suggests a major conduit collapse. This collapse supplied enough material into the eruption that the dilution effect (Varekamp, 1992) caused by the increasing mass eruption rate was masked. The decrease in mass eruption rate and eruption column height at the end of the eruption was accompanied by the highest amount of hydrothermally altered lithics. This could be a result of both ongoing conduit collapse and decreasing dilution effect, due to a decrease in the abundance of juvenile material. Further a possible collapse of the magma chamber roof can be taken into account. This may mark the onset of roof collapse that is assumed to have taken place during the MIN-B phreatomagmatic phase and cumulated during the ash flow generating phases (MIN-C and D; Druitt et al., 1999). However, the conduit and possibly magma chamber roof collapse event shattered the entire edifice substantially and led to a large scale access of water into the conduit that is marked by the phreatomagmatic break at the top of the Plinian deposit.

3.2.3. Rheology and conduit flow

Information about the variation of the magma rheology and conduit flow can be gained from the mass eruption rate, pumice textures and chemistry and the changes in the juvenile clast population and clast shape parameters in the deposit. Information about the degassing of the rising magma can be deduced from the pumice textures (vesicularity, permeability and VSD). Combination of the textural data with the chemical variation allow to estimate the viscosity changes. The viscosity of the mixture of the two magma batches involved in the eruption (rhyodacite and andesite) and shear intensity changes in the conduit can be deduced from the modal variation of the juvenile clasts and the shape parameter changes.

Shear intensity in the conduit

Tube-pumice is much more abundant during the first third of the Plinian phase, decreasing in abundance at the top of the lower third of the deposit. Also, the shape parameters show contemporaneous jumps comprising increasing values of formfactor and solidity and decreasing elongation. All these changes suggest a shear intensity decrease in the conduit at the end of the first third of the eruption (Fig. 3.15d). In the upper third, further slight jumps to higher values of formfactor and solidity occur, while elongation and tube-pumice abundance show no significant change. In addition, the standard deviation of formfactor and solidity decrease, indicating a narrower range of values. The latter changes in formfactor and solidity may be caused by a further shear intensity decrease caused by enhanced conduit erosion and widening observed during the last third of the eruption.

Degassing, vesicle nucleation, growth and coalescence

A vesicularity increase in the four lowermost stages (Fig. 3.7) indicates that the degree of degassing of the magma increased over the first third of the eruption and then reached a stable degassing regime in the conduit. An increasing vesicularity is commonly related to an increase in permeability (Klug and Chashman, 1996), but the data (Fig. 3.8) display a decrease in permeability over this range. However, the higher permeability in the lower part of the section indicates an enhanced gas flow through, and gas escape out of, the magma and therefore degassing at the beginning of the eruption. It can be assumed, that he high abundance of tube-pumice (as result of the high shear intensity) during this phase of the eruption had a positive effect on the gas escape. The decrease in permeability possibly explains the higher vesicularity that developed contemporaneously, because the gas flow out of the magma became more restricted. This restriction led to a higher expansion of the

magma that is expressed in a higher void volume in the pumice clasts erupted. This upward increase in void space is also expressed in the upward increasing maximum and median eq. diameters observed in the pumice of the first third of the deposit (Figs. 3.11 and 3.12). The vesicularity decrease from stages 4 to 5, observed in the density data also has its expression in the decrease of maximum and median eq. diameter, showing a minimum at stage 5. The increasing and subsequently decreasing maximum and median eq. diameters observed in stages 6 to 10 is not reflected in the vesicularity variation.

These data indicate that vesicle nucleation and growth processes are responsible for the VSD changes during the second half of the Plinian eruption. A factor controlling the degree of vesiculation of the magma is the time available for the vesicles to nucleate, coalesce and grow by diffusion and expansion. Comparing the variation of VSD and mass eruption rate shows that the large median, maximum vesicle diameters and almost unimodal distributions occur in phases of high or increasing mass eruption rate, while small median, maximum vesicle diameters and polymodal distribution occur during phases of lower mass eruption rates. At first sight, this behavior appear counterintuitive, because high eruption rates suggest higher ascent velocities of the magma in the conduit and therefore less time for bubbles to grow and coalesce in the conduit. In order to increase the time span available for vesicles to grow and coalesce to develop VSDs with a significant void volume of large size vesicles the length of the path the ascending magma has to pass before it gets quenched varied. Quenching of the magma takes place at the fragmentation level for the clast size range analyzed (e.g. Mader, 1998). Therefore it can be assumed that the fragmentation level oscillated during the Plinian eruption, with a fragmentation level that was deep in the conduit at the beginning of the eruption. During the first third of the eruption, the fragmentation level moved upwards in the conduit while mass eruption rate increased, briefly moved downwards during a phase of decreasing mass eruption rate followed by a second phase of upward movement and downward movement towards the end of the Plinian eruption.

VSDs are not only a proxy for the degree of degassing of the rising magma but are also the integrated result of vesicle nucleation, growth and coalescence (Klug et al., 2002). The vesicle volume distributions provide information on the number of nucleation events and coalescence (Brazier and Sparks, 1982). The extent to which coalescence and single vesicle growth are responsible for the vesicle populations can be assessed from the size distributions (Fig. 3.11). The major and subordinate peaks at the 100 to 1000 μm size range in many samples (SE1a, b, d, e, f, g, i and j) indicate that bubble nucleation took place early in the vesiculation history and vesicle growth and nucleation occurred over a long time span. The samples with major peaks at >1000 μm (SE1c and h) underwent a longer time of vesicle

growth and coalescence than the samples with peaks at 100 to 1000 μm. Large vesicles (≥1000 μm) have been commonly interpreted to represent a population inherited from the magma storage area (Whitham and Sparks, 1986). Inherited vesicles are assumed to show a higher degree of deformation, as a result of the complex deformation history during their ascent (Klug et al., 2002). This is not plausible for the Minoan eruption, however, because the large vesicles do not show a significantly higher state of deformation than the small vesicles. They rather show a smaller range of elongation values compared to the small bubbles. Therefore a longer time range for the development of the vesicle populations was necessary for the samples containing large volumes of vesicles with large diameters, as already assumed.

The number densities of the pumice samples (1.8 to 9.6×10^5 cm^{-3}) are small compared to number densities determined in both heterogeneous and homogeneous nucleation experiments (~10^8 cm^{-3}, Hurwitz and Navon, 1994; Lyakhovsky et al., 1996; Gardner et al., 1999; Mangan and Sisson, 2000). These low values primarily result from the missing data of vesicles <10 μm (because of technical problems with the imaging system) that comprise a large amount of vesicles within the entire population. The time span necessary to generate the observed vesicle population can, therefore, not be determined. Times, calculated on the base of nucleation rates of 10^6-10^7 cm^{-3} s^{-1} (Klug et al., 2002), range between 0.01-0.1 s, which is implausible. Likewise, the degree of volatile supersaturation of the magma and the style of nucleation can only be estimated. Based on the determined number densities, supersaturation ranges from 120 to 130 MPa (Mangan and Sisson, 2000) and the absence of microlites as nucleation sites in all samples suggests rather homogeneous nucleation.

The cumulative number densities define power law trends (linear distributions on Fig. 3.13), a common feature in vesicle distributions generated during volcanic eruptions (e.g. Blower et al., 2002). The deviation of all samples from the power law trends at small vesicle sizes, where they define exponential trends (Blower et al., 2001), suggests that the vesicle distributions in all samples may comprise two populations: small vesicles (<60 μm) with exponential distribution and large vesicles that follow power law systematic.
The small vesicles (<60-100 μm) with their exponential trend and low abundance in volume distributions indicate that some minor late stage nucleation took place (Blower et al., 2002). Further the abundance of small size vesicles is smaller in samples that correspond to phases with low mass eruption rate (magma ascent velocity) and the proposed deeper fragmentation horizon. Therefore it is assumed that late stage nucleation, generating the vesicles, was less significant during the phases of slower magma ascent. A possible reason for this behavior may be that more effective vesicle growth led to a restriction of the space available for new

small vesicles to nucleate and lower decompression rates, leading to a less pronounced supersaturation of the magma also restricting nucleation (Gardner et al., 1999).

The large vesicle population (~60-1000 μm), defining a power law trend with fractal dimension D=3.15, is assumed to be produced by growth and coalescence of vesicles that nucleated in the conduit early in the vesiculation history. A continuous nucleation can be ruled out because of the high fractal dimension being significantly higher than the value determined for this so-called 'Apollonian' case (D=2.45; Blower et al., 2001). The critical value for coalescence-influenced power law distributions was determined in models, assuming a cascade of binary coalescence events, to be D>3 (Gaonac'h et al., 1996). So the variation of the fractal dimensions is relevant to deduce the importance of coalescence during the Plinian eruption. Fractal dimensions D<<3 occur only in SE1c, h and i. The first two samples (D=2.7 and 2.8) correspond to phases of increasing mass eruption rate, and are hence influenced by additional nucleation events, due to a supersaturation of the magma, caused by the higher ascent velocity and resulting higher decompression rates. The last sample (D=2.9) correspond to already decreasing ascent velocity, resulting in more time for the newly nucleated vesicles to grow and coalesce. The minimum D=2.7 is still larger than the Apollonian value of 2.45. It is, therefore, suggested that the large vesicles mainly formed by coalescence of small, early nucleated vesicles during the ascent of the magma in the conduit and only in the samples mentioned above a newly nucleated and grown population plays a minor role in the large vesicle population.

Viscosity

The viscosity of the ascending magma in the conduit is controlled by several factors such as composition of the magma (both magma chemistry and mixing ratio of the two magmas in the conduit), water content (degassing), vesicularity and crystal-content. Therefore information about the variation in viscosity and the effect on the conduit dynamics can be roughly gained from pumice chemistry and textures.

1. The chemical variation, including the changes of water content of the major rhyodacitic component of the Plinian phase, results in a viscosity increase from $6x10^3$ to $8x10^3$ Pa s during the first half of the eruption (after Shaw, 1972). The viscosity decreases to $6x10^3$ during the second half of the eruption, though the magma gets more evolved. This is an effect of the rising water content in the pumice, reflecting the water content at the point of fragmentation, exerting a larger effect on the viscosity than the variation of the major element composition (Hess and Dingwell, 1996). In the case of the rhyodacite erupted

during the Plinian phase, the water content variation results in approximately half an order of magnitude of viscosity decrease.

2. The degassing of the melt has a twofold effect on the magma viscosity. First the loss of water leads to a viscosity increase, because of the increased polymerization of the degassing melt (Sparks et al. 1994; Dunbar and Kyle, 1993). Second, it is assumed that an increase of the degree of vesiculation lowers the viscosity of the magma at low strain rate (Thomas et al. 1994). The effect of vesicles on the viscosity is still poorly understood, e.g. comparing vesicle-free magmas to vesiculated magmas both higher and lower viscosities are inferred (Manga et al. 1998). Recent studies show that vesicles cause a decrease of viscosity only over the low vesicularity range up to 50% (e.g. Bagdassarov and Dingwell, 1992; 1993; Manga and Loewenberg, 2001; Llewellin, 2002). Shearing has a significant effect on the viscosity of vesiculated magmas. Dingwell (1997; 1998b) emphasizes that at high strain rates vesicles lose their capability to deform and behave more like crystals and increase magma viscosity. Taking this into account, the high shear rates during the first third of the eruption resulted in a higher effective viscosity of the ascending magma than the melt viscosity. Combined with the higher viscosity in this phase of the eruption it can be concluded that the viscosity was several orders of magnitude higher than during the later phases of the eruption. The resulting effective viscosity of SE1a to SE1c increases from $9x10^7$ to $4x10^8$ Pa s (after Roscoe, 1952). The increase in vesicularity of the rhyodacitic pumice caused a decrease in the effective viscosity at the fragmentation level during the upper two thirds of the eruption.
3. The composition of the erupted mixture changed during the upper third of the eruption, concluded from the increasing abundance of andesitic scoria in the corresponding part of the deposit. This less viscous andesitic magma ($3x10^2$ to $7x10^2$ Pa s) exerted an increasing influence on the average viscosity (representing a horizontal slice through the conduit) of the erupted mixture, that decreased. Further the increasing abundance of the andesitic component caused an increase of mass eruption rate (see Chapter 3.2.1.) by lowering the viscous resistance in the conduit (Freundt and Tait, 1986). It, also, possibly enhanced the conduit wall or magma chamber roof collapse (see Chapter 3.2.2) as result of a drop of the pressure gradient along the conduit (Freundt and Tait, 1986). Another effect of the less evolved andesite is that of supplying the eruption with CO_2. Even small amounts of CO_2 cause an earlier gas exsolution and a significant drop of the magmatic pressure in the conduit, enhancing conduit wall/chamber roof collapse. This results in a downward migration of the fragmentation horizon and the pressure drop enhances conduit erosion and collapse as the CO_2 content increases (Papale and Polacci, 1998).

4. The crystal content of the magma was not taken into account for the viscosity variation, because the phenocryst content of the magma is assumed to be almost stable at 4% (Heiken, 1987). In the SEM images used for the VSD no microlites were visible. The effect of crystals on the magma viscosity can, therefore, be neglected.

In summary, the viscosity in the conduit underwent two phases of drastic viscosity decrease (Fig. 3.15e). These changes modified the general viscosity variation deduced from the chemical variation of the major magma component. One increase in viscosity is close to the end of the first third of the eruption, when the shear intensity in the conduit significantly dropped and vesiculation of the magma increased. The second took place during the last third of the eruption, caused by the increasing importance of the andesitic component in the conduit.

3.2.4. Fragmentation intensity

Fragmentation intensity can be deduced from the median and sorting coefficient. The major trend deduced is an increase in fragmentation intensity over the entire eruption (see also Taddeucci and Wohletz, 2001). But this increase is not gradual and two phases of increase in fragmentation intensity can be deduced from the median and sorting coefficient variation.
The first intensification was accompanied by a reduction of shear rate and viscosity in the conduit and an increase in vesicularity. Further the permeability of the magma decreased during this phase, detaining the gas in the vesiculating magma. This retarded gas flow out of the magma led to a higher degree of vesiculation and increased the vigor of the fragmentation. At this point of the eruption, the fragmentation style shifted from a more brittle, strain-dominated fragmentation (Papale, 1999) to a more ductile dominated fragmentation caused by wall thinning (Sparks, 1978).
The second intensification was accompanied by an increase in the supply of andesitic magma in the erupted mixture. The andesitic magma may have intensified fragmentation by supplying additional gas. This additional gas supply can be estimated by calculating the water loss of both components from the difference of bulk rock and pre-eruptive volatile-contents (Chap. 3.1.7.). This calculation results in a water loss of the magma decreasing from 2.3 to 2.1 wt% for the rhyodacite, while the water loss of the andesite increases from 3.49±0.89 wt% to 3.79±0.89 wt%. Absolute values can be gained by calculating the proportional masses of each component from the modal composition of the deposit and assuming each stage represents a tenth of the entire fallout mass ($4x10^{12}$ kg). The resulting masses of lost water from SE1g to SE1j decrease from $8.2x10^{9}$ to $5x10^{9}$ kg for rhyodacite

and increase from $4.2x10^8 \pm 1.1x10^8$ to $2.7x10^9 \pm 6.4x10^8$ kg for andesite. The density of water vapor can be derived from the ideal gas equation: d=PM/RT, where are T=800°C, P=10 MPa, M the molar mass of water, being 18 and R the universal gas constant. The calculated density of water vapor is 24.05 kg/m^3. The resulting stratigraphic variation of the volatile loss volumes are $3.4x10^8$ to $2.1x10^8$ m^3 for the rhyodacite and $1.7x10^7 \pm 4.6x10^6$ to $1.1x10^8 \pm 2.7x10^7$ m^3 for the andesite. These estimates show that the andesitic component supplied the eruption with an increasing amount of gas while the gas supply from the rhyodacite slightly decreased. Further the additional gas supply from the andesite is almost as high as that of the rhyodacite at the end of the eruption. This increased additional gas supply may have been responsible for the increase in fragmentation intensity during the last third of the Plinian phase. Fragmentation may also have been enhanced by external water. The enhanced erosion possibly shattered the edifice so much that pathways for seawater opened already well before the first phreatomagmatic explosions occurred.

3.3 Conclusions

The combination of all data shows significant variations in the overall lithology and pumice textures both at the top of the lower third and in the upper third of the deposit. Thus the Plinian phase of the Minoan Eruption can be subdivided into three phases, represented in three almost equal portions of the deposit (see color coding in Figs. 3.3 to 3.16). The only almost constant parameter is the chemical composition of the rhyodacitic pumice (Druitt et al., 1999, Fig. 3.14). The median and sorting coefficient, also, display three significant changes that take place at or close to the transitions between the distinct phases. The three phases and the major changes in the deposit and the suggested changes of the magma-conduit system are outlined below.

Phase 1: The opening-phase of the eruption (Fig. 3.16a) was characterized by an increasing eruption column height, mass eruption rate and ascent velocity of the magma, reaching a first peak in all three parameters and a slightly increasing fragmentation intensity at its end. The fragmentation horizon moved upwards during this phase. The decreasing abundance of tube-pumice and an abrupt change in the shape parameters at the end of this phase are taken as evidence for a decreasing strain rate as the eruption continued. The decreasing abundance of crystal-rich pumice in the deposit possibly reflects the initial cleaning of the plumbing system of more crystallized parts at the magma chamber roof. These possibly made up a coat, narrowing the magma chamber outlet into the conduit that opened at the beginning of the eruption. Whether or not the conduit was already open is not known, but the precursory

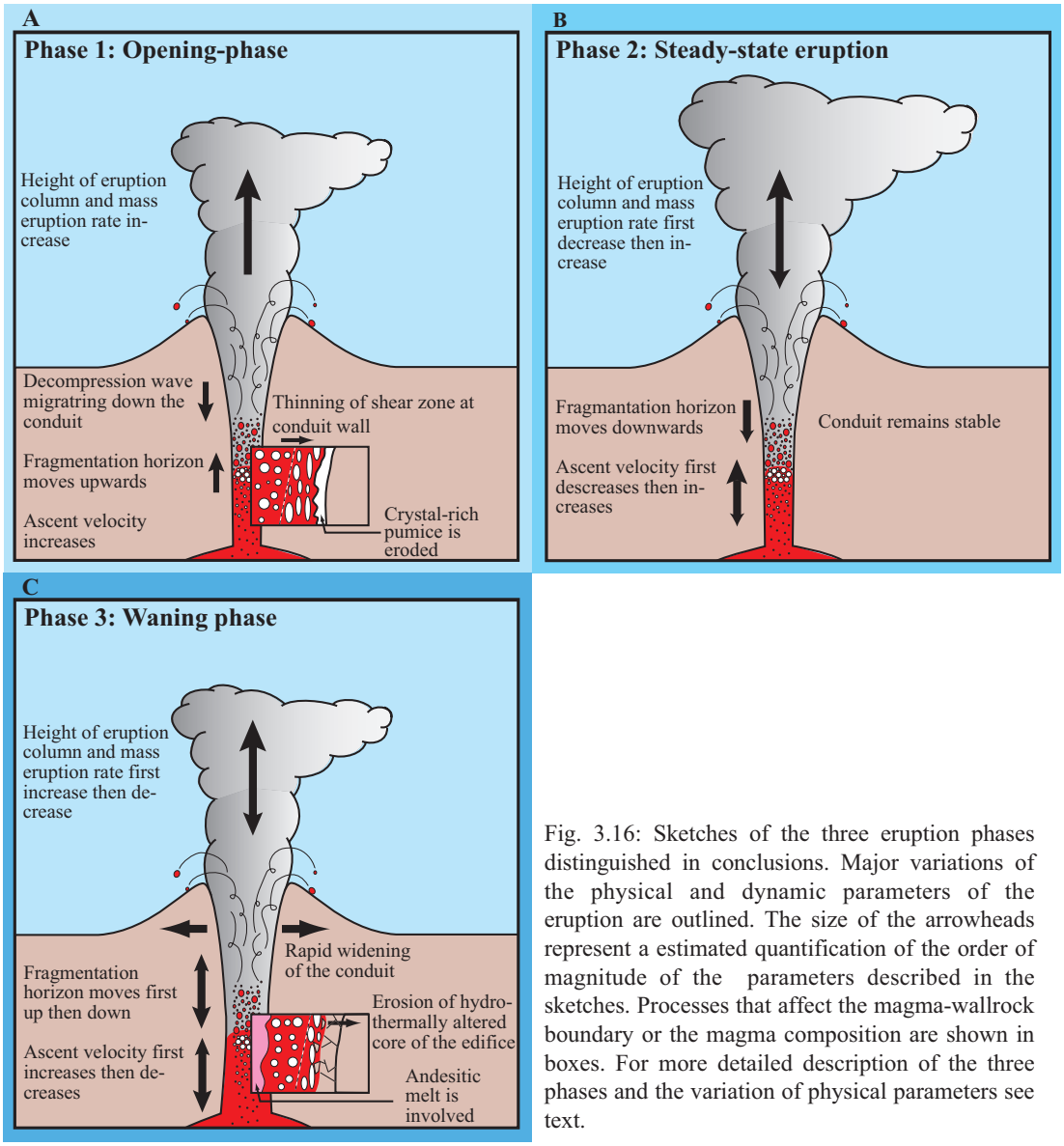

Fig. 3.16: Sketches of the three eruption phases distinguished in conclusions. Major variations of the physical and dynamic parameters of the eruption are outlined. The size of the arrowheads represent a estimated quantification of the order of magnitude of the parameters described in the sketches. Processes that affect the magma-wallrock boundary or the magma composition are shown in boxes. For more detailed description of the three phases and the variation of physical parameters see text.

activity (Heiken and McCoy, 1990) may point toward an already existing, magma filled conduit prior to the onset of the Plinian pase. Minor conduit wall erosion took place, as is reflected in the small amounts of both dacitic lava and hydrothermally altered lithics in the modal composition.

The significant changes in density and median/maximum vesicle-size in the lower third suggest an enhanced degassing at the beginning of this phase, possibly caused by a decompression wave migrating downward in the conduit after the opening of the system, possibly accompanied by a brief downward migration of the fragmentation level (Alidibirov, 1994; Alidibirov and Dingwell, 1996; Alidibirov and Panov 1998). This decompression wave may have increased the supersaturation of the magma and triggered a nucleation event at the very beginning of the Plinian eruption (stage 1), explaining the higher abundance of small size vesicles at the onset of the eruption while the mass eruption rate and ascent velocity were still low. The effect of the decompression wave diminished afterwards, but the

low fractal dimension (D=2.7 at stage 3) indicates a second nucleation event, caused by the increasing ascent velocity. In combination with the upwards moving fragmentation level and extended growth and coalescence time, larger vesicles were produced. The higher permeability of the pumice erupted during this phase supports an enhanced degassing capability of the magma, compared to the later phases. The enhanced degassing and lower vesicularity at the high strain rates during the opening phase additionally indicate a higher viscosity of the rising magma, next to the higher viscosity caused by the lower water content of the magma. In addition to the effects on viscosity, the degassing and hence the increasing gas volume in the magma increased the volume of the magma-gas mixture, resulting in an acceleration of the unfragmented magma, also contributing to the shear intensity.

Phase 2: During the second phase of the eruption (Fig. 3.16b) the eruption column first declined in height and then rose again. The mass eruption rate and ascent velocity behave in the same manner. The fragmentation horizon migrated downwards at the beginning of the phase and remained stable afterwards. The oscillation was preceded by an increase of the fragmentation intensity at the beginning of the phase. The fragmentation intensity remained almost stable during the entire phase. The conduit also appears to have been quite stable during this phase, except for ongoing minor conduit wall erosion. Further, the lower shear intensity in combination with higher vesicularity and water content in the magma caused a significant viscosity drop at the beginning of the second phase. The only significant variation was a decrease in median/maximum vesicle size and a density maximum in the middle of this phase. Thus it appears that the degassing of the magma became more restricted over a short period and the fragmentation horizon deep in the conduit shortened the time range for vesicle growth and coalescence. The less pronounced vesiculation during this short intermittent period, deduced from the density and median/maximum vesicle size, caused a decrease in the ascent velocity of the magma-gas mixture in the conduit, contributing to the oscillation of the eruption column and mass eruption rate. After this ocillation the degassing of the magma reached an almost steady state at the end of this phase that stayed stable until the end of the Plinian eruption. The vesicularity, maximum vesicle size and permeability increased and the magma-gas mixture in the conduit accelerated again, expressed in the rising eruption column height and mass eruption rate.

Phase 3: The waning phase of the eruption (Fig. 3.16c) first showed an increase in eruption column height, reaching a maximum and thereafter waning till the end of the Plinian phase. The mass eruption rate and ascent velocity show the same behavior, while the ascent velocity is assumed to had decreased more significantly than the mass eruption rate and column height, at least during the last half of this phase, when the elevated conduit erosion intensity

caused a widening of the conduit. The fragmentation level also first moved upward and then downwards again.

The upward movement of the fragmentation level explains the increase in median/maximum vesicle size, while the increasing ascent velocity explains the nucleation event deduced from the fractal dimension (D=2.8 at stage 8). The fragmentation intensity increased significantly during this last phase, even while the height of the eruption column declined. This elevated fragmentation intensity was possibly caused by additional gas supply into the conduit, either out of the andesitic magma component becoming more abundant during this phase or by external water gaining access to the conduit. The first gas source is more plausible because of the increase in andesitic scoria abundance and the resulting increase in gas supply. This was accompanied by an increase in hydrothermally altered lithic clasts as well as further slight jumps to higher values of formfactor and solidity. This is interpreted as a collapse event of the conduit walls or the magma chamber roof that involved the shattered, hydrothermally altered core of the edifice.

This erosion event led to a significant widening of the conduit, resulting in a reduction of the speed of the rising magma, lowered shear intensity and decreasing eruption column height. The deceleration of the magma in the conduit had no significant effect on the vesiculation and VSD, because other processes had a larger influence during this period. The average viscosity of the magma mixture in the conduit significantly decreased because of the less viscous andesitic component that made up a successively increasing proportion in the conduit, contributing to the lowered shear intensity by decreasing the viscous resistance (Freundt and Tait, 1986). Also the andesite may have contributed a higher amount of CO_2 than the rhyodacite to the gas mixture driving the eruption, decreasing the magmatic pressure in the conduit and lowering the fragmentation horizon. This decompression of the magma also enhanced conduit collapse by lowering the magmatic below lithostatic pressure (Papale and Polacci, 1998). A downward migrating fragmentation level may have caused the slight density increase observed in the last sample and contributed to the decreasing median/maximum vesicles size. At the end of the phase all this destruction of the edifice came to a head as seawater gained access to the conduit at the end of the Plinian phase.

4. Laacher See Eruption

The Laacher See eruption is the only known large explosive eruption that took place in central Europe during late Quaternary time and is the topic of many studies (e.g. Schmincke, 1970; 1977; 1981; 2000; Schmincke et al., 1973; 1990; 1999 Wörner and Schmincke, 1984; Bogaard and Schmincke, 1984; 1985, Freundt and Schmincke, 1985; 1986; Wörner et al., 1983, 1985; Tait, 1988; Tait et al., 1989; Bogaard et al., 1990; Harms and Schmincke, 2000, Harms et al., 2003). The Laacher See volcanic center (LSV) is located in the East Eifel volcanic field (EEVF), consisting of about 100 eruptive centers that cover an area of approximately 330 km². The EEFV is located west of Rhine River in the still uplifting Paleozoic Rhenish Massif. The LSV is situated centrally in the EEVF just north of the Neuwied tectonic basin northern boundary (Fig. 4.1). The Rhenish massif constitutes of folded Devonian slates, sandstones, graywackes and Tertiary sediments and represents the basement of the LSV.

The LSV is morphologically characterized by a basin filled by a lake (Laacher See), with 3,3 km² area, surrounded by a steep ringwall rising 90 to 240 m above the basin. The ringwall is made up by basanitic/tephritic cinder cones and the tuff-ring of the Laacher See eruption and resembles slightly an eight, suggesting that the ringwall constitutes of two adjacent, overlapping oval conduits. The internal structure of the Laacher See basin is dominated by the northeast-southwest striking "Siegen thrust" which separates two facies of Lower Devonian rocks from each other: 1) the sandy to silty "Siegen facies" making up the northwestern block and 2) the slates of the "Hunsrückschiefer facies" of the southeastern one.

The Laacher See eruption that took place ~12,900-12,880 yrs BP (e.g. Boogard, 1995; Hajdas et al., 1995) is a classic example for a complex Plinian eruption, with multiply changing eruption dynamics in the course of the eruption. The pyroclastic sequence (Laacher See Tephra – LST) has been subdivided into three major units:

- The Lower Laacher See Tephra (LLST), mainly Plinian fallout, except for the basal, proximal phreatomagmatic facies.
- The Middle Laacher See Tephra (MLST A-C), ash and lapilli beds at the base (MLST A) and interbedded Plinian fall and flow in the upper part (MLST B and C).
- The Upper Laacher See Tephra (ULST), mainly surge breccias, duned beds and ash flow deposits.

The three units differ from each other in lithology, eruptive and depositional differences, chemical and mineralogical composition and areal distribution. The chemical variation of the

LST reflects the successive evacuation of a chemically zoned magma chamber, varying from crystal-poor, highly differentiated phonolite at the base to crystal-rich mafic phonolite at the top of the LST sequence. The strongly varying eruption dynamics, reflected by the lithologic and depositional differences in the LST, are the expression of a superimposition of environmental factors (crustal lithology around the LSV, aquifer location around the vent, water supply rates into the vent), dynamic environmental factors, changing in the course of eruption (repeated lateral and downward vent erosion, construction, lateral vent migration, crater collapses and blockage of the vent) and internal factors (magma composition and properties, especially gas content and viscosity).

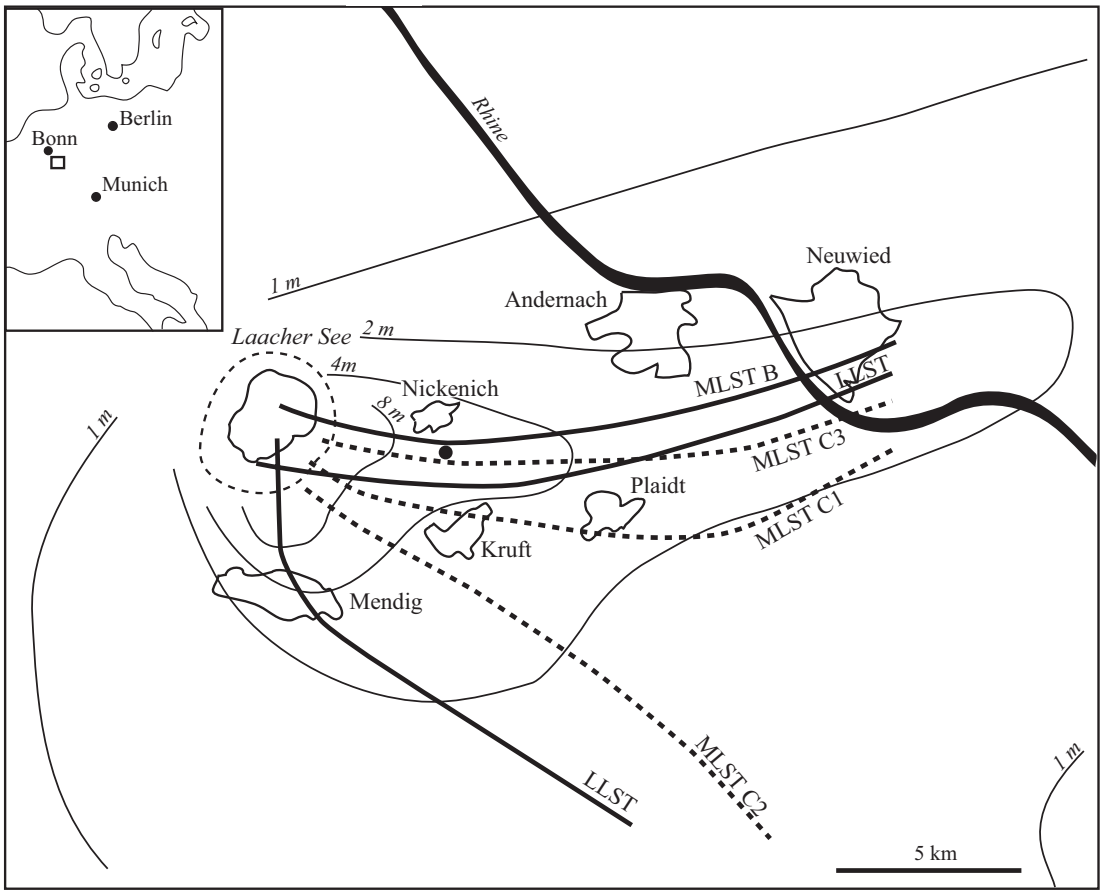

Fig. 4.1: Overview sketch of the Laacher See area including its position in Central Europe (see insect). The dashed line around the Laacher See marks the crest of the Ringwall. The main distribution axes (thick lines) and isopleth of the LST fan (thin lines with thickness labeled) are displayed (after Bogaard and Schmincke, 1984). The black dot south of Nickenich marks the locality of the pit, where the section and samples were taken.

The eruption started in the southern part of the Laacher See depression with an initial phreatic/hydroclastic stage, which was caused by a shallow level interaction of the rising magma or an associated gas phase with an aquifer. After the initial opening phase the vent was cleaned by the repeated strong explosions and the first open vent Plinian eruption column developed. The prevailing westerly winds distributed the tephra towards the east. In proximal areas southwest of the Laacher See (e.g. at Wingertsberg outcrop, so called Mendig

facies) the LLST consists mainly of coarse-grained, poorly sorted pumice and lithic breccias with intercalated ash and pumice lapilli fallout. The Mendig facies is rich in large ballistic blocks, that wane in abundance further eastward. There the fallout gets less lithic-rich and more well-sorted (e.g. pit south of Nickenich, so called Nickenich facies). Both facies types gradually merge from west to east, indicating a contemporaneous deposition of both. The LLST fallout ends with a prominent, regionally widespread double layer rich in Devonian slate lithics (so called “slate double” or “double Devonian slate layer”; DDS). The DDS marks the end of LLST and the first Plinian phase of the LSV.

The following section (MLST) can be divided into three major substages labeled MLST A, B and C. The first of these three substages (MLST A) consists of interbedded lapilli and ash layers and lithic-rich breccia beds. Both bed types contain dense to vesicular pumice clasts. Abundant ballistic blocks are a common feature in the proximal Mendig facies. The main distribution direction of the MLST A is towards the southern direction (Bogaard and Schmincke, 1984). The deposits reflect that the eruption style in this stage was an alternation of predominantly phreatomagmatic explosions (fine ash and lithic-rich breccia beds) with distinct Plinian pulses.

The next eruptive stage (MLST B) started with the major ash flow generating phase of the LSV eruption and an onset of a northward migration of the vent (Boogard and Schmincke, 1984). The ash and pumice flows (local term: Trass) of this phase were channeled and ponded in radial pattern in the paleovalleys around the pre-Laacher See basin. The deposits are massive, unwelded ignimbrites, up to tens of meters thick in the valleys and thin coignimbrite ash layers off the valleys. The ash flows or their overbank pendants (Schumacher and Schmincke, 1990) are sandwiched between pumice lapilli beds, representing a fallout from the repeatedly collapsed eruption column.

The MLST C subunit is a Plinian fallout sequence of well-sorted pumice with intercalated brown ash deposits. The pumice differ significantly from the beds below containing more phyric, dense and green-gray pumice clasts with upward increasing abundance in the sequence, cumulating in the prominent dense gray dominated MLST-C3 layer. This widespread MLST-C3 layer marks the end of MLST.

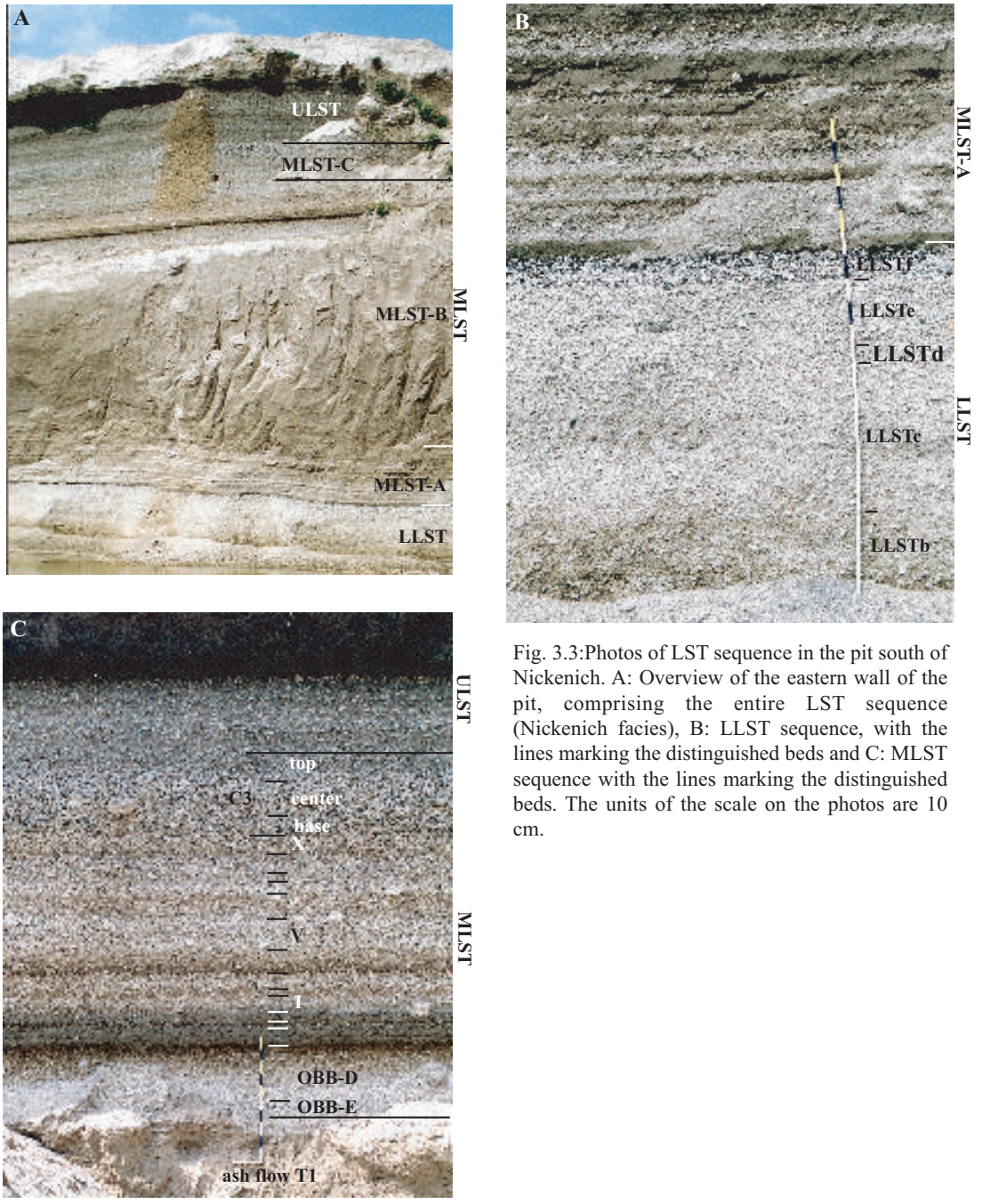

Fig. 3.3:Photos of LST sequence in the pit south of Nickenich. A: Overview of the eastern wall of the pit, comprising the entire LST sequence (Nickenich facies), B: LLST sequence, with the lines marking the distinguished beds and C: MLST sequence with the lines marking the distinguished beds. The units of the scale on the photos are 10 cm.

The ULST is the deposit of the last phreatomagmatic phase of the LSV. It consists of lapilli breccias, massive ash flow or lahar deposits, strongly duned beds and laminated ash and silt beds. The ULST is characterized by a fining upward sequence indicating an intensification of fragmentation, maybe accompanied with a declining eruption column height towards the end of the LSV eruption. The ULST is a major part of the Laacher See basin ringwall, with a thickness up to 35 m, and is deposited in 6 fans spreading radially from the eruption center.

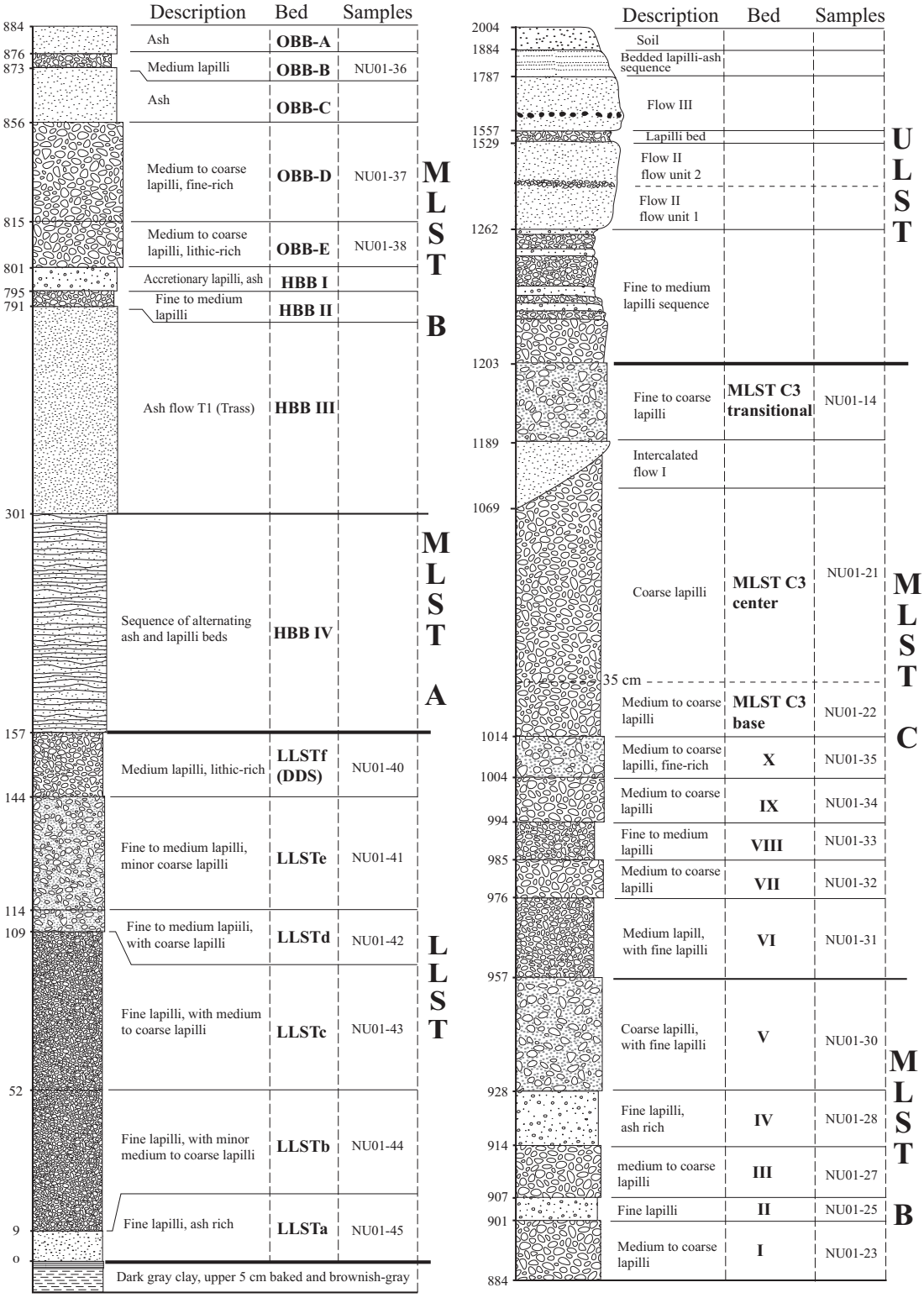

Fig. 4.2: Schematic section of the stratigraphy of LST in the Nickenich Pit. Included are a short description of the main depositional characteristics (for detail see field descriptions in Appendix), the bed names also used in the text and samples numbers of the beds disussed in text.

This study focuses on the fall deposits of LLST, MLST-B and C, sampled in detail at a pit south of the village of Nickenich (Figs. 4.1 and 4.2). This locality was chosen because it was possible there to sample the entire LST sequence and it is located close to the main distribution axis of the LST fallout (Bogaard and Schmincke, 1984). The single fallout beds were distinguished in the field by their depositional characteristics (Fig. 4.3). For LLST six beds were defined this way. The MLST-B/C fallout was subdivided into 16 beds, in part separated by ash flow beds at the base (OBB) and the top of this section (MLST-C3). The ash flow beds embedded in the OBB sequence (OBB-C and A) were not included in the

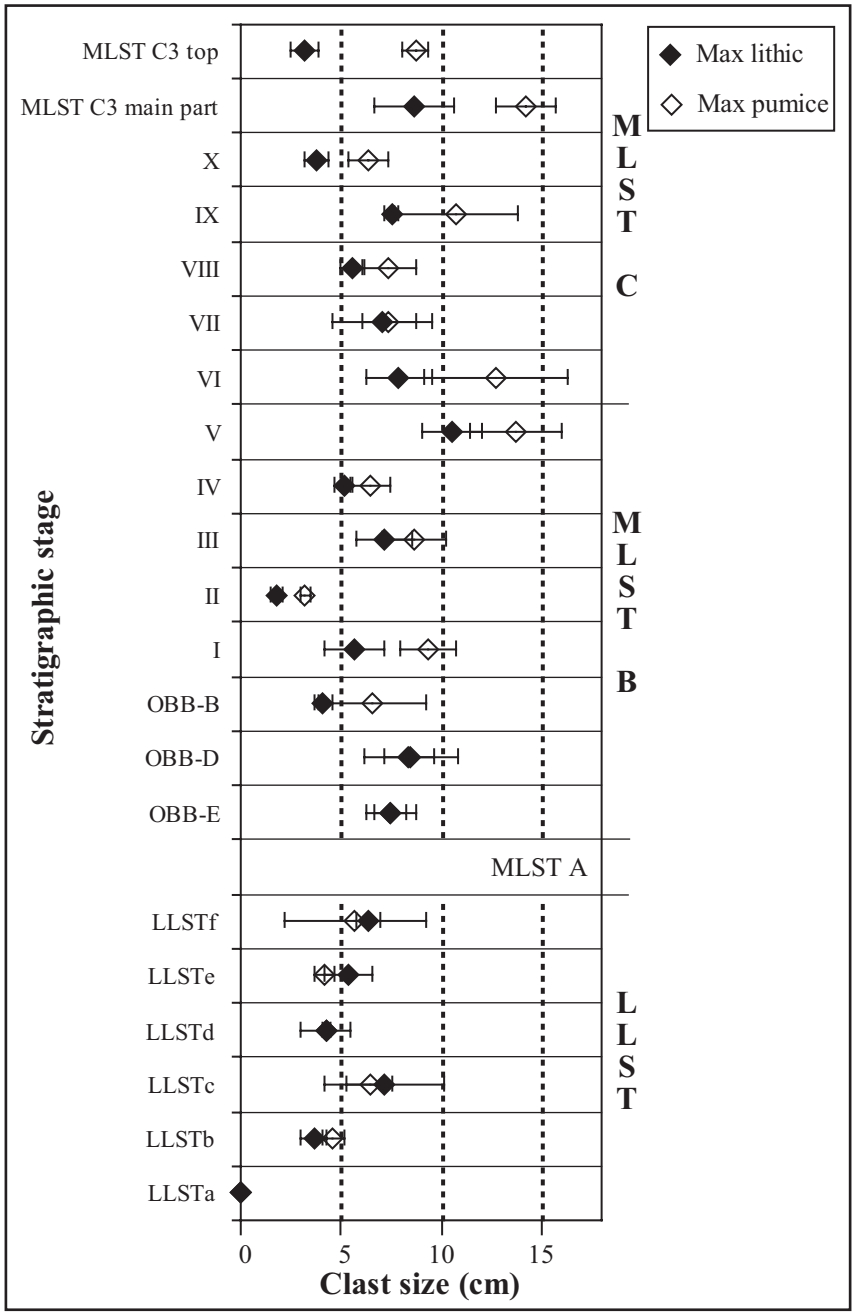

Fig. 4.4: Stratigraphic variation of maximum lithic and pumice clast size.

description.

4.1.Results

4.1.1. Granulometric data

Maximum clast size

In the field the maximum clast size (MCS) variations for pumice and lithic clasts were determined in the pit south of Nickenich (Figs. 4.1 and 4.2). The average MCS variations are described for the two major Plinian fallout sequences LLST and MLST-B/C of the Nickenich facies (Fig. 4.4).

LLST

The LLST mean MCS increases in two cycles from LLSTa to LLSTc (pumice: to 6.4 cm, lithics: to 7.2 cm) and from LLSTd to LLSTf (pumice: 2.3 to 5.7 cm, lithics: 2.2 to 6.3 cm).

MLST-B/C

The MCS of the fallout beds in the lower part of MLST-B, being interrupted by ashbeds, shows an increase from OBB-E to D (pumice: 7.5 to 8.5 cm, lithics 7.5 to 8.4 cm) and a following decrease in OBB-B (pumice: 6.6 cm, lithics: 4.1 cm). The upper part of MLST-B and MLST-C beds show an oscillating increase in MCS from bed I to the peak MCS in MLST-B at bed V (pumice: 9.3 to 13.7 cm; lithics 5.6 to 10.5 cm). From this bed on the MCS decreases again towards bed VIII (pumice: 7.4 cm, lithics: 5.6 cm). The MCS oscillates while it increases to the MLST-C peak in the center of the C3 bed (pumice: 14.2 cm, lithics 8.7 cm), decreasing as it passes into the lower beds of the ULST (pumice: 8.7 cm, lihtics: 3.3 cm).

Grain size distribution

The grain size dirstribution (GSD) was determined for each bed sampled in the pit south of Nickenich. The data for LLST and MLST-B/C are both shown as original GSD and recalculated GSD (Chap. 3.1.1).

LLST

The GSD of LLST (Fig 4.5a) shows an coarsening upwards trend with the peak shifting upward from Φ -1 in LLSTa-c to Φ -3 in LLSTf and a decreasing fines tail. The recalculated and combined GSD emphasize this trend. The combined and pumice GSD show that the Φ -

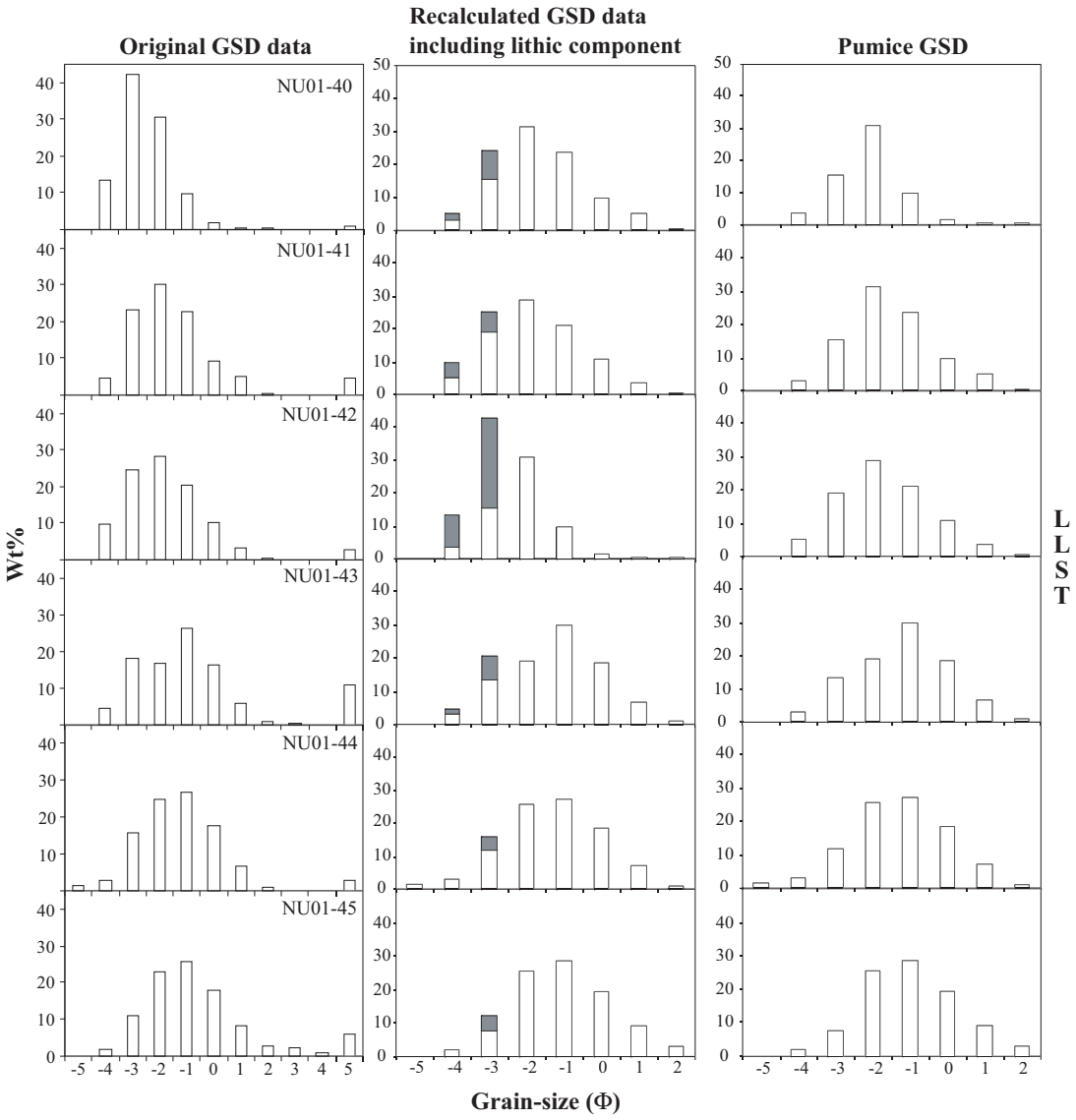

Fig. 4.5a: Stratigraphic variation of GSD of LLST. The gray columns represent the lithic component of the GSD in all plots.

3 peak in LLSTf is caused by abundant lithics in this layer. The peak of the pumice GSD only shifts from Φ -1 to Φ -2 in the LLST section.

MLST-B/C

The GSD of the OBB in MLST-B shows no clear peak but a broad triple peak at OBB-E ranging form Φ -4 to -2 (Fig. 4.5b). This triple peak reduces to a double peak in OBB-D and B comprising Φ -3 and -2. A fines tail develops upwards in this three layers. The recalculated GSD also displays this fines tail development. In the combined GSD the triple and double peaks can be attributed to lithics and in the pumice GSD a constant, single peak at Φ -2 exists in all layers. The fines tail is still displayed in the pumice GSD.

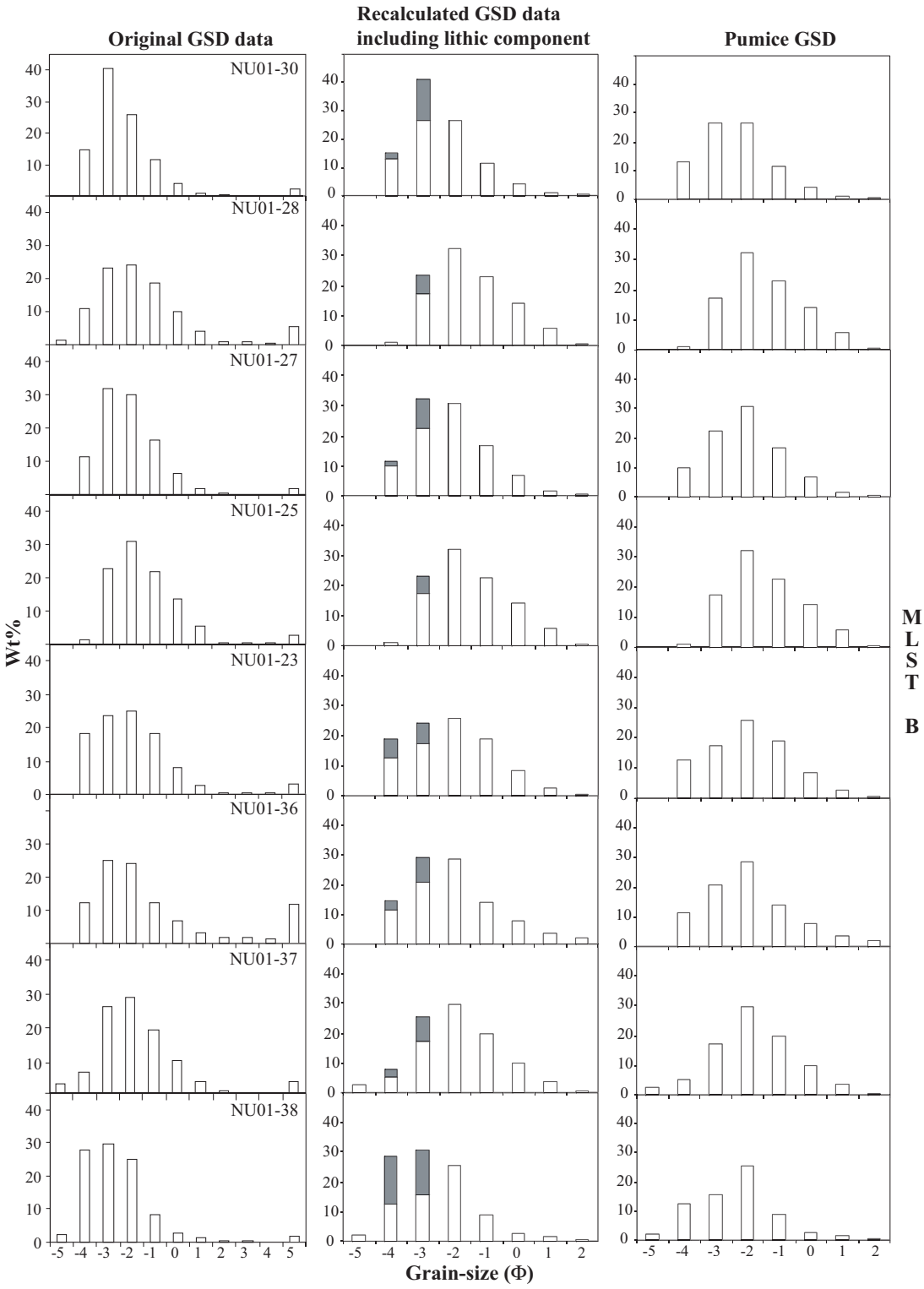

Fig. 4.5b: Stratigraphic variation of GSD of MLST-B.

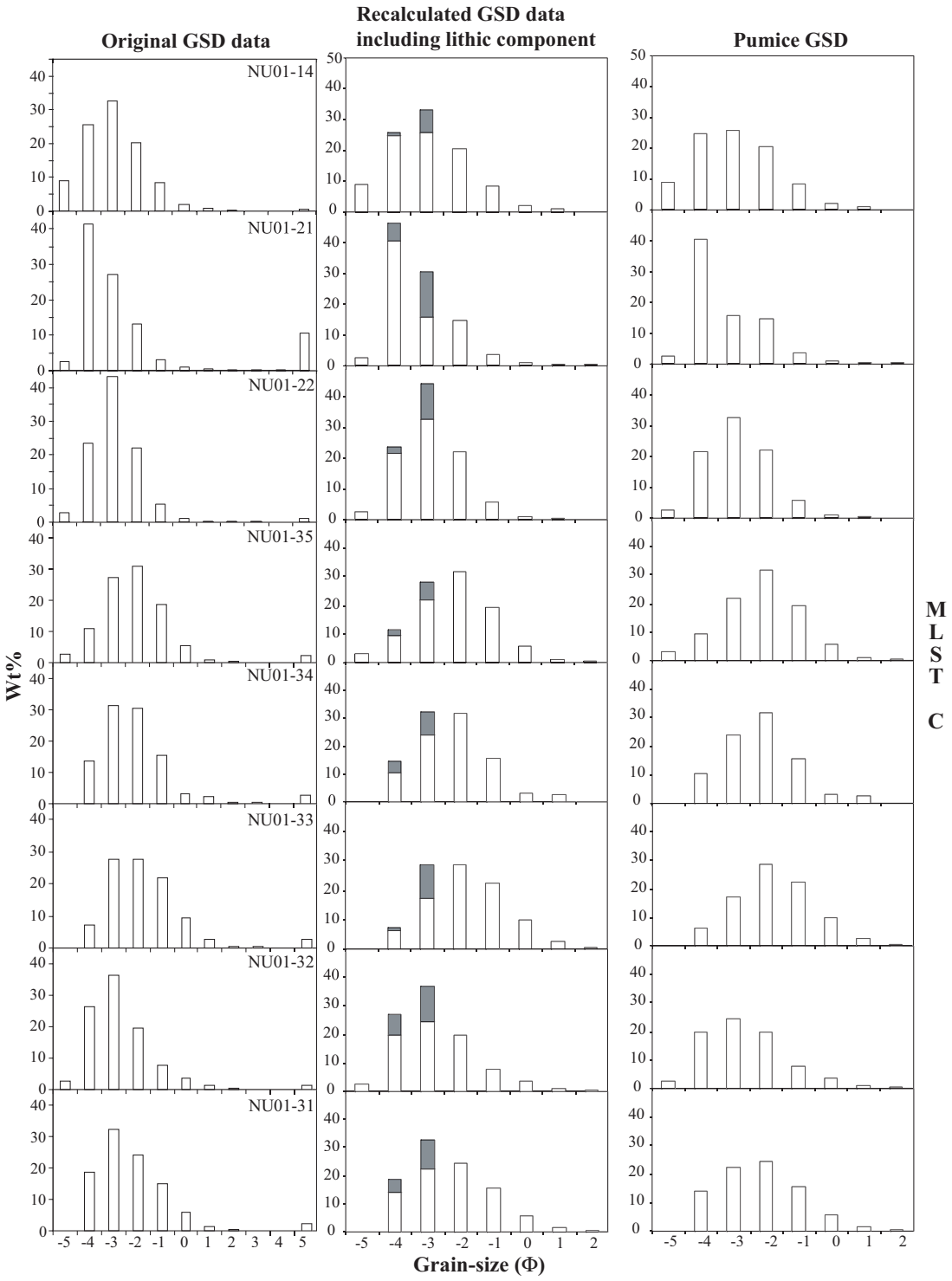

Fig. 4.5c: Stratigraphic variation of GSD of MLST-C.

The MLST-B/C section above the last ash flow bed (Figs. 4.5b and 4.5c) shows an oscillation between a double peak comprising Φ –3 and –2 and a single peak at Φ –2 that moves to Φ -3 at the transtition from MLST-B to C (bed V to VII). This single peak gets broader including Φ -2 in beds VIII to X, with a slight peak at Φ -2 in bed X. The peak jumps to Φ -3 at the base of MLST-C3, moves to Φ -4 in its center and shifts back to Φ -3 at the top above an intercalated ash flow. Fines tails exist only in the ash and fine lapilli rich beds, as are beds II and IV.

Recalculated GSDs emphasize the absence of fines tails except beds II and IV. The combined GSD and resulting pumice GSD show that the oscillation towards broader peaks can be attributed to the lithic component. The pumice GSD show a stable peak at Φ -2 from that gets broader including Φ -3 upwards and shifts to Φ -3 and back to Φ -2 during MLST-C. The peak in the base to center of MLST-C3 in the pumice GSD behaves as in the original GSD. The peak at the top of MLST-C3 vanishes and becomes a double peak including Φ -4.

Median and sorting

Median and sorting coefficient (Fig. 4.6) were determined from the cumulative GSD plots of both the original GSD data and the recalculated GSD data, comprising only pumice.

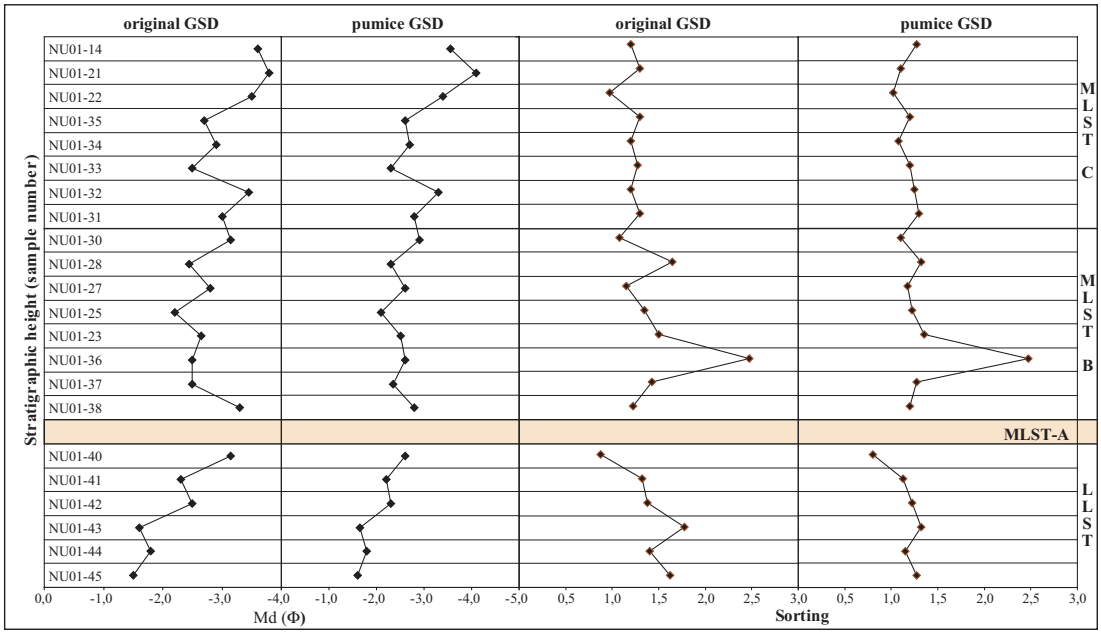

Fig. 4.6: Stratigraphic variation of median and sorting of both original grain size distribution and pumice grain size distribution.

LLST

The median original GSD decreases from LLSTa to c (-1.5 to -1.6) and then abruptly decreases to -2.5 in LLSTd and toward the top to –3.15. The pumice GSD median oscillates between -1.6 to -1.8 from LLSTa to c. Then the median abruptly changes to -2.3 in LLSTd and subsequently decreases to -2.6 at the top.

The sorting coefficient of the original GSD oscillates between LLSTa and c (between 1.4 and 1.8) and decreases from LLSTc on to 0.9 at the top. The pumice GSD sorting coefficient oscillates between 1.1 and 1.3 from LLSTa to c and subsequently decreases from 1.2 to 0.8 from LLSTd on upwards.

MLST-B/C

The median of the original GSD increases abruptly from OBB-E to D (-3.3 to -2.5) and stays stable at –2.5 in OBB-B. In the subsequent sequence the median decreases in an oscillating manner from bed I to bed VII (-2.65 to -3.45), increases in bed VIII (-2.5), decreases towards the center of MLST-C3 to -3.8 and increases again to -3.6 at the top.

The pumice GSD median increases from -2.8 to 2.3 in OBB-E and D and decreases to -2.6 in OBB-D. In the fallout sequence above the median decreases in an oscillating manner from -2.5 to -3-3 from bed I to bed VII, increases to -2.3 at bed VIII, decreases towards the center of MLST-C3 to -4.1 and increases again to -3.5 at the top.

The sorting coefficient of the original GSD increases from 1.2 to 2.5 in the OBB sequence. The sorting coefficient decreases in beds I to III from 1.5 to 1.15, peaks in bed IV (1.65), increases in an oscillating manner from 1.1 to 1.3 in the center of MLST-C3 and decreases again to 1.2 at the top.

The pumice GSD sorting coefficient increases in the OBB sequence from 1.2 to 2.5. Throughout subsequent sequence sorting coefficient oscillates between 1.33 and 1.08.

4.1.2. Modal Composition

Modal compositions were determined for the size range >32 mm to 4 mm (Φ -5 to -2) and the data are presented in Fig. 4.7 for 32-16 mm size range (essential lapilli).

The modal analyses focussed on the distinction of lithic clasts and 5 pumice types as are:

Type 1 (pt1): white pumice with large vesicles (>1-2mm), at least two vesicle populations, >50% vesicles, subordinate elongated, mostly ovoid to round vesicles, subrounded to subangular clasts and phenocryst content < 5%.

Type 2 (pt2): white to ligth gray pumice with large vesicles (>1-2mm), at least two vesicle populations, <50% vesicles, ovoid to round vesicles, subangular to angular clasts and phenocryst content < 5%.

Type 3 (pt3): banded pumice with large vesicles (>2 mm), two vesicle populations, <50% vesicles, elongated to ovoid/round vesicles, subangular to subrounded clasts and in part coliform surfaces

Type 4 (pt4): gray-greenish pumice with large vesicles (>1 mm), in part two populations,<<50% vesicles, ovoid vesicles, angular to subangular clasts with coliform, irregular surfaces and phenocryst content >5%.

Type 5 (pt5): white tube-pumice with strongly elongated vesicles.

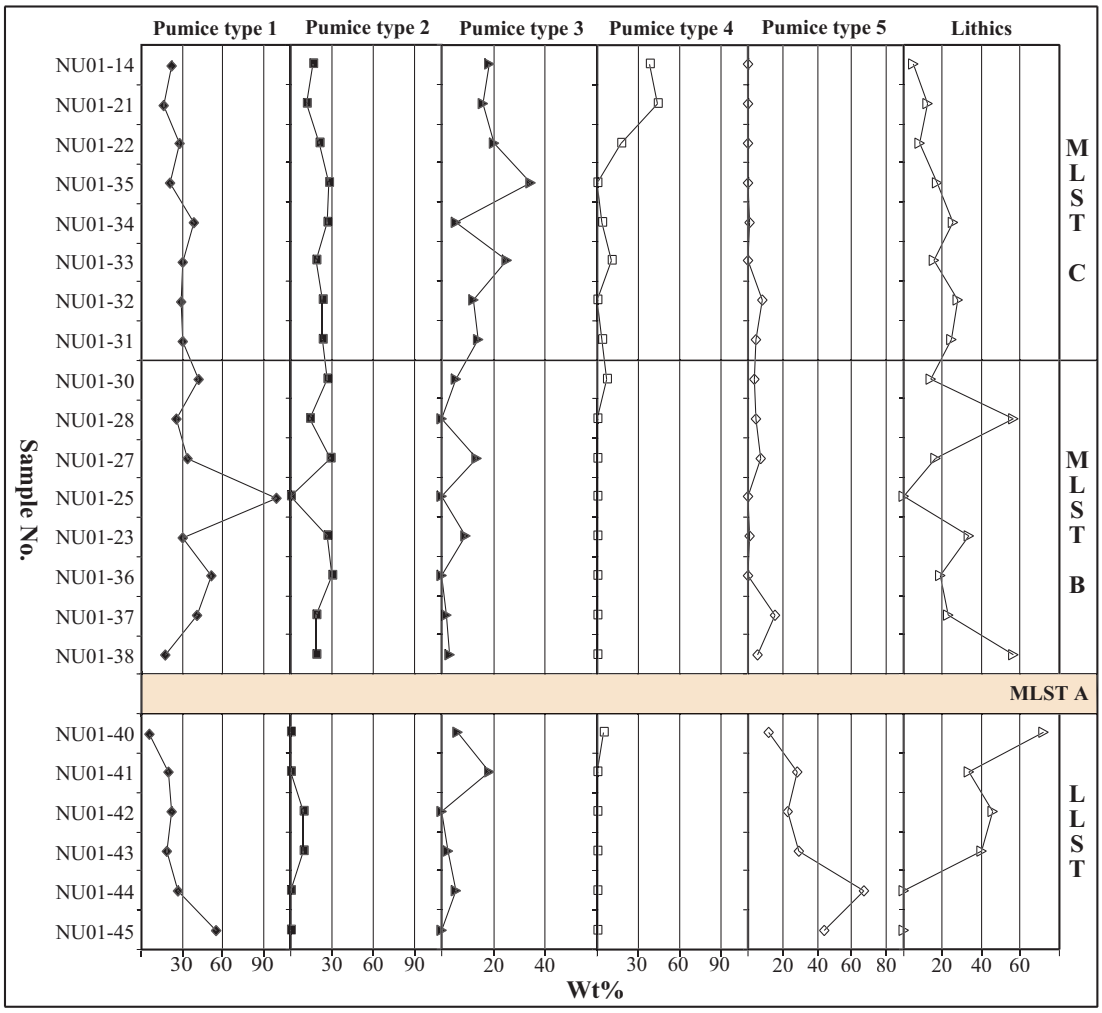

Fig. 4.7: Stratigraphical variation of the modal composition of the essential lapilli size range (32-16 mm).

LLST

The modal composition of the LLST sequence shows a steady upwards decrease in pt1 from 55.5 to 5.3 wt%. Pt2 occurs only as minor component in the center of the deposit (LLSTc and d) with about 9 wt%. Pt3 is rare to absent at the basal LLSTa to d with a maximum of 5.3 wt%, but increases in abundance at the top (up to 18.4 wt%). Pt4 is absent in the LLST except in LLSTf where it occurs with 4.4 wt%. Pt 5 first shows an increase in abundance from 44.5 to 67.3 wt% in LLSTa and b. Then its abundance decreases from 29.6 to 11.9 wt% at the top. Lithics are missing in LLSTa and b and then increase in abundance from 40 to 70 wt% in LLSTc to LLSTf.

MLST-B/C

The OBB sequence in MLST-B shows an increase in pt1 from 17.2 to 50.9 wt% in OBB-E to B. The pt2 abundance also increases from ~18 to 30.5 wt% in OBB-E to OBB-B. Pt3and Pt4 are minor to absent in OBB-E to OBB-B (pt3: 3.3 to 0 wt%). Pt5 increases in abundance from 5.4 to 15.7 wt% from OBB-E to D and is absent in OBB-B. The lithic content of the sequence decreases from 56.1 to 18.6 wt% from OBB-E to B.

The upper MLST-B/C sequence shows a pt1 abundance that varies between ~25 and 42.5 wt%. Exceptions from this compositional range are bed II made up exclusively by pt1 and bed X with a decrease in pt1 abundance to 20 wt%. Pt2 abundance behaves as the pt1 with a range between 13.4 and 28.9 wt%. The pt2 abundance trend only differs in bed X from the pt1 trend, with a slight increase in abundance to 27.6 wt%. The pt3 abundance oscillates between 0 wt% and 13.5 wt% in beds I to IV and increases from 5.7 to 25.3 wt% from bed V to VIII, decreases to 5.4 wt% at bed IX and increases to 34.4 wt% at bed X. Pt4 is absent in the majority of MLST-B, as already in the OBB part, and comes in at its top. From this point on pt4 shows two cycles of coming in and subsequent disappearance, one from beds V to VII (7.1 to 0 wt%) and a second from beds VIII to X (10.2 to 0 wt%). Pt5 is lacking or a subordinate component of this sequence with 0.8 to 8 wt%. The maximum abundance of pt5 of 3.6 to 8 wt% occurs between bed III and VII. The lithic component shows a significant variation only in the MSLT-B part of the sequence as it decreases from 33.1 wt% to zero from bed I to II and subsequently increases to the peak abundance of 56.5 wt% in bed IV. In the MLST-C part of the sequence the lithics abundance displays an almost anti-cyclical behavior as the pt4 abundance with increasing abundance from 13.9 to 27.9 wt% from bed V to VII and from 15.1 to 25.4 wt% in beds VIII and IX and a decrease to 17 wt% in bed X.

The trends in abundance observed in the MLST-B/C sequence below the MLST-C3 layer are not consequently continued in the latter. The pt1 abundance increases to 30.1 wt% at the base then decreases to 18.2 wt% in the center and increases to 23.5 wt% at the top. The similarity of the pt1 and pt2 behavior continues in MLST-C3 with pt2 decreasing abundance from 22.9 to 13.1 wt% from base to center and an increase to 17.6 wt% at the top. The pt3 abundance also shows this decrease in abundance from 22.7 to 18.1 wt% from base to center but then stays almost stable with 19.1 wt% at top. The pt4 is the most significant component in the MLST-C3 layer an increases in abundance from 18.7 wt% at the base to 49.9 wt% in the center and then decreases again to 39.9 wt%. Pt5 is absent in this layer. Lithics follow the trend of pt4 an increase in abundance from 8.1 wt% at the base to 12.5 wt in the center and decrease to 5 wt% at the top.

4.1.3. Density

The density was determined of up to ten pumice clasts of each type and stratigraphic bed of the LST, depending on their availability and occurrence (Fig. 4.8).

LLST

The density of pt1 was determined for LLSTb and LLSTd to f. The density of pt1 increases from 285 to 317 kg/m^3 in this range. The density of pt2 clasts was only determined for LLSTc and d, because other beds lack this type. The determined density decreases upwards from 433 to 377 kg/m^3. The density of pt3 was only determined for the last two beds of the sequence (LLSTe and f) and decreased from 459 to 408 kg/m^3. Pt4 clasts do not occur in significant abundance in LLST to determine their density. The pt5 density was determined throughout the section and shows an increase in two cycles from LLSTa to b (750 to 804 kg/m^3) and from LLSTc to LLSTf (705 to 778 kg/m^3).

MLST-B/C

For density measurements of the OBB part of MLST-B the clasts of all types were not sufficient. So no data is available on the density variation. The upper part of MLST-B shows two cycles of increasing density of pt1 from beds I to III (281 to 350 kg/m^3) and from beds IV to V (306 to 363 kg/m^3). The MLST-C shows a density increase of pt1 from beds VI to the center of MLST-C3 (333 to 413 kg/m^3) and a subsequent decrease at its top (394 kg/m^3). The density of pt2 was determined for almost the entire MLST-B/C section, only lacking data for bed II. The density of pt2 clasts increases from beds I to V (465 to 479 kg/m^3) and increases at the base of MLST-C to 502 kg/m^3 in bed VI, jumps to 300 kg/m^3 in bed VII and increases constantly to 568 kg/m^3 at the top of MLST-C3. The density of tp3 shows an increase in MLST-B from bed III to V (514 to 740 kg/m^3). The density of tp3 increases from beds VII to X (361 kg/m^3 to 944 kg/m^3) and decreases in the MLST-C3 bed from base to top (790 to 490 kg/m^3). The tp4 density was not determined in the major sequence of MLST-B/C and decreases in MLST-C3 from base to top (1.216 to 990 kg/m^3). Pt5 clasts are sparse, therefore only data for beds III (411 kg/m^3), V (856 kg/m^3), VI (496 kg/m^3) and VIII (551 kg/m^3) were determined.

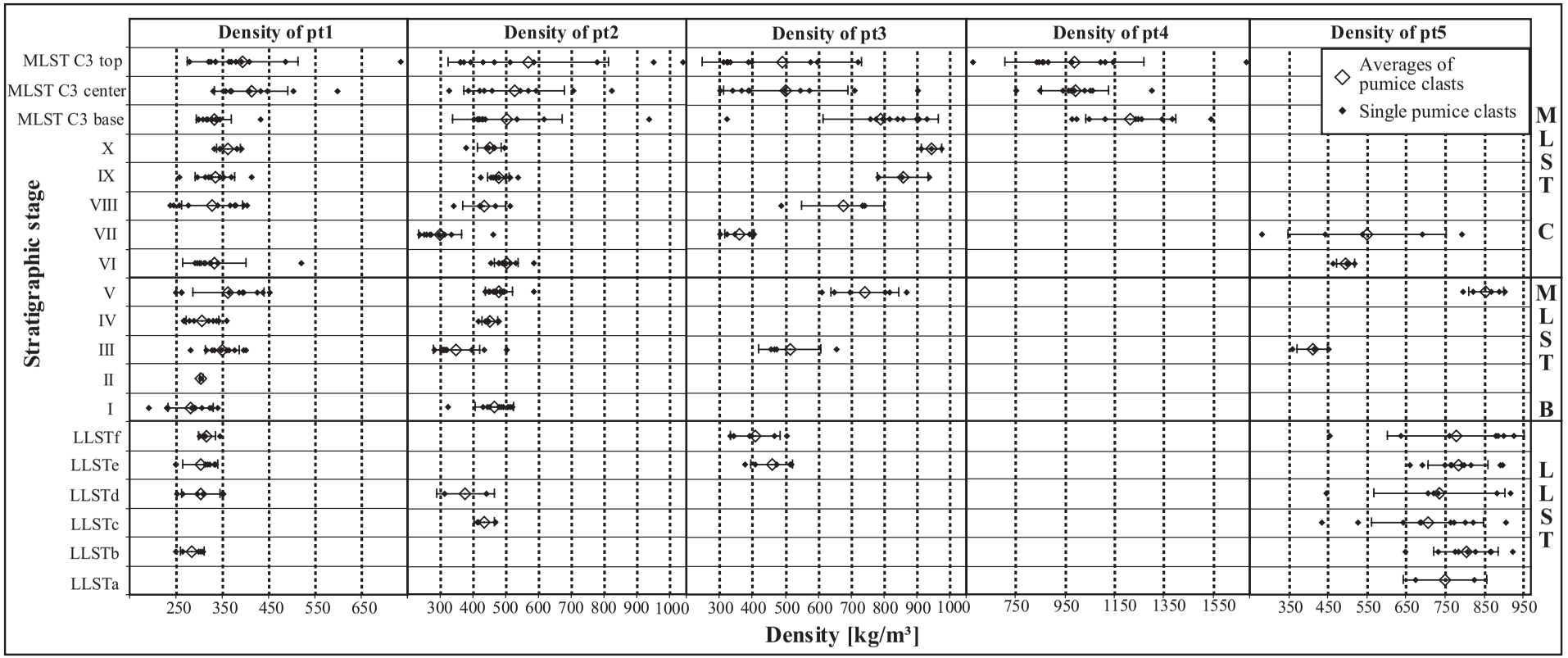

Fig. 4.8: Stratigraphic variation of the density of the 5 distinguished pumice types.

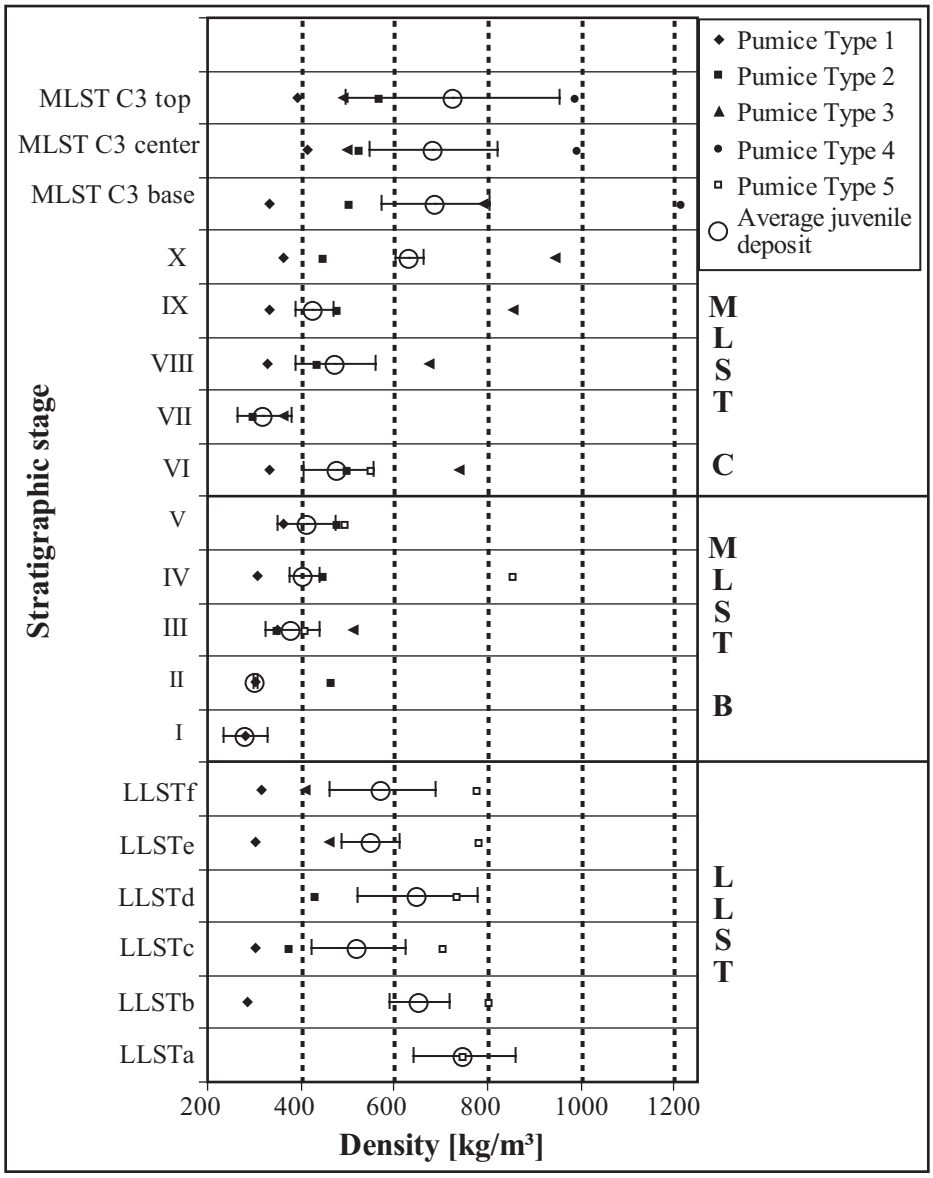

Fig. 4.9: Stratigraphic variation of the weighted average density of the juvenile component of the deposit.

Because of the large variability of the density of the distinct pumice types a weighted average was calculated for each bed (Fig. 4.9). This average represents an approximation of the juvenile component density of the deposit. The calculation based on the sum of the average densities of each pumice type and the corresponding juvenile component relative abundances (wt%): $\rho_{average} = \Sigma\ \rho_{PT}\ abundance_{PT}$. The weighted average displays two cycles of decreasing density in LLST (750 to 522 kg/m^3 from LLSTa to c and 651 to 575 kg/m^3 from LLSTd to f). The minimum average density is observed in bed I (282 kg/m^3) and increases subsequently towards bed VI (480 kg/m^3). Density jumps to a next minimum at bed VII (321 kg/m^3) and increases in an oscillating manner towards bed X (633 kg/m^3). The density increases further in the MILST-C3 layer (690 to 725 kg/m^3).

4.1.4 Shape parameters

The shape parameters (formfactor, solidity and elongation) were determined for the 2-1 mm, unpicked clast size range, as for the Minoan eruption (Fig. 4.10). The method applied is the same as described in the corresponding section (Chap. 3.1.5.).

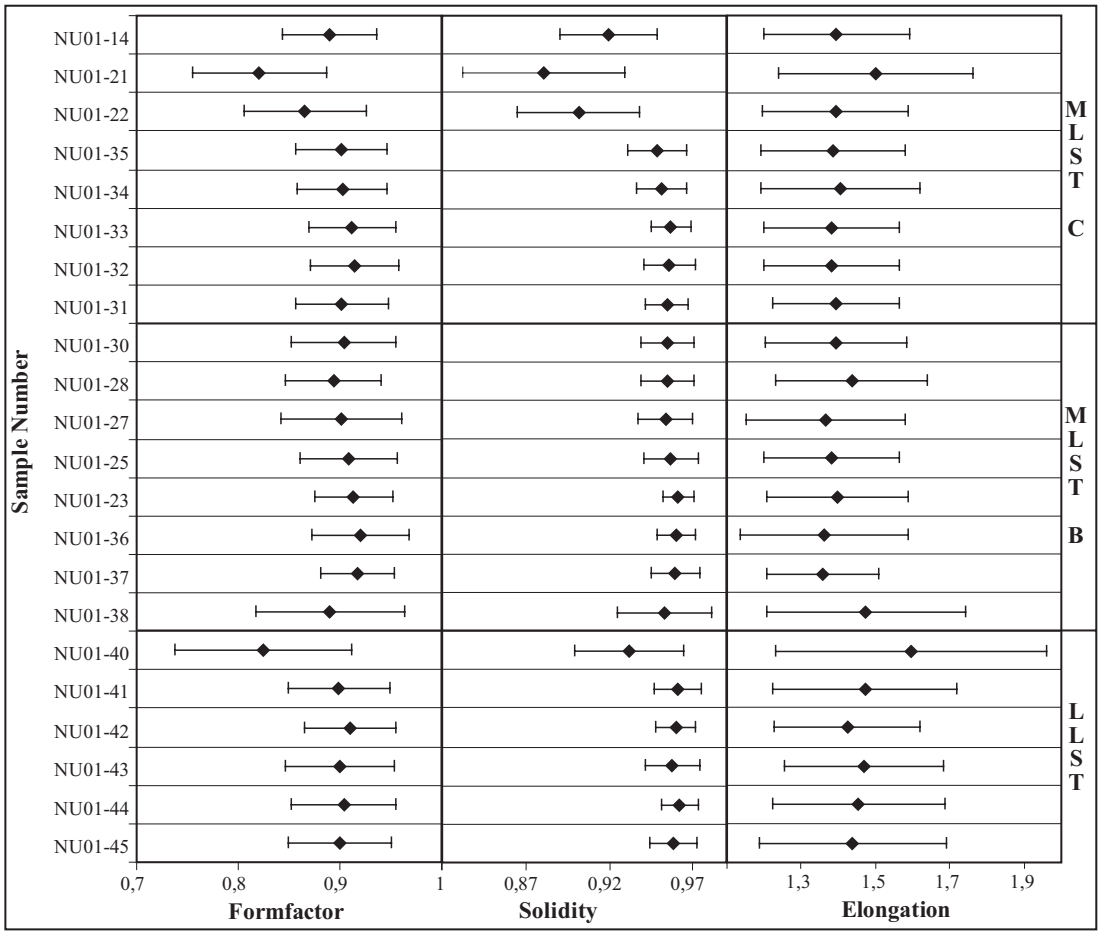

Fig. 4.10: Stratigraphic variation of the pumice clast shape parameters formfactor, solidity and elongation. The standard deviation 2σ is displayed as error bars.

Formfactor

The value of formfactor oscillates between 0.89 and 0.91 from LLSTa to e and jumps to a minimum value of 0.82 in LLSTf, also displaying the maximum standard deviation of 0.09. The value of formfactor increases from OBB-E to OBB-B from 0.89 to 0.92 and decreases from 0.91 to 0.89 at beds I to IV. The value of formfactor increases again from 0.9 to 0.91 from bed V to VIII and subsequently decreases to 0.9 again in beds IX and X. Formfactor in the MLST-C3 layer is decreasing from 0.87 at the base to 0.82 in the center and increases again to 0.89 at the top.

Solidity

The value of solidity oscillates between 0.958 and 0.962 from LLSTa to e and then decreases to 0.932 in LLSTf. The value of solidity increases from 0.953 at OBB-E to 0.96 in OBB-D and B. The value of solidity decreases from 0.961 to 0.954 at beds I to VI then increases to 0.957 in bed VIII. The value of solidity finally decreases to 0.949 at bed X. The value of solidity decreases from 0.9 at the base to 0.88 in the center and increases to 0.919 at the top of MLST-C3.

Elongation

Elongation show the highest values in LLST and increases in two cycles from 1.43 to 1.47 in LLSTa to c and from 1.42 to 1.59 in LLSTd to f. The elongation decreases again from 1.47 to 1.36 from OBB-E to b. Elongation decreases further from 1.39 to 1.36 from bed I to III, jumps to 1.43 at bed IV and subsequently decreases to 1.38 at beds VII and VIII. Elongation increases again to 1.4 at bed IX and decreases to 1.38 at bed X. The elongation in the MLST-C3 layer is 1.39 at the base and increases to 1.5 in the center to decrease again to 1.39 at the top.

4.1.5. Chemistry/viscosity

The chemical variation of the zoned, phonolitic LST is well known for both bulk rock composition (Wörner and Schmincke, 1984) and pre-eruptive volatile contents (Harms, 1998; Harms and Schmincke, 2000). The discussion in this study therefore is based on this published data (Fig. 4.11; Appendix A-2-8).

LLST

The LLST chemical variation is very restricted in comparison to the variation in the entire LST. The SiO_2 and Al_2O_3 slightly increases from 56.6 to 58.5 wt% and 20.9 to 21.6 wt%. The alkalies are most abundant in LLST phonolite and decrease from 12.2 to 11.1 wt% (Na_2O) and 5.83 to 5.76 wt% (K_2O). The 'mafic' elements are most depleted in LLST and decrease upwards in abundance (e.g. CaO from 1.2 to 0.9 wt%; Wörner and Schmincke, 1984). The water content as major volatile component of the LLST matrix glass varies between 0.7±0.4 and 1.2±0.4 wt% and pre-eruptive water content between ~2.4±0.4 and ~4.7±0.4 wt%. No significant water gradient is observed in the Laacher See magma chamber (Harms, 1998). Further the LLST magma represents a volatile enriched (especially in Cl and F) cupola of the LSV magma reservoir (Harms and Schmincke, 2000). The temperature prior to eruption was experimentally determined to be 750-760 °C in LLST (Harms et al., 2003).

The corresponding melt viscosity increases from $6x10^4$ to 10^5 Pas (after Shaw, 1972). The effective viscosity with 5 vol% phenocryst (Wörner and Schmincke, 1984) increases from $8x10^4$ to 10^5 Pas.

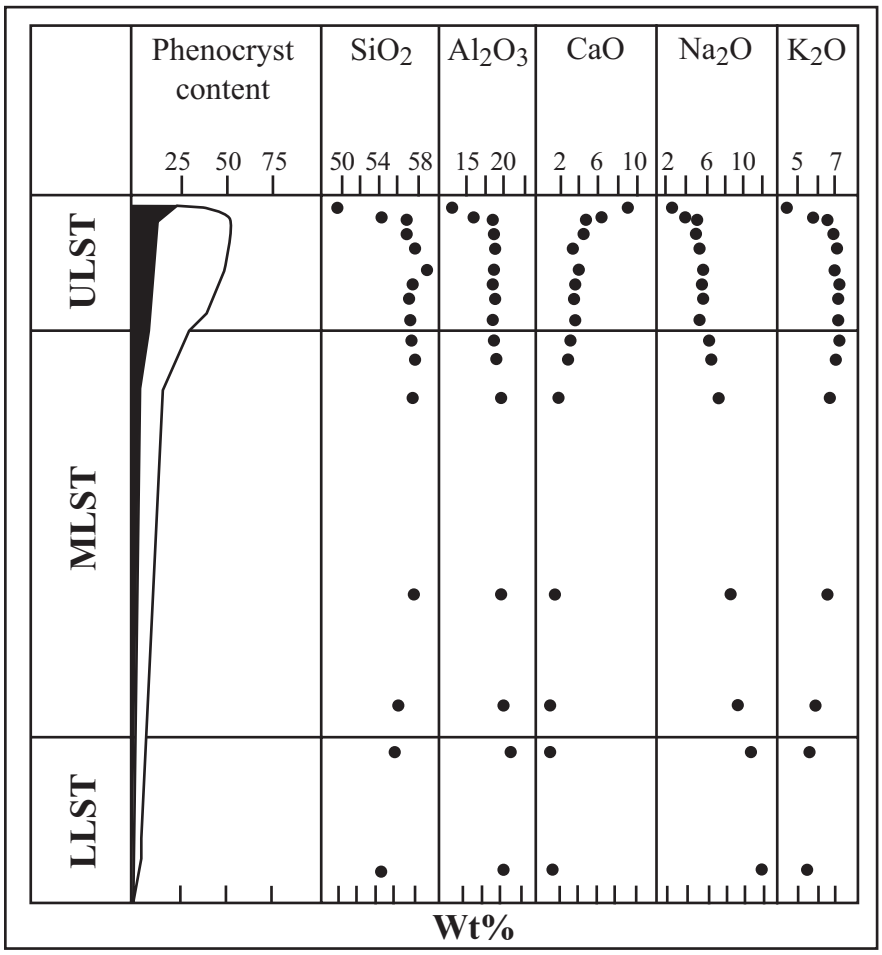

Fig. 4.11: Stratigraphic variation of phenocryst content (black: mafic minerals, white: felsic minerals) and chemical composition after Wörner and Schmincke (1984).

MLST-B/C

The MLST-B/C has a constant chemical composition by the means of SiO_2 (59.4 to 59.7 wt%). The Al_2O_3 content decreases from 20.6 to 19.3 wt% and Na_2O from 8.9 to 6.5 wt% while CaO increases from 1.45 to 2.7 wt% and K_2O from 6.6 to 7.3 wt% (Wörner and Schmincke, 1984). The water content of the MLST-B shows the same concentration range as the LLST at its base but increase in water content upwards to 1.4±0.4 wt% at its top and to 1.4±0.4 to ~2±0.4 wt% in MLST-C. The pre-erutpive water content varies between ~1.6±4 and 5±0.4 wt% (Harms, 1998). The pre eruptive temperature was estimated to be 760-780°C in MLST (Berndt et al., 2001). The corresponding melt viscosity of the samples analyzed by Wörner and Schmincke, 1984 ranges from $3x10^4$ to $9x10^4$Pas for an average temperature of 770°C. The effective viscosity ranges from $5x10^4$ to 10^5 while the phenocryst content constantly increases from ~8 to ~15 wt% (Wörner and Schmincke, 1984).

4.2 Discussion

4.2.1. Intensive parameters of the eruption

Eruption column height evolution

The maximum eruption column height was determined by Bogaard (1983) using the empirical equation of Wilson (1980) that links the mass eruption rate to the eruption column height (see Chap. 3.2.1.). The mass eruption rates of $3x10^8$ kg s^{-1} (LLST) and $5x10^8$ kg s^{-1} (MLST-B) yield an eruption column height of 34-39 km (Bogaard, 1983). The eruption column height was recalculated (Harms, 1998) applying the method of Carey and Sparks (1986), based on maximum lithic size isopleth maps of the proximal LST sequence (Staps, 1976; Risse, 1976; Knoop, 1981; Bogaard, 1983). The resulting maximum eruption column heights proposed by Harms (1998) are 25 km for the Plinian phase of LLST and 20-22 km for MLST-B. The recalculation of Harms (1998) is of significance concerning the climatic impact of the eruption by the means whether it penetrated the stratosphere or not.

The variation of the eruption column height was calculated based on the latter data and the variation of the maximum lithic clast size (see Chap. 3.2.1.). During the Plinian phase of LLST the eruption column height (Fig. 4.12a) rapidly increased from 12.7 km (LLSTb) to the peak height of 25 km (LLSTc). Thereafter it decreased briefly to 14.7 km (LLSTd) and increased to 22 km at the end of LLST. This shows that the eruption column height rose rapidly to its maximum, oscillated a bit and rose until the end of the Plinian phase of LLST.

At the beginning of the MLST-B (the OBB section) the eruption column height increased from 14.3-15.7 km to 16-17.5 km first an then decreased to 7.8-8.6 km at its end (Fig. 4.12a). The main MLST-B eruption was characterized by an eruption column that successively rose while it oscillated between 3.4-3.8 and 10.7-11.8 km until it reached the peak height of 20-22 km (bed V). The low standing column phases were accompanied by the deposition of ash in the section studied, representing repeated partial collapses of the eruption column and resulting ash flows that were channeled in the paleovalleys surrounding the Laacher See basin. Therefore the ash rich beds and thin ash flow beds at the top of OBB can be interpreted as overbank or co-ignimbrite facies (Schumacher and Schmincke, 1990). The corresponding ash flows were deposited eastward in the Krufter Ofen and Mendig fan (Bogaard and Schmincke, 1984).

The calculation was extrapolated into the MLST-C sequence based on the maximum of 20-22 km: this extrapolation indicates that during MLST-C the eruption column height (Fig. 4.12a) first decreased from 15-16.5 km (bed VI) to 10.6-11.7 km (bed VIII) and then started oscillating (between 7.2-7.9 and 14.3-15.8 km) while it increased to the MSLT-C peak

height of 16.5-18.1 km during the main phase of MLST-C3. At the end of the MLST-C3 the eruption column height waned to 6-6.6 km. The absolute values given for the MLST-C eruption column variation are estimates, because the maximum lithic clast size variation may also be caused by a shift in the distribution axis of the fallout fan (e.g. by changing wind field; Carey and Sparks, 1986). But the relative variation can be used to deduce the behavior of the column height that decreased first and started to oscillate during the second half. The cause of the decrease and oscillation in eruption column height resulted from both changing conduit processes (discussed later in more detail) and partial column collapse at the end of MLST-C phase. The partial collapse can be concluded from the intercalated ash flow at the top of the MLST-C3 bed and the fines rich layer (Bed X), accompanying the phases of low standing eruption column height.

4.2.2. Conduit erosion

The evolution of the conduit can be deduced from both the lithic component composition and the modal composition lithic abundance variation of the deposit, with the latter giving a hint on the erosion intensity in the conduit.

The lithic component composition was determined by Bogaard and Schmincke (1984) who interpreted the shift from predominantly “Hundrückschiefer facies” slates and tephritic lava during LLST and MLST-A to predominantly “Siegen facies” during MLST-B and ULST as a northward migration of the eruption center at the beginning of MLST-B eruption. This migration was accompanied by the deposition of ash flows (especially during OBB phase) and a strongly oscillating eruption column height.

The total lithic abundance points toward two major episodes of enhanced conduit erosion or collapse during the Plinian phases of the Laacher See eruption (Fig. 4.12b). The first phase started shortly after the onset of the LLST Plinian phase, with increasing erosion intensity during this phase, cumulating in DDS layer (LLSTf). The increase in lithic abundance was accompanied by an increasing mass eruption rate, thus a lithic enrichment effect can be denied. This even indicates that the supply of lithic clasts into the erupted mixture outranked the dilution effect of the increased mass eruption rate (Varekamp, 1993).

The second phase of high lithic abundance is at the beginning of MLST-B (OBB-E) with an upward decrease in lihtic abundance (Fig. 4.12b). This phase was shortly after the assumed conduit migration and was preceded by an eruption phase generating ash flows (“Trass” ash flows). Two interpretations of the increased lithic abundance are possible. First the northward migration of the conduit marks a phase of intense lateral erosion and opening of a new pathway for the ascending melt. Second the intense ash flow eruption prior to OBB

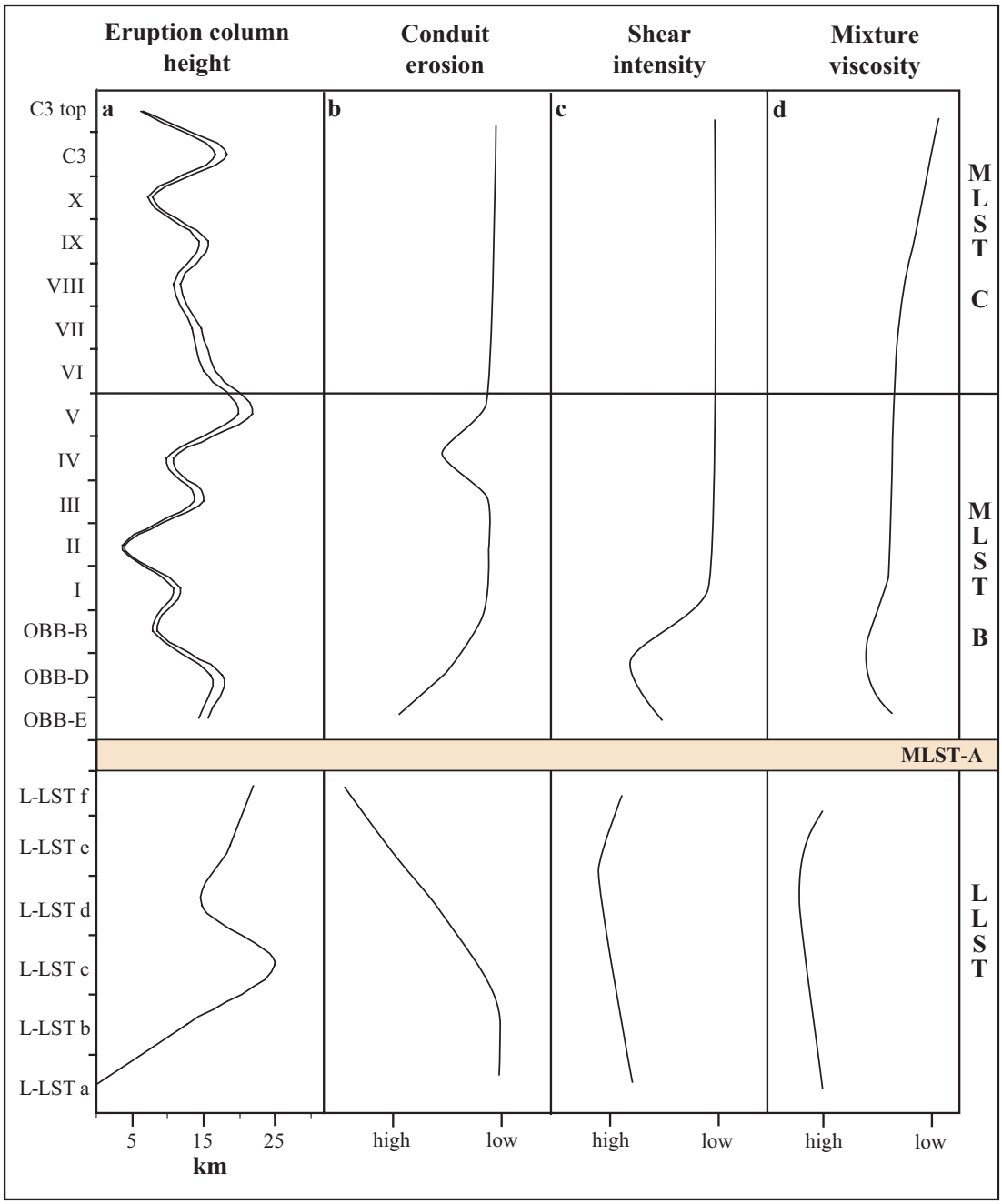

Fig.4.12: Temporal variation of intensive parameters (a: eruption column height) and conduit flow parameters (b: erosion; c: shear inensity; d: melt-gas mixture viscosity). The bed names are given as equivalent of the temporal development of the eruption.

possibly caused a partial filling of the conduit with material that fell back into the conduit during this phase. Subsequently this was eroded during the reopening of the conduit at the onset of the MLST-B Plinian phase. Maybe this partial filling led to the onset of conduit migration during MLST-A/B. Another brief phase of lithic enrichment occurred near the end of MLST-B (Bed IV) and preceded a phase of major change of the erupted pumice population with increasing dense gray (pt4) and banded pumice (pt3) abundance (Fig. 4.7). Therefore it is concluded that the onset of admixing the MLST-C melt component in the conduit altered the flow regime in the conduit and possibly caused a minor conduit collapse

event. During the other phases (MLST B and C) lithic abundance is almost constant at a low level and therefore constant low intensity conduit erosion is assumed (Fig. 4.12b).

4.2.3. Rheology and conduit flow

Information about the variation of the melt rheology and conduit flow can be gained from the mass eruption rate, pumice textures and chemistry and the changes in the juvenile clast population and clast shape parameters in the deposit. Information about the degassing of the rising melt can be deduced from the pumice vesicularity. Combination of the textural data with the chemical variation give an estimate of the viscosity changes. The mixture viscosity and shear intensity changes in the conduit can be deduced from the modal variation of the juvenile clasts and the shape parameter changes.

Shear intensity in the conduit

The tube-pumice abundance is significantly higher during the LLST and the beginning of MLST-B (OBB) eruption phases. During LLST the tube-pumice occurred at high abundance from the beginning of the Plinian eruption on and increases upwards with the peak abundance during LLSTe and decreases in the LLSTf (DDS). This indicates that the shear intensity was high throughout this phase with its peak shortly before the significant erosion event that led to the lithic rich bed marking the end of this phase (Fig. 4.12c). This is supported by the higher elongation and lower formfactor of the clasts of this phase in comparison to the later phases. The maximum of elongation respectively minimum of formfactor and solidity in LLSTf are not corresponding to the assumed shear intensity evolution in the conduit and may therefore result from secondary processes that took place in the fragmented, lithic enriched jet or in the rising plume. Here the fragile juvenile pumice clasts possibly were exposed to secondary fragmentation by collisions with the dense lithic clasts, resulting in elongated tube-pumice shards. This also explains why this layer shows a wider range in all shape parameters, as can be deduced from the higher standard deviation (Fig. 4.10). In conclusion the entire LLST phase was characterized by enhanced shear intensity that slightly decreased at its end, because of an increasing conduit erosion intensity.
During OBB tube-pumice abundance first shows a significant upward increase followed by a drop off at the end of OBB. This indicates that the shear intensity was higher during the beginning of OBB (Fig. 4.12c). The elevated shear intensity possibly was an effect of the migration of the eruptive center during this phase, e.g. the conduit was narrower while it migrated and widened during the migration process. The clast shape parameters of OBB show no significant deviation from the constant shape parameter values of the MLST-B/C section. The only exception are slightly higher elongation and lower formfactor and solidity

in the lithic rich basal layer of OBB, which shows no increased tube-pumice abundance. Therefore these slight shape parameter deviations at the base of MLAST-B/C are interpreted as a secondary effect like that assumed for the LLSTf layer shape parameters. A second bed with comparable clast shape parameter deviations occurs near the end of MLST-B (Bed IV). A secondary effect is also taken into account for this bed, because of low tube-pumice and high lithic abundance.

During the subsequent MLST-B and C Plinian phase tube-pumice was only erupted at low abundance or was absent. Therefore, it is assumed that the shear intensity was at a low level compared to LLST and OBB (Fig. 3.12c). Also the clast shape parameters show no significant variation, except bed IV described above. The shape parameter variation during the MLST-C3 is interpreted to be not a result of magmatic processes. It is assumed that during this phase external water played a significant role, influencing the fragmentation process (Rosenbleck, 1990). This resulted in the eruption of predominantly angular, dense pumice clasts (pt4) and also explains the deviation from the mean clast shape parameter values, especially formfactor and solidity, of the preceding phases. Further the increased density of the erupted pumice enhanced the secondary effects described for the lithic rich beds with altered clast shape parameters.

Degassing

The average density variation of the LLST shows a decrease in the lower three beds (Fig. 4.9) indicating an increase in the degree of degassing during the approximately first half of this eruption phase. The enhanced degassing of the LLST magma is also supported by the low volatile content determined in the matrix glasses of LLST (Harms, 1998; Harms and Schmincke, 2000). Only fluorine showed a restricted degassing behavior in comparison to other volatile elements (Harms and Schmincke, 2000). An increase in average density following the maximum of the degree of degassing described above suggests that the grade of degassing slightly decreased again towards the end of the LLST phase. The high abundance of tube-pumice indicates that the capability of gas to flow out of the melt was very high in the conduit during the entire LLST phase.

The MLST section in contrast starts with low average density increasing successively upwards towards bed VI indicating the degree of degassing decreased upwards, in agreement with the conclusion of Harms and Schmincke (2000) that the Plinian phases of the LSE were characterized by higher degree of degassing than the phreatomagmatic phases. Then the average density decreases significantly to increase again towards the end of MLST. This latter increase is interpreted as the increasing influence of external water on the eruption that restricted the degassing of the melt by quenching it before it significantly vesiculated. This interpretation is supported by the increasing abundance of gray, dense pumice clasts (pt4) in

the deposit, representing the part of the ascending magma being quenched before it vesiculated significantly.

Viscosity

The viscosity of the ascending melt in the conduit is controlled by several factors such as composition of the melt (both magma chemistry and mixing ratio of the different magmas involved), water content (degassing), vesicularity and crystal-content. Therefore information about the variation in viscosity can be gained roughly from pumice chemistry and textures.

1. The chemical variation of the melt erupted during the Laacher See Plinian phases strongly influenced the viscosity. It results in a viscosity ranging between $3x10^4$ and 10^5 Pa s, being almost one order of magnitude. The chemically induced viscosity variation shows that the melts viscosity increased in the course of the LLST from $6x10^4$ to 10^5 Pa s (after Shaw, 1972). Further it is concluded from the pre-eruptive volatile contents (Harms, 1998; Harms and Schmincke, 2000; Harms et al., 2003) that the LLST magma represents a volatile enriched cupola of the magma reservoir. Especially the observed high fluorine content of glass inclusions (690-4060 ppm) and its restricted degassing behavior (Harms and Schmincke, 2000) indicate a reduction of the LLST magma viscosity (e.g. Lange, 1994). If fluorine was more enriched at the top of the cupola it possibly led to an amplification of the viscosity increase during this phase. During MLST the melt viscosity first decreased from $9x10^4$ Pa s at the beginning of MLST-B (Bed II) to $3x10^4$ Pa s at the beginning of MLST-C (Bed VI). In the course of the MLST-C phase the melt viscosity first increased significantly to $8x10^4$ Pa s (Bed X) and decreased again to $5x10^4$ Pa s during the MLST-C3 phase.
2. Next to the chemical variation the crystal content of the erupted magma influences the effective viscosity of the magma in the conduit, increasing the melts viscosity. Incorporation of the increase in crystal content (Woerner and Schmincke, 1984) results in an effective viscosity increase from $8x10^4$ to 10^5 Pa s during LLST Plinian phase. During MLST effective viscosity first decreased from 10^5 to $5x10^4$ Pa s and increased to 10^5 Pa s until MLST-C3.
3. The influence of degassing on the viscosity of the ascending melt must also be taken into account. The effect of the polymerization of a melt during water loss (Sparks et al. 1994; Dunbar and Kyle, 1993) is already included in the chemically induced viscosity variation, but the effect of vesicles in the melt has to be taken into account too. So it is assumed that the high shear intensity and increasing vesicularity during LLST led to a stronger viscosity increase than caused by the chemical variation during this Plinian phase. This viscosity increase, however, was not that large during the last eruptive stage

(LLSTf), because of the decreasing shear intensity. During the MLST the low shear rates in combination with the significant decrease in vesicularity, especially in the dense, gray pumice (pt4) component with >50 vol% vesicles, indicates that during this phase the viscosity dropped significantly (e.g. Llewellin, 2002), possibly outranking the effects of chemical composition and increasing crystal content. Therefore it is assumed that this vesiculation induced viscosity drop was most effective at the end of MLST-C.

4. Next to the effects of chemical composition, crystal content and vesiculation of the melt, the mixing of different melts in the conduit influenced the viscosity. Therefore it may be assumed that at the end of LLST the admixing of a second melt component (deduced from higher banded pumice (pt3) occurrence in LLSTe and f) further enhanced the already assumed viscosity decrease. The same is assumed during the MLST-C Plinian phase that was characterized by a significant increase in banded pumice (pt3) and dense gray pumice (pt4) abundance in the erupted clasts. This points towards that extensive mixing took place in the conduit during this phase. The lower viscosity of the MLST-C3 melt therefore possibly caused a drop in the average viscosity in the conduit. This tendency cumulated during the MLST-C3 phase, characterized by the eruption of predominantly dense, gray pumice clasts (pt4) of lower viscosity.

In conclusion it can be assumed that the highest viscosity during the Laacher See eruption occurred during its first phase (LLST) with an increase at its beginning followed by a slight decrease at its end. During MLST the viscosity was lower because of a) the altered chemical composition and b) the increasing importance of admixing of a less vesiculated melt in the conduit (Fig. 4.12d).

4.2.4. Fragmentation intensity

The pumice GSD based median represents the clast population generated at the fragmentation horizon and is therefore a measure for the fragmentation intensity, save for the lithic enriched layers that experienced extensive secondary fragmentation. Based on these data (Fig. 4.6) the fragmentation intensity decreased during the LLST Plinian phase. The first decrease in fragmentation intensity took place after approximately the first half of the eruption and was followed by a further gradual decrease during its second half. The fragmentation style was predominated by strain-induced brittle fragmentation (Papale, 1999) during LLST, because of the high shear intensity during this phase.

The fragmentation intensity increased in two cycles at the beginning of the MLST Plinian phase (OBB-E to D and OBB-B to bed II). Afterwards it decreased in an oscillating manner during the subsequent MLST-B and the beginning of MLST-C phases (Bed III to VII) and showed a first minimum fragmentation intensity at the end of this cycle. This minimum was followed by a sudden fragmentation intensity increase and a subsequent decrease. This decrease led to an absolute minimum in fragmentation intensity during MLST-C3 main phase. The final phase of MLST-C3 was characterized by an increase in fragmentation intensity, marking the transition to the phreatomagmatic ULST, displaying high fragmentation intensity. The fragmentation style was predominately ductile during MLST-B/C, except a brief phase at the beginning (OBB), that displayed elevated shear intensity and thus a higher proportion of brittle fragmentation.

4.3 Conclusion

LLST

The LLST represents the first Plinian phase of the LSE. It is characterized by predominant eruption of tube-pumice and thus a high shear intensity during the entire phase that slightly decreased during the phase. This shear intensity decrease occurred contemporaneously with an increase in the deposits banded-pumice abundance, general viscosity decrease and conduit collapse at the end of the phase. All these changes resulted in an alteration of the magma rheology and a drop in shear intensity, by reducing the friction at the conduit wall. The volatile enrichment of the cupola, deduced for the LLST magma (Harms and Schmincke, 2000; Harms et al., 2003) has to be taken into account too. Whether the volatiles were enriched in the melt (assumed for F by Harms and Schmincke, 2000) or in a separated fluid phase (assumed for S by Harms and Schmincke, 2000; Schmincke et al., 2000) determines the influence of each volatile phase on the magma viscosity. An extensive water- and fluorine-enrichment in the melt may be responsible for a viscosity lower than the value determined from the chemical variation during LLST Plinian phase. The enrichment of volatile elements in a separated fluid phase would rather cause an elevation of the viscosity and results in higher friction and shear intensity at the beginning of LLST. Therefore, the elevated shear intensity is not in accordance with the assumed water- and F-enrichment in the magma, resulting in lower viscosity. It is assumed that the conduit was still narrow during LLST. The high tube-pumice abundance, next to the average density variation occurring in the deposit indicates a high degree of degassing during LLST that slightly decreased towards the end of this phase. This enhanced degassing of the Plinian LLST phase was already proposed by Harms and Schmincke (2000).

The fluctuation of the eruption column height during the second half of the LLST phase can be taken as expression of the changes in the magma composition (less volatile-enriched magma tapped and admixing of a minor second melt component) rather than influenced by changes of the conduit geometry. The large scale conduit collapse, resulting in the prominent DDS layer (LLSTf) occurred at the very end of the Plinian phase after the eruption column oscillation. The collapse marked a significant change of the eruption dynamics towards a phreatomagmatically dominated style during the MLST-A phase. It is assumed (Schmincke et al., 1990) that the partial evacuation of the magma chamber triggered this change by groundwater gaining access into the magma chamber.

MLST-B

The MLST-B phase started with the eruption of a lithic-rich lapilli bed after a phase of intense ash flow eruption. Further the tube-pumice abundance points towards an elevated shear-intensity at the beginning of MLST-B. This lithic enrichment and shear intensity elevation possibly resulted from the preceding processes (intense ash flow eruption and vent migration) that altered the conduit geometry by partially filling it with material falling back from the unstable flow-generating eruption column and the intense lateral erosion of the conduit while it moved northward. Both effects may have narrowed the pathway for the ascending magma and the obstacle of fragmented wall rock was blown out of the conduit as the Plinian eruption reestablished. This interpretation is supported by the fact, that both lithic and tube-pumice abundance decrease upwards in the upper MLST-B deposit.

During the MLST-B the eruption column height successively increased in an oscillating manner. The low eruption column heights occurred contemporaneously with the deposition of ash- and fines-rich beds and hence is interpreted as the result of partial collapses of the eruption column, generating ash flows, commonly associated with this phase of the eruption (e.g. Schmincke et al. 1990). The section in the Nickenich pit contains no ash flow deposits in the upper MLST-B and the flows are here represented by coignimbrite ashes in the lapilli beds and ignimbrite overbank facies ash beds (Schumacher and Schmincke, 1990). This fluctuating eruption column is concordant with the mass eruption rate of the MLST-B ($4.3x10^5$ to $5x10^5$ kg s^{-1}) being close to the transition of sustained to collapsing eruption column (Wilson, 1980; Bogaard, 1983).

The reason for the change in mass eruption rate and hence eruption column fluctuation may be a lower pre-eruptive water content (~1.6 to 4.4 wt%; Harms, 1998) while the degree of degassing shows a comparable efficiency like during the LLST Plinian phase (Harms and Schmincke, 2000). The degree of degassing, concluded from the average density variation, decreased during the MLST-B phase. This decrease is also displayed by the matrix glass water content increase (from <1 wt% to ~2 wt%; Harms, 1998). These changes in pre-

eruptive water content and degree of degassing are assumed to be the controlling factor of the eruption column stability rather than conduit widening, playing no significant role during the majority of the MLST-B Plinian and ash flow generating phase. Exceptions of the low lithic abundance during the MLST-B phase are the basal layer (OBB-E) and the bed close to the top of MLST-B (layer IV). The latter represents a phase of low eruption column height and mass eruption rate, and therefore may be a enrichment effect, caused by a reduced mass of juvenile material erupted (Varekamp, 1993). A large scale conduit erosion or collapse event can be denied, because the eruption column height subsequently rose and reached its climax one stage later.

MLST-C

The MLST-C phase is characterized by a successive increase in banded pumice (pt3) and dense gray pumice (pt4) abundance that represents a less vesiculated portion of the melt. This low vesicularity is also displayed in the average density development of the deposit. The pt3 abundance increase mainly took place during the beginning of the phase and was accompanied by a decreasing eruption column height, while the significant pt4 abundance increase occurred during the end of the phase, accompanied by an oscillating, slightly increasing eruption column height. Therefore it is assumed that at the beginning of MLST-C a less evolved and less viscous magma was mingled with the more evolved and viscous magma. This intimate mixture strongly affected the conduit flow and eruption dynamics and led to the described wane of eruption column height. The pt3 abundance oscillated significantly as the eruption column height starts to fluctuate. Pt3 abundance was high when the eruption column height was low and pt3 abundance was low when the eruption column was high. This correlation of pt3 abundance and eruption column height shows how effective the mingling of the two magmas affected the eruption dynamics. At the end of MLST-C the less evolved magma (represented by pt4) gained more importance and predominates in C3. The increasing average density of the deposit and abundance of the less vesiculated pt4 points towards an increasing influence of external water on the eruption dynamics. This water access toward the conduit or magma chamber seems to have taken place in pulses, causing the fluctuations of the eruption column height during the C3-phase. The MLST-C phase is therefore interpreted to be rather a phase that successively changed from a Plinian to a phreatoplinian eruption style, following the definition of phreatoplinian eruptions by Houghton et al. (2000) This phreatomagmatic eruption style was continued and dominated the ULST eruption phase.

5. Comparison and models of the Minoan and the Laacher See Plinian eruption

The combination of methods described in this study is a powerful tool to gain detailed insight into the temporal variations of conduit flow and eruption dynamics that take place during Plinian eruptions from homogeneous magma chambers, such as the Minoan Plinian eruption. Furthermore the combination of existing detailed chemical data, including pre- and post-eruptive volatile element variations, with a detailed investigation of the corresponding deposit structures helps to better understand the processes influencing the dynamics of complex Plinian eruptions, such as the Laacher See eruption.

5.1. Comparison of the variation of eruption dynamics

The detailed datasets of both eruptions described in this study allow a comparison of the processes responsible for the changes that took place during the Plinian eruptions. The major properties affecting the eruption dynamics, next to the dynamic changes of both eruptions are summarized below (Tab. 5.1.)

Table 5.1: Comparison of the physico-chemical parameters and eruption dynamics of the Minoan and the Laacher See eruption.

	Minoan eruption	**Laacher See eruption**
Chemistry	• homogeneous major rhyodacitic magma • minor andesitic component with varying chemistry and increase in abundance during eruption	• zoned magma chamber with evolved, volatile rich phonolite at top and mafic, phenocryst rich phonolite at base
Volatiles	• no volatile zonation assumed, about ~6 wt% pre-eruptive water-content	• strongly zoned pre-eruptive volatile distribution • volatile enriched cupola (Harms and Schmincke, 2000)

	Minoan eruption	Laacher See eruption
Eruption column	• nearly constant column height increase during eruption • waned at the end of the eruption	• sustained eruption column repeatedly collapsed, both at the end of Plinian phase LLST and during Plinian phase MLST-B • fluctuating eruption column (MLST-B/C)
Conduit stability	• conduit was stable during first two phases of the eruption • intense conduit erosion/collapse during third phase that significantly shattered the edifice	• conduit collapse at the end of LLST • conduit migration during MLST-A/B (Bogaard and Schmincke, 1985) • possible collapses at beginning and end of MLST-B
Shear intensity	• high during phase 1 • low during phases 2 and 3	• high during LLST and beginning of MLST-B
Viscosity	• mainly controlled by vesiculation, shear intensity and magma mixing in the conduit • no significant chemical control on viscosity variation (less than an order of magnitude)	• chemical zonation and phenocryst content exerted strong effect on viscosity variation (decrease in viscosity of about an order of magnitude during the eruption) • shear intensity, vesiculation and mixing of magma enforced the chemistry related viscosity variation
Degassing	• degree of degassing increased during phase 1 • stable degree of degassing during phases 2 and 3	• high degree of degassing during pure Plinian phases (LLST/MLST-B; Harms and Schmincke, 2000) • degree of degassing was reduced during MLST-B and was lowest during MLST-C

	Minoan eruption	Laacher See eruption
External factors	• external water (seawater) gained access at the end of the Plinian eruption, leading to phreatomagmatic MIN-B phase • volcanotectonic faulting occurred after the MIN-A phase, when the caldera collapse started (MIN-B/C; Druitt et al., 1999)	• external water (groundwater) gained possibly access at the end of LLST, surely during MLST-A • increasing water ingression in the course of MLST-C, leading to the phreatomagmatic ULST phase • volcanotectonic faulting during the phase of vent migration assumed (e.g. Schmincke et al., 2000)

It can be concluded, that the chemical variation of the Minoan rhyodacite magma had only a minor effect on the viscosity variation and hence not affected the eruption dynamics. Hence the conduit dynamics were strongly influenced mainly by the physical properties of the melt. These properties were: 1) changes in the degree of degassing (controlling density of pumice clasts and ascent velocity), 2) shear intensity (controlling effect of vesicles on the viscosity) and 3) admixing of a second andesitic magma in the conduit with a different volatile composition (controlling average viscosity, pressure gradient along the conduit and fragmentation horizon height in the conduit). Conduit erosion, respectively conduit wall or magma chamber roof collapse (controlling mass eruption rate and stability of the edifice) affected the eruption dynamics as additional factor. The variations of these factors were reconstructed in this study and especially the vesicle size distribution data helped to deduce the vesicle nucleation and growth processes, that are controlled by the ascent velocity of the magma.

The Laacher See eruption (LSE) in contrast is characterized by the evacuation of a strongly chemically zoned magma chamber including the volatile enrichment at the top of the magma chamber (Harms and Schmincke, 2000). Thus the chemical variation had a strong influence on the viscosity variation. The resulting complexity of the viscosity variation prevents a clear distinction of the different factors controlling the conduit dynamics. Further the chemically different magmas were not erupted as a successive sequence and mixing of the magmas of different viscosity took place in the conduit, as displayed by the abundant banded pumice in the MLST-C deposit. This mixing affected the eruption dynamics of the LSE and a fluctuating, pulsing eruption column developed. The Minoan Plinian eruption in contrast developed a sustained eruption column that fluctuated not significantly and was rather

sustained throughout the Plinian eruption and even existed during the phreatomagmatic phase (Druitt et al., 1999).

External factors (Tab. 5.1) affected the two eruptions on different scale. The influence of external water played a much more important role during the LSE, being responsible for eruption dynamic shift to a phreatomagmatically dominated style after LLST and at the end of the MLST-C phase. The successively increasing influence of external water resulted in the eruption of low vesiculated gray pumice of increasing abundance and a decrease in the degree of degassing of the magma during the latter phase. During the MPE external water played virtually no role.

The assumed vent migration that occurred during the LSE has no equivalent in the MPE. During the Minoan the conduit was quite stable during almost the entire eruption and only at the end it was widened by intense erosion/collapse, as also suggested before (Taddeucci and Wohletz, 2001; Druitt et al., 1999). The vent migration during LSE occurred mainly during the phreatomagmatic and ash flow generating phases (MLST-A and beginning of MLST-B), and had no significant effect on the Plinian phase dynamics, except the lithic enrichment of the basal MLST-B bed.

The style of fragmentation (ductile or brittle) is difficult to deduce from the deposit. Only an assessment on the basis of the tube-pumice abundance is possible, assuming that they represent the part of the magma that was exposed to higher elongational strain rates close to the conduit walls. This elevated strain rates lead to a transition from ductile to brittle behavior of the melt (shear induced glass transition) when the elongational strain rate exceeds the inverse structural relaxation time of the melt (Papale, 1999). Based on this assumption it can be concluded for both eruptions that brittle fragmentation took place only at the beginning of the Plinian eruption phases (Phase 1 of the MPE; LLST and basal MLST-B in the case of LSE). This is interpreted as an effect of the narrower conduit during the opening phases of the different eruptions. The higher abundance of tube-pumice in the LLST deposit (up to 67 wt%) than in the MIN-A and MLST-B basal deposit (up to ~17 wt%) indicates that brittle fragmentation was more significant during the LLST eruption than during Phase 1 of MPE and MLST-B. This is interpreted as the result of a combination of the higher viscosity of the LLST melt and a narrower conduit. In both eruptions brittle fragmentation declined in importance as the eruptions proceeded and a ductile fragmentation style dominated, except

during MLST-C characterized by a successive shift towards a phreatomagmatic fragmentation style.

5.2. Model calculations

5.2.1. Model input and output data discussion

For both eruptions a set of models was calculated applying the CONFLOW model of Mastin and Ghiorso (2000). The main aim of these calculations was to gain insight into the fluctuation of the fragmentation horizon depth during both Plinian eruptions in dependence on the changes in chemical composition and physical parameters. It is important to note that the CONFLOW model is a so-called steady-state model not allowing to explore e.g. the opening of a conduit system.

All models were calculated a) applying a defined pressure gradient (~25 MPa/km; equal to the lithostatic pressure gradient), b) allowing the melt to cool during conduit transport, c) assuming choked flow conditions at the conduit exit (this means that the exit velocity equals the local sonic speed of the erupted mixture) and d) the "75 vol% vesicles criterion" for fragmentation (Sparks, 1978). All parameters used in the various model calculations are listed in Table 5.2.

Tab. 5.2: Input and output parameter of the model calculations. Physical and chemical input parameters were taken from the literature for the Minoan eruptions (Cottrell et al., 1999; Michaud et al., 2000; Druitt et al., 1999; Heiken, 1987) and Laacher See eruption (Wörner and Schmincke, 1984; Harms, 1998; Berndt et al., 2001; Harms et al, 2003). For a couple of compositions (SE1a, SE1j, LLSTa, LLSTf, II and C3) additional model runs were carried out to explore the mixture density and mass fractions of exsolved gas and magma.

Input parameters	**Minoan eruption**	**Laacher See eruption**
Chemical composition	bulk XRF analyses (this study)	bulk XRF analyses (Wörner and Schmincke, 1984)
Temperature	885°C	720 (LLST) to 770°C (MLST)
Input pressure	50 MPa	135 MPa

Input parameters	**Minoan eruption**	**Laacher See eruption**
Inlet conduit diameter	70 m	30 m
Input velocity at conduit base	1 m/s	1 m/s
Conduit length	2000 m	5500 m
Pre-eruptive water content	6 wt%	4.7 (LLST) to 4-5 wt% (MLST-B and C)
Phenocryst content	4 vol%	5-6 vol% (LLST) and 8-15 vol% (MLST B to C)
Output parameters	**Minoan eruption**	**Laacher See eruption**
	depth	depth
	pressure	pressure
	conduit radius	conduit radius
	volume fraction of gas	volume fraction of gas
	velocity	velocity
	log viscosity	log viscosity
	mach number	mach number

5.2.2. Minoan eruption

According to the model calculations (see velocity profiles in Appendix B-1-1) the fragmentation level depth in the models, representing the ten stages, stayed constant at ~780 m below surface during the entire eruption. This is a result of the constant amount of water dissolved in the melt at depth, pressure and the minor chemical variation preventing a significant change of conduit dynamics on the basis of chemistry. This results differ from the conclusions of the combined studies (Chap. 3.4), because some factors affecting the fragmentation level depth are not included in the model. Effects that cannot be included in the model calculation are 1) the admixing of andesitic magma in the conduit during the last phase of the eruption, because the model cannot handle two different components, 2) the conduit widening during the last phase of the eruption, because the flow is pressure driven and therefore conduit width is fixed and 3) the highly variable conditions during the opening phase of the eruption, leading to the fluctuation of the fragmentation level (Chap. 3.4).

5.2.3. Laacher See eruption

The calculations show a clear dependence of the fragmentation level depth on the initial water content (see the velocity profiles in Appendix B-2-1). The fragmentation level moved from ~420 to 440 m in the models during the LLST phase. At the beginning of MLST B fragmentation level depth was at ~420 m in the model and moved successively downward to ~555m during VII and ~580 m during MLST-C3. This shows that the conduit dynamics and fragmentation level depth significantly changed with the changing pre-eruptive water content and chemical composition of the magma erupted.

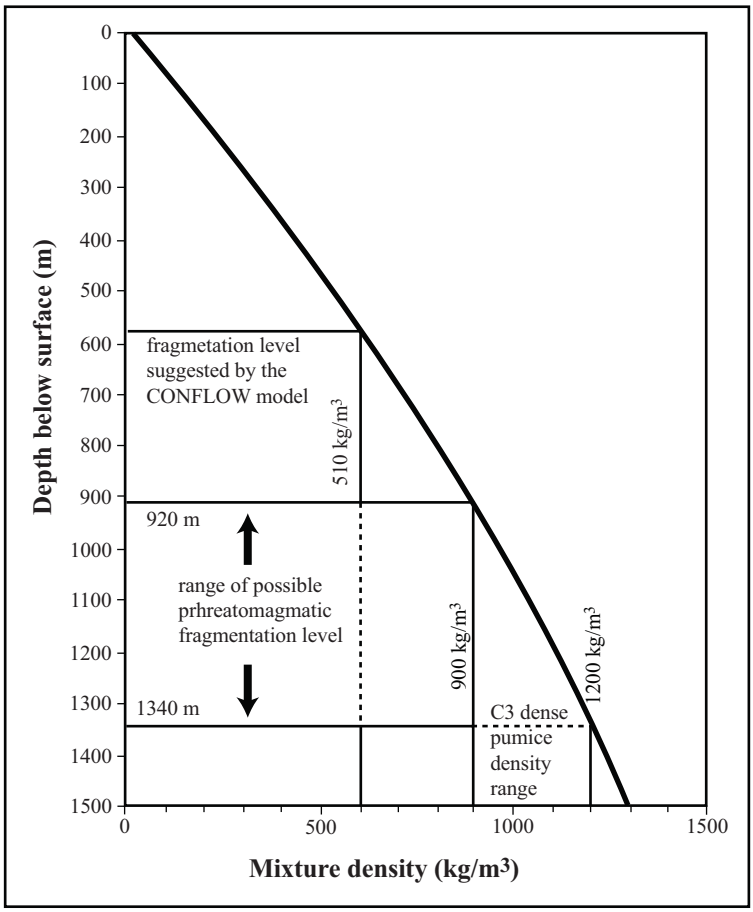

Fig. 5.1: Fragmentation level depth of MLST-C3 as deduced from the mixture density in the conduit calculation by the conflow model. Density variation of C3 gray pumice clasts represent the point of water-magma interaction and fragmentation.

The fragmentation depth suggested for the MLST-C3 by the model calculations is not reliable, because this bed is interpreted to be the result of an increasing water-magma interaction in the conduit. The impact of water during this phase is concluded from the

abundant dense gray pumice clasts in this bed (900-1200 kg/m^3, or ~50-60 vol% vesicles). Their vesicularity range is well below the 75 vol% fragmentation criterion (~510 kg/m^3). The lower vesicularity of the dense gray pumice clasts is a result of the magma-water interaction, forcing fragmentation immediately followed by quenching. Therefore the model calculations were applied to determine the depth of water-magma interaction in the conduit by comparing the calculated mixture densities, representing the modeled pumice density prior fragmentation, with the determined density range of dense gray pumice (Fig. 5.1). The depth range corresponding to this mixture density range in the calculations is assumed to represent the depth of water-magma interaction. Therefore the C3 mixture density points towards a deeper, "phreatomagmatic" fragmentation level during the C3 phase at ~920-1340 m, being much deeper than the assumed "magmatic" fragmentation level depth ~580 m indicated by CONFLOW model calculations.

5.3. Is pumice clast shape only controlled by shear intensity?

The shape parameters (formfactor, solidity and elongation) determined for 2-1 mm pumice clasts of both eruptions were compared to both the median pumice size and the median mass of clasts of the corresponding bed/stage. The median clast mass was calculated based on the median of the pumice GSD. The median pumice size was used for the calculation of the volume of an equivalent sphere. This volume was multiplied with the pumice or respectively average deposit density to determine the median mass of the clasts. The shape parameter vs. median and vs. median mass plot display linear trends for both eruptions (Figs. 5.2 and 5.3). The correlation is best for solidity and formfactor vs. median pumice size and mass. The most

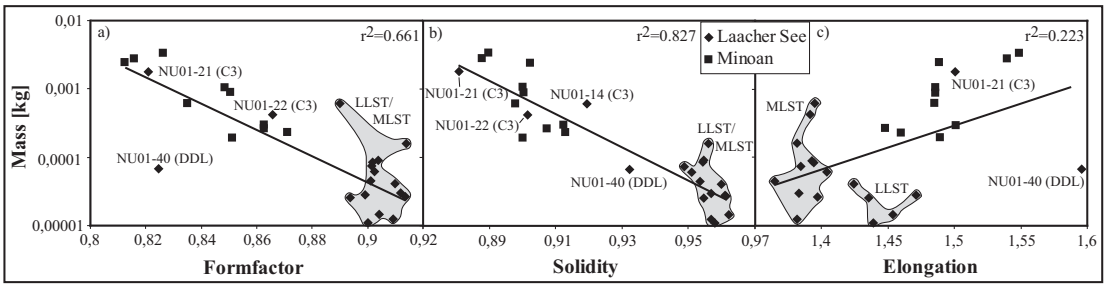

Fig. 5.2: Median mass vs. shape parameters formfactor, solidity and elongation. The LST samples with shape parameters comparable to the Minoan shape parameter are labeled with their sample numbers and the corresponding bed in brackets. The gray fields describe the range of LST shape parameters. For all plots power regressions (black line) and correlation coefficients (r^2) for all samples are displayed.

striking finding is that the two eruptions explored, being very different in many aspects (see e.g. Tab. 5.1), still plot on the same line. This points towards some general mechanism operating during Plinian eruptions regardless of the shear intensity. This is basically concluded from the formfactor and solidity values of the LLST beds which represent a phase of high shear intensity. If shear intensity is the only factor controlling the shape parameters of 2-1 mm clasts, then low values of formfactor and solidity, comparable to the values of Minoan eruption phase1, would be expected for the pumice clasts of this beds. This is not observed in the shape parameter values of the LLST beds and they plot together with the other LST shape parameters at high values of formfactor and solidity. A few beds of the LST (LLSTf, C3-beds) differ significantly from the average LST shape parameter range and consequently overlap with the shape parameter range of the Minoan fall deposit. All these LST beds have a common feature: they are all rich in dense clasts (either lithoclasts or dense

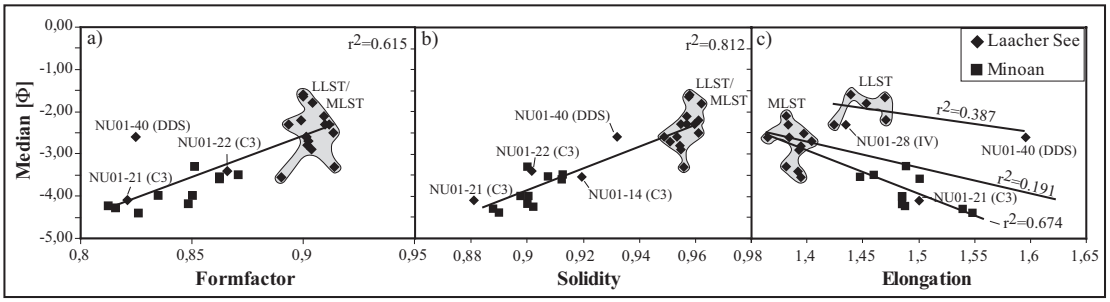

Fig. 5.3: Median grain size vs. shape parameters formfactor, solidity and elongation. The LST samples with shape parameters comparable to the Minoan shape parameter are labeled with their sample numbers and the corresponding bed in brackets. The gray fields describe the range of LST shape parameters. For a) and b) the linear regression (black line) and correlation coefficients of all samples are displayed. For c) the regression and correlation coefficients of all samples (0.191), Minoan and MLST samples (0.674) and LLST samples (0.387) are displayed.

pumice clasts exceeding about 50 wt%).

The counterintuitive position of the LST explained above indicates that possibly other processes are responsible for the fine lapilli clast shapes generated during Plinian eruptions. The examination of the characteristics of the LST beds with deviant shape parameter values can reveal information about possible processes altering the clast shapes. The interpretation of the conduit flow models of the C3 beds, especially the assumed “phreatomagmatic” fragmentation level, suggests that it was possibly twice as deep in the conduit during this phase compared to the other phases of the LSE. This may indicate that the fragmentation level depth and the resulting longer pathway for the fragmented magma influences the shape parameters of the clasts by extending the time range available for particle-particle interaction in the ascending and confined gas-particle mixture. Further the C3 beds are characterized by

median clast sizes of the same range as the Minoan fall deposit median clast sizes. Thus the median of the erupted clast population can be interpreted as a feature controlling the clasts shape parameters. What effect the increasing water-magma interaction during the C3 phase exerted on the shape parameters can not be concluded from the available data.

The elongation shows a slightly different median and median mass dependence (Figs. 5.2c and 5.3c). The LLST clast shapes deviate significantly from the major trend defined by the MIN-A and MLST clasts and no mass/median to elongation relation can be derived. The LLST represents a phase of elevated shear intensity and high abundance of tube-pumice. Thus the elongation of the clasts is affected by the pumice textures rather than the dynamic processes in the conduit.

In summary the following dynamic features of an eruption seem to influence the shape parameters towards more elongated, rough and less spherical clast populations observed in the deposit (Fig. 5.4):

- Shear intensity in the conduit.
- Tube-pumice abundance.
- Fragmentation level depth and the corresponding pathway for the fragmented mixture.
- Median clast size increase.
- Amount of dense clasts in the erupted mixture.

The mechanical processes controlling the shape parameters during the ascent of the magma and gas-magma mixture in the confining conduit are not directly observable and therefore only assumptions can be made here. It seems that abrasion, resulting in clast rounding during conduit transport after fragmentation, is not necessarily the major active process in confined, turbulent gas-particle mixtures as it is in other environments where clasts are transported (e.g. in rivers). This is mainly the result of the different transport processes, mixture density, velocity of the mixture, time scales and fragility of the involved particles. In e.g. rivers the commonly dense clasts are diluted in a rather slowly flowing transporting media, resulting in a long time of successive grinding, abrasion and rounding of the clasts. In a conduit the fragile, juvenile clasts are rapidly transported in a turbulent particle loaded gas jet, resulting in a short time of high-speed particle-particle collisions. It is known from planetary evolution

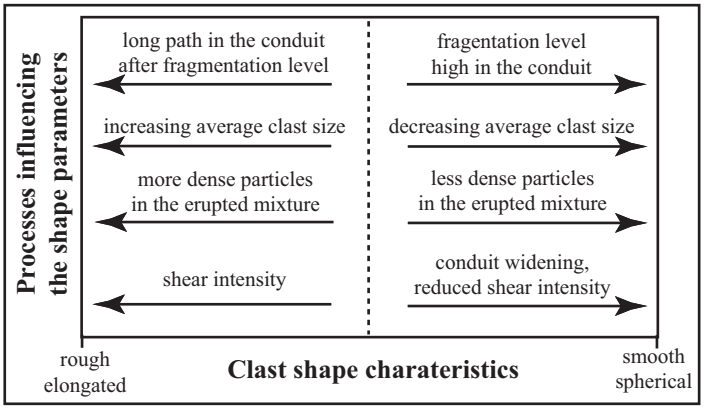

Fig.5.4: Processes intended to exert effect on clast shpes and clast surface appearence. On the left side the prosesses are listed that result in more elongated, angular and rough clast shapes, on the right processes that result in more shperical, rounded and smooth clast shapes.

that the collision of small bodies causes a destruction (breakup) of the involved particles as the mean encounter velocity rises (Melosh, 1989). So it is assumed that the particle-particle collisions in the high-velocity and turbulent mixture result in a breakup of the fragile pumice clasts, generating angular and irregular clasts, and a generation of convex impact marks on the clast surfaces, resulting in rough and non-spherical clast appearance (low formfactor and solidity values). The intensity of this roughening process and the formation of non-spherical clast shapes is controlled by the time available for particle interaction, clast density range and clast size range or median clast size. Further the pumice textures seem to play a significant role concerning the elongation of the resulting clasts during impact induced clast fragmentation. So the increased elongation of clasts of the LLST beds (Figs. 5.1c and 5.2c) indicate that the abundant tube-pumice clasts form elongated shards on breakup, resulting in a higher average elongation of the clast population in these beds. The other shape parameters seem to be almost unaffected by the tube-pumice abundance.

5.4. Concluding remarks and outlook

In conclusion the comparison of the two Plinian eruption phases indicates, that the chemically homogeneous Minoan eruption offers much more opportunities for interpretation of the changes in eruption dynamic and the dynamic controlling factors than the Laacher See eruption. The reasons for this are mainly the chemical and resulting viscosity variation, the abundant influence external water and the complexity of the deposit and pumice population. This distinction is better achieved for the Minoan Plinian eruption, because of the homogenous chemical composition of the major rhyodacitic melt. Therefore it is better to apply this kind of combined studies first to simple, chemically homogeneous eruptions to

learn which parameters are most useful to decipher temporal conduit and eruption dynamic changes from Plinian fall deposits. With complex Plinian eruptions that are influenced by numerous internal (e.g. chemical zonation) and external factors (e.g. external water access of varying degree) the variety of possible interpretations impede conclusions on dynamic changes. These eruptions are suitable for later studies of this kind, when the method has developed and a distinction between these multiple factors is possible.

Based on model calculations it can be assumed that the fragmentation level was about 200-360 m deeper during the Minoan Plinan eruption than during the Laacher See Plinian phases. This is mainly an effect of the higher pre-eruptive water content of the Minoan eruption. The MLST-C3 phase was controlled by an increasing degree of water-magma interaction (therefore interpreted as phreatoplinian), resulting in a lower fragmentation level than the other LSE Plinian phases and the Minoan Plinian eruption.

A possible effect of the deeper fragmentation level are the differences in the shape parameters that indicate on average rougher and less rounded clasts in the Minoan fall deposit than in LST. This effect may be caused by the different distances available for particle-particle interaction (shallow vs. deep fragmentation level). When this distance covered is longer the clasts seem to show an increased amount of convex impact marks rather than getting more well rounded. This effect further seems to take place when the erupted mixture contains a significant amount of dense clasts (either lithoclast or dense pumice exceeding about 50 wt%). This indicates that the shape parameter not only depend on the shear intensity in the conduit but also on the general conduit dynamics and average mass of the erupted clast population. These dependencies are only a first insights in a possible connection of eruption dynamics and shape parameter. Thus it is a first approach and the statistical data base is still too small to draw final and clear conclusions. Further studies concerning this relation have to be carried out to extend eruption dynamic, clast texture and clast shape parameter datasets to other Plinian eruptions and also phreatomagmatic eruptions.

References

Alibidirov, M. and Dingwell, D.B., 1996. Magma fragmentation by rapid decompression. Nature, 380: 146-149.

Alidibirov, M. and Panov, V., 1998. Magma fragmentation dynamics: experiments with analogue porous low-strenght material. Bull Volcanol, 59: 481-489.

Alidibirov, M.A., 1994. A model for viscous magma fragmentation during volcanic blasts. Bull Volcanol, 56: 459-465.

Bagdassarov, N. and Dingwell, D.B., 1992. A rheology investigation of vesicular rhyolite. J Volcanol Geotherm Res, 50: 307-322.

Bagdassarov, N. and Dingwell, D.B., 1993. Frequency dependent rheology of vesicular rhyolite. J Geophys Res, 98: 6,477-6,487.

Baille, M.G.L. and Munroe, M.A.R., 1988. Irish tree-rings, Santorin and volcanic dust veils. Nature, 332: 344-346.

Barclay, J., Riley, D.S. and Sparks, R.S.J., 1995. Analytical models for bubble growth during decompression of high viscosity magmas. Bull Volcanol, 57: 422-432.

Berndt, J., Holtz, F. and Koepke, J., 2001. Experimental constraints on storage conditions in the chemically zoned phonolitic magma chamber of the Laacher See volcano. Contr Min Petrol, 140: 469-486.

Blower, J.D., Keating, J.P., Mader, H.M. and Phillips, J.C., 2001. Inferring volcanic degassing processes from vesicle size distributions. Geophys Res Lett, 28: 347-350.

Blower, J.D., Keating, J.P., Mader, H.M. and Phillips, J.C., 2002. The evolution of bubble size distributions in volcanic eruptions. J Volcanol Geotherm Res, 120: 1-23.

Bogaard, P.v., 1983. Die Eruption des Laacher See Vulkans. PhD Thesis, Ruhr-Universität, Bochum, 348 pp.

Bogaard, P.v., 1995. $^{40}Ar/^{39}Ar$ ages of sanidine phenocrysts from Laacher See Tephra (12,900 yr BP): Chronostratigraphic and petrological significance. Earth Plan Sci Lett, 133: 163-174.

Bogaard, P.v., Schmincke, H.-U., Freundt, A. and Park, C., 1990. Evolution of a complex Plinian eruption: The late Quaternary Laacher See case history. In: D.A. Hardy (Editor), Thera and the Aegean world III. The Thera Foundation, London, pp. 463-483.

Bogaard, P.v.d. and Schmincke, H.-U., 1984. The eruptive center of the Late Quaternery Laacher See Tephra. Geol Rundsch, 73: 933-980.

Bogaard, P.v.d. and Schmincke, H.-U., 1985. Laacher See Tephra: A widespread isochronous late Quaternary tephra layer in central and northern Europe. Geol Soc Am Bull, 96: 1,554-1,571.

Bond, A. and Sparks, R.S.J., 1976. The Minoan eruption of Santorini, Greece. J Geol Soc London, 132: 1-16.

Bottinga, Y. and Javoy, M., 1990. MORB degassing: bubble growth and ascent. Chem Geol, 81: 255-270.

Buresti, G. and Casarosa, C., 1989. One-dimensional adiabatic flow of equilibrium gas-particle mixtures in long vertical ducts with friction. Journal of Fluid Mechanics, 203: 251-272.

Carey, S. and Bursik, M., 2000. Volcanic Plumes. In: H. Sigurdsson, B. Houghton, S. McNutt, H. Rymer and J. Stix (Editors), Encyclopedia of volcanoes. Academic Press, San Diego, pp. 527-544.

Carey, S.N. and Sigrudsson, H., 1989. The intensity of plinian eruptions. Bull Volcanol, 51: 28-40.

Carey, S.N. and Sparks, R.S.J., 1986. Quantitative models of the fallout and dispersal of tephra from volcanic eruption columns. Bull Volcanol, 48: 109-125.

Cioni, R., Marianelli, P., Santacroce, R. and Sbrana, A., 2000. Plinian and subplinian eruptions. In: H. Sigurdsson, B. Houghton, S. McNutt, H. Rymer and J. Stix (Editors), Encyclopedia of volcanoes. Academic Press, San Diego, pp. 477-494.

Cottrell, E., Gardner, J.E. and Rutherford, M.J., 1999. Petrologic and experimental evidence for the movement and heating of the pre-eruptive Minoan rhyodacite (Santorini, Greece). Contr Min Petrol, 135: 315-331.

Dellino, P., Isaia, R., La Volpe, L. and Orsi, G., 2001. Statistical analysis of textural data from complex pyroclastic sequences: implications for fragmentation processes of the Agnano-Monte Spina Tephra (4.1 ka), Phlegraean Fields, southern Italy. Bull Volcanol, 63: 443-461.

Devine, J.D., Gardner, J.E., Brack, H.P., Layne, G.L. and Rutherford, M.J., 1995. Comparison of microanalytical methods for estimating H_2O contents of silicic volcanic glasses. Am Min, 80: 319-328.

Dingwell, D.B., 1997. The brittle-ductile transition in high-level granitic magmas: Material constraints. J Petrol, 38: 1,635-1,644.

Dingwell, D.B., 1998a. Magma degassing and fragmentation: recent experimental advances. In: A. Freundt and M. Rosi (Editors), From magma to tephra - modelling physical processes of explosive volcanic eruptions. Elsevier, Amsterdam, pp. 1-23.

Dingwell, D.B., 1998b. Recent experimental progress in the physical description of silicic magma relevant to explosive volcanism. In: J.S. Gilbert and R.S.J. Sparks (Editors), The physics of explosive volcanic eruptions. Special Publications. Geological Society, London, pp. 9-26.

Dobran, F., 1992. Nonequilibrium flow in volcanic conduits and application to the eruptions of Mt. St. Helens on May 18, 1980 and Vesuvius AD 79. J Volcanol Geotherm Res, 49: 285-311.

Druitt, T.H., Edwards, L., Mellors, R.M., Pyle, D.M., Sparks, R.J.S., Lanphere, M., Davies, M., Barriero, B., 1999. Santorini Volcano. Geol Soc London Mem, 19: 1-165.

Druitt, T.H. and Francaviglia, V., 1992. Cladera formation on Santorini and the physiography of the island in the late Bronze Age. Bull Volcanol, 54: 484-493.

Druitt, T.H., Mellors, R.A., Pyle, D.M. and Sparks, R.S.J., 1989. Explosive volcanism on Santorini, Greece. Geol Mag, 126: 95-126.

Dunbar, N.W. and Kyle, P.R., 1993. Lack of volatile gradient in the Taupo Plinian-ignimbrite transtition: evidence from melt inclusion analysis. Am Min, 178: 612-618.

Freundt, A. and Schmincke, H.-U., 1985. Lithic-enriched segregation bodies in pyroclastic flow deposits of Laacher See volcano (E-Eifel, Germany). J Volcanol Geotherm Res, 25: 193-224.

Freundt, A. and Schmincke, H.-U., 1986. Emplacement of small-volume pyroclastic flows at Laacher See (East-Eifel, Germany). Bull Volcanol, 48: 39-59.

Freundt, A. and Tait, S.R., 1986. The entrainment of high-viscosity magma into an low-viscosity magma in eruption conduits. Bull Volcanol, 48: 325-339.

Friedrich, W.L., Wagner, P. and Tauber, H., 1990. Radiocarbon dated plant remains from the Akrotiri excavation on Santorini, Greece. In: D.A. Hardy (Editor), Thera and the Aegean World III. The Thera Foundation, London, pp. 188-196.

Gaonac'h, H., Lovejoy, S., Stix, J. and Schertzer, D., 1996. A scaling growth model for bubbles in basaltic lava flows. Earth Plan Sci Lett, 139: 395-409.

Gardner, C.A., Cashman, K.V. and Neal, C.A., 1998. Tephra-fall deposits from the 1992 eruption of Crater Peak, Alaska: implications of clast textures for eruptive processes. Bull Volcanol, 59: 537-555.

Gardner, J.E., Hilton, M. and Carroll, M.R., 1999. Experimental constraints on degassing of magma: isothermal bubble growth during continuous decompression from high pressure. Earth Plan Sci Lett, 168: 201-218.

Gardner, J.E., Thomas, R.M.E., Jaupart, C. and Tait, S.R., 1996. Fragmentation of magma during plinian volcanic eruptions. Bull Volcanol, 48: 144-162.

Hajdas, I. et al., 1995. AMS radiocarbon dating of annually laminated sediments from Holzmaar, Germany. Quat Sci Rev, 14: 137-143.

Hammer, C.U., Clausen, H.B., Friedrich, W.L. and Tauber, H., 1987. The Minoan eruption of Santorini in Greece dated to 1645 BC? Nature, 328: 517-519.

Harms, E., 1998. Volatile composition and syn-eruptive degassing of the Laacher See phonolite magma (12,900 yr BP). PhD Thesis, Christian-Albrechts-Universität, Kiel, 150 pp.

Harms, E., Gardner, J.E. and Schmincke, H.-U., 2003. Phase equilibra of the Lower Laacher See Tephra (LLST, East Eifel, Germany): Constraints on pre-eruptive storage conditions of a phonolitic magma resrevoir. J Volcanol Geotherm Res, submitted.

Harms, E. and Schmincke, H.-U., 2000. Volatile composition of the phonolitic Laacher See magma (12,900 yr BP): implications for syn-eruptive degassing of S, F, Cl and H_2O. Contr Min Petrol, 138: 84-98.

Heiken, G., 1987. Textural analysis of tephra from a rhyodacitic eruption sequence, Thira (Santorini), Greece. In: J.R. Marshall (Editor), Clastic particles. Van Nostrand, New York, pp. 67-78.

Heiken, G. and McCoy, F., 1984. Caldera development during the Minoan eruption, Thira, Cyclades, Greece. J Geophys Res, 89: 8,441-8,462.

Hess, K.U. and Dingwell, D.B., 1996. Viscosities of hydrous leucogranitic melts: a non-Arrhenian model. Am Min, 81: 1,297-1,300.

Hort, M. and Gardner, J.E., 1999. Constraints on cooling and degassing of pumice during plinian volcanic eruptions based on model calculations. J Geophys Res, 105: 25,981-26,001.

Houghton, B., Wilson, C.J.N. and Pyle, D.M., 2000a. Pyroclastic fall deposits. In: H. Sigurdsson, B. Houghton, S. McNutt, H. Rymer and J. Stix (Editors), Encyclopedia of volcanoes. Academic Press, San Diego, pp. 555-570.

Houghton, B., Wilson, C.J.N., Smith, R.T. and Gilbert, J.S., 2000b. Phreatoplinian eruptions. In: H. Sigurdsson, B. Houghton, S. McNutt, H. Rymer and J. Stix (Editors), Encyclopedia of volcanoes. Academic Press, San Diego, pp. 513-527.

Hurwitz, S. and Navon, O., 1994. Bubble nucleation in rhyolitic melts: Experiments at high pressure, temperature, and water content. Earth Plan Sci Lett, 122: 267-280.

Innocenti, F., Manetti, P., Peccerillo, A. and Poli, G., 1981. South Aegean volcanic arc: geochemical variations and geotectonicimplications. Bull Volcanol, 44: 377-391.

Jackson, J.A., 1994. Active tectonics of the Aegean region. Ann Rev Earth Planet Sci, 22: 239-271.

Jaupart, C., 2000. Magma ascent at shallow levels. In: H. Sigurdsson, B. Houghton, S. McNutt, H. Rymer and J. Stix (Editors), Encyclopedia of volcanoes. Academic Press, San Diego, pp. 237-245.

Jurado-Chichay, Z. and Walker, G.P.L., 2001. Variability of plinian fall deposits: examples from Okataina Volcanic Centre, New Zealand. J Volcanol Geotherm Res, 111: 239-263.

Kaminski, E. and Jaupart, C., 1997. Expansion and quenching of vesicular magma fragments in Plinian eruptions. J Geophys Res, 102: 12187-12203.

Kaminski, E. and Jaupart, C., 1998. The size distribution of pyroclasts and the fragmentation sequence in explosive volcanic eruptions. J Geophys Res, 103: 29759-29779.

Klug, C. and Cashman, K.V., 1996. Permeability development in vesiculating magmas: implications for fragmentation. Bull Volcanol, 58: 87-100.

Klug, C., Cashman, K.V. and Bacon, C.R., 2002. Structure and physical characteristics of pumice from the climatic eruption of Mount Mazama (Crater Lake); Oregon. Bull Volcanol, 64: 486-501.

Knoop, U., 1981. Lithologie und Entstehung der Unteren Laacher See Pyroklastika im Mendiger Raum, Diploma Thesis, Ruhr-Universität, Bochum, 180 pp.

LaMarche, V.C. and Hirschboeck, K.K., 1984. Frost rings in trees as records for major volcanic eruptions. Nature, 307: 121-126.

Lange, R.A., 1994. The effect of H2O, CO2 and F onm the density and viscosity of silicate melts. Rev Min, 30: 331-365.

Llewellin, E.W., Mader, H.M. and Wilson, D.R., 2002. The rheology of a bubbly liquid. Proc Roy Soc London A, 458: 978-1016.

Lyakhowsky, V., Hurwitz, S. and Navon, O., 1996. Bubble growth in rhyolitic melts: experimental and numerical investigation. Bull Volcanol, 58: 19-32.

Mader, H.M., 1998. Conduit flow and fragmentation. In: J.S. Gilbert and R.S.J. Sparks (Editors), The physics of explosive volcanic eruptions. Special Publications. Geological Society, London, pp. 51-71.

Mader, H.M. et al., 1994. Experimental simulations of explosive degassing of magma. Nature, 372: 85-88.

Manga, M., Castro, J., Cashman, K.V. and Loewenberg, M., 1998. Rheology of bubble-bearing magmas. J Volcanol Geotherm Res, 87: 15-28.

Manga, M. and Loewenberg, M., 2001. Viscosity of magmas containing highly deformable bubbles. J Volcanol Geotherm Res, 105: 19-24.

Mangan, M.T. and Sisson, T., 2000. Delayed, disequilibrium degassing in rhyolite magma: decompression experiments and implications for explosive volcanism. Earth Plan Sci Lett, 183: 441-455.

Martel, C., Dingwell, D.B., Spieler, O., Pichavant, M. and Wilke, M., 2000. Fragmentation of foamed silicic melts: an experimental study. Earth Plan Sci Lett, 178: 47-58.

Martel, C., Dingwell, D.B., Spieler, O., Pichavant, M. and Wilke, M., 2001. Experimental fragmentation of crystal- and vesicle-bearing silicic melts. Bull Volcanol, 63: 398-405.

Mastin, L.G. and Ghiorso, M.S., 2000. Conflow. U.S. Geological Survey, Vancouver.

Mastrolorenzo, G., Brachi, L. and Canzanella, A., 2001. Vesicularity of various types of pyroclastic deposits of Campi Flegrei volcanic field: evidence of analogies in magma rise and vesicultaion mechanisms. J Volcanol Geotherm Res, 109: 41-53.

Melnik, O., 2000. Dynamics of two-phase conduit flow of high-viscosity gas-saturated magma: large variations of sustained explosive eruption intensity. Bull Volcanol, 62: 153-170.

Melnik, O.E., 1999. Fragmenting magma. Nature, 397: 394-395.

Melosh, H.J., 1989. Impact cratering - A geologic process. Oxford University Press, 245 pp.

Michaud, V., Clocchiatti, R. and Sbrana, S., 2000. The Minoan and post-Minoan eruptions, Santorini (Greece), in the light of melt inclusions: chlorine and sulphur behaviour. J Volcanol Geotherm Res, 99: 195-214.

Mungall, J.E., Bagdassarov, N., Romano, C. and Dingwell, D.B., 1996. Numerical modelling of stress generation and microfracturing of vesicle walls in glassy rocks. J Volcanol Geotherm Res, 73: 33-46.

Neri, A., Papale, P. and Macedonio, G., 1998. The role of magma composition and water content in explosive eruptions. 2. Pyroclastic dispersion dynamics. J Volcanol Geotherm Res, 87: 95-115.

Papale, P., 1998. Volcanic conduit dynamics. In: A. Freundt and M. Rosi (Editors), From magma to tephra - modelling physical processes of explosive volcanic eruptions. Elsevier, Amsterdam, pp. 55-89.

Papale, P., 1999. Strain-induced magma fragmentation in explosive eruptions. Nature, 397: 425-428.

Papale, P. and Dobran, F., 1994. Magma flow along the volcanic conduit during the Plinian and pyroclastic flow phases of the May 18, 1980 Mount St. Helens eruption. J Geophys Res, 99: 4,355-4,373.

Papale, P., Neri, A. and Macedonio, G., 1998. The role of magma composition and water content in explosive eruptions. 1. Conduit ascent dynamics. J Volcanol Geotherm Res, 87: 75-93.

Papale, P. and Polacci, M., 1999. Role of carbon dioxide in the dynamics of magma ascent in explosive eruptions. Bull Volcanol, 60: 583-594.

Papazachos, B.C. and Panagiotopoulos, D.G., 1993. Normal faults associated with volcanic activity and deep rupture zones in the southern Aegean volcanic arc. Tectonophysics, 220: 301-308.

Polacci, M., Papale, P. and Rosi, M., 2001. Textural heterogeneities in pumices from the climatic eruption of Mount Pinatubo, 15 June 1991, and implications for magma acsent dynamics. Bull Volcanol, 63: 83-97.

Proussevitch, A., Sahagian, D.L. and Anderson , A.T., 1994. Dynamics of diffusive bubble growth in magmas: Isothermal case. J Geophys Res, 98: 22,283-22,307.

Proussevitch, A.A. and Sahagian, D., 1996. Dynamics of coupled diffusive and decompressive bubble growth in magmatic systems. J Geophys Res, 101: 17,447-17,455.

Pyle, D.M., 1990. New estimates for the volume of the Minoan eruption. In: D.A. Hardy (Editor), Thera and the Aegean world III. The Thera Foundation, London, pp. 113-121.

Ramos, J.I., 1995. One-dimensional, time-dependent, homogeneous, two-phase flow in volcanic conduits. Int J Numer Methods Fluids, 21: 253-278.

Risse, R., 1976. Stratigraphie, Transport- und Ablagerungsmechanismen der Mittleren Laacher See Pyroklastika im Laacher See Gebiet(Osteifel), Diploma Thesis, Ruhr-Universität, Bochum, 204 pp.

Roscoe, R., 1952. The viscosity of suspensions of rigid spheres. J App Phys, 2: 267-269.

Rosenbleck, C., 1990. Die Entstehung der phonolitischen MLSTC-Lage der Laacher See Tephra. Diploma Thesis, Ruhr-Universität, Bochum, 134 pp.

Rosi, M., 1998. Plinian eruption columns: particle transport and fallout. In: A. Freundt and M. Rosi (Editors), From magma to tephra - modelling physical processes of explosive volcanic eruptions. Elsevier, Amsterdam, pp. 139-172.

Russell and Taylor (1937)

Schmincke, H.-U., 1970. "Base surge"-Ablagerungen des Laacher See-Vulkans. Der Aufschluss, 21: 350-364.

Schmincke, H.-U., 1977. Phreatomagmatische Phasen in quartären Vulkanen der Osteifel. Geol Jb, A39: 3-45.

Schmincke, H.-U., 1981. Bimsablagerungen des Laacher See Vulkans. In: A. Neunast and J. Theiner (Editors), "Bims". Müller Verlag, Köln, pp. 19-31.

Schmincke, H.-U., 2000. Vulkanismus. Wiss Buchgesellschaft Darmstadt, 264 pp.

Schmincke, H.-U., Bogaard, P.v. and Freundt, A., 1990. Quaternary Eifel Volcanism. Excursion guide. IAVCEI 1990 workshop on explosive volcanism. Pluto Press, Witten, 188 pp.

Schmincke, H.-U., Fisher, R.V. and Waters, A.C., 1973. Antidune and chute and pool structures in base surges of the Laacher See volcano (Germany). Sedimentology, 20: 1-24.

Schmincke, H.-U., Park, C. and Harms, E., 1999. Evolution and environmental impacts of the eruption of Laacher See Volcano (Germany) 12,900 a BP. Quat Int, 61: 61-72.

Schumacher, R. and Schmincke, H.-U., 1990. The lateral facies of ignimbrites at Laacher See volcano. Bull Volcanol, 52: 271-285.

Shaw, H.R., 1972. Viscosities of magmatic silicate liquids: an empirical method of prediction. Am J Sci, 272: 870-893.

Sigurdsson, H., Carey, S. and Devine, J.D., 1990. Assessment of mass, dynamics and environmental effects of the Minoan eruption of Santorini volcano. In: D.A. Hardy (Editor), Thera and the Aegean world III. The Thera Foundationn, London, pp. 100-112.

Slezin, Y.B., 2003. The mechanism of volcanic eruptions (a steady state approach). J Volcanol Geotherm Res, 122: 7-50.

Sparks, R.S.J., 1978. The dynamics of bubble deformation and growth in magmas: A review and analysis. J Volcanol Geotherm Res, 3: 137-186.

Sparks, R.S.J., Barclay, J., Jaupart, C., Mader, H.M. and Phillips, J.C., 1994. Physical aspects of magma degassing. I. Experimental and theoretical constraints on vesiculation. Rev Min, 30: 413-445.

Sparks, R.S.J. and Brazier, S., 1982. New evidence for degassing processes during explosive eruptions. Nature, 295: 218-220.

Sparks, R.S.J., Bursik, M.I., Carey, S.N., Gilbert, J.S., Glaze, L.S., Sigurdsson, H., Woods, A.W., 1997. Volcanic plumes. Wiley&Sons, New York, 574 pp.

Staps, P., 1976. Stratigraphie, Verbreitung, Aufbau und Entstehung der Unteren Laacher See Pyroklastika. Diploma Thesis, Ruhr-Universität, Bochum, 112 pp.

Taddeucci, J. and Wohletz, K.H., 2001. Temporal evolution of the Minoan eruption (Santorini, Greece), as recorded by its Plinian fall deposit and interlayered ash flow beds. J Volcanol Geotherm Res, 109: 299-317.

Tait, S., Thomas, R.M.E., J.E., G. and Jaupart, C., 1998. Constraints on cooling rates and permeabilities of pumice in an explosive jet from colour and magnetic mineralogy. J Volcanol Geotherm Res, 86: 79-91.

Tait, S.R., 1988. Samples from the crystallising boundary layer of a zoned magma chamber. Contr Min Petrol, 100: 470-483.

Tait, S.R., Wörner, G., Bogaard, P.v. and Schmincke, H.-U., 1989. Cumulative nodules as evidence for convective fractionation in a phonolite magma chamber. J Volcanol Geotherm Res, 37: 21-37.

Thomas, N., Jaupart, C. and Vergniolle, S., 1994. On the vesicularity of pumice. J Geophys Res, 99: 15,663-156,64.

Toramaru, A., 1995. Numerical study of nucleation anf growth of bubbles in viscous magmas. J Geophys Res, 100: 1,913-1,931.

Turcotte, D.L., Ockendon, H., Ockendon, J.R. and Cowley, S.J., 1990. A mathematical model of vulcanian eruptions. Geophys J Int, 103: 211-217.

Varekamp, J.C., 1992. Some remarks on volcanic vent evolution during plinian eruptions. J Volcanol Geotherm Res, 54: 309-318.

Vergniolle, S. and Jaupart, C., 1986. Separated two-phase flow and basaltic eruptions. J Geophys Res, 91: 12,842-12,860.

Whitham, A.G. and Sparks, R.S.J., 1986. Pumice. Bull Volcanol, 48: 209-223.

Wilson, C.J.N. and Houghton, B.F., 1990. Eruptive mechanisms in the Minoan eruption: Evidence from pumice vesicularity. In: D.A. Hardy (Editor), Thera and the Aegean world III. The Thera Foundation, London, pp. 122-128.

Wilson, L., 1980. Relationship between pressure, volatile content and ejecta velocity in three types of volcanic explosions. J Volcanol Geotherm Res, 8: 297-313.

Wilson, L., Sparks, R.S.J. and Walker, G.P.L., 1980. Explosive volcanic eruptions IV: The control of magma properties and conduit geometry on eruption column behaviour. Geophys J Roy Astr Soc, 63: 117-148.

Wilson, L. and Walker, G.P.L., 1987. Exlposive volcanic eruptions VI. Ejecta dispersal in plinian eruptions: the control of eruption conditions and atmospheric properties. Geophys J Roy Astr Soc, 89: 657-679.

Wörner, G., Beusen, J.-M., Duchateau, N., Gijbels, R. and Schmincke, H.-U., 1983. Trace element abundances and mineral/melt distribution coefficients in phonolites from the Laacher See Volcano (Germany). Contr Min Petrol, 84: 152-173.

Wörner, G. and Schmincke, H.-U., 1984a. Mineralogical and chemical zonation of the Laacher See Tephra sequence (East Eifel, Germany). J Petrol, 25: 805-835.

Wörner, G. and Schmincke, H.-U., 1984b. Petrogenesis of the zoned Laacher See Tephra. J Petrol, 25: 836-851.

Wörner, G., Staudigel, H. and Zindler, A., 1985. Isotopic constraints on open system evolution of the Laacher See magma chamber (Eifel, West Germany). Earth Plan Sci Lett, 75: 37-49.

Acknowledgements

First of all, I want to thank Matthias Hort who enabled me to carry out this study and supported my work all the time. I benefitted from the numerous discussions with him about he physics of volcanic eruptions and his reviews of earlier manuscripts of this study.
Further I want to thank Hans-Ulrich Schmincke for his wonderful introduction into the complex deposits of the Laacher See eruption in the field and the thorough reviews of the earlier manuscripts that improved the quality of this study.
Many thanks to the staff of the department, including the former staff members Ralf Seyfried, Malte Vöge, Valentin Troll and Lothar Schwarzkopf, and the members of the Graduierten Kolleg for the great time at GEOMAR.
Mario Thöner helped me to carry out the SEM imaging and kept the SEM running despite all technical problems. Dagmar Rau carried out the XRF analyses of my samples. The team of the Institute of Soil Science and Plant Nutrition at the CAU, Kiel supported my permeability measurements in their laboratories. Dieter Dettmar prepared the polished thin sections of my pumice samples.
Thanks to Armin Freundt for giving me his spreadsheet to calculate the melt viscosities of my samples.
Special thanks to Steve Sparks who introduced me into the geology of Santorini during a field trip and supplied my with helpful information about the Minoan eruption and deposit.

I gratefully acknowledge the Deutsche Forschungsgesellschaft for their financial support of this study ("Fragmentierung von Magma bei plinianischen Eruptionen"; HO 1411/11-1 and "Graduierten Kolleg; Dynamik globaler Kreisläufe im System Erde"; SCHM 250/49).

Apppendix A-1 Minoan eruption

Maximum clast size
Grain size distribution
Median and sorting coefficient
Modal composition
Density
Permeability
Shape parameter
Vesicle size distributions
Chemistry

A-1-1a: Maximum pumice clast size variation of all three sections analyzed.

Section locality	height	max pumice					average pumice	Stddev
Phira Quarry	50	11,50	9,00	12,50	12,00	13,00	11,60	1,56
Phira Quarry	100	23,00	13,00	12,00	9,00	8,00	13,00	5,96
Phira Quarry	150	10,00	11,00	13,50	14,00	12,00	12,10	1,67
Phira Quarry	200	20,00	33,00	18,00	19,50	15,00	21,10	6,93
Phira Quarry	250	20,00	17,00	16,00	16,50	16,00	17,10	1,67
Phira Quarry	300	17,00	18,50	19,00	15,00	25,00	18,90	3,75
Phira Quarry	350	28,00	25,00	30,00	20,00	21,00	24,80	4,32
Phira Quarry	400	23,50	16,00	17,00	21,00	14,00	18,30	3,87
Phira Quarry	450	38,00	26,00	19,00	15,00	16,00	22,80	9,52
Phira Quarry	500	23,00	18,00	23,00	18,00		20,50	2,89
Phira Quarry	PHREATOMAGMATIC BREAK							
Phira Quarry	555	8,00	9,50	11,00	9,00	9,50	9,40	1,08
Cape Athinios	40	12,50	9,00	7,50	6,50	7,00	8,50	2,42
Cape Athinios	80	11,50	10,00	12,00	15,00	12,00	12,10	1,82
Cape Athinios	120	13,00	11,50	14,00	9,50	10,00	11,60	1,92
Cape Athinios	160	12,50	12,00	9,00	10,00	11,00	10,90	1,43
Cape Athinios	200	13,50	9,50	9,00	8,50	8,00	9,70	2,20
Cape Athinios	240	14,00	13,00	9,50	13,00	10,50	12,00	1,90
Cape Athinios	280	15,50	13,50	11,50	11,50	11,00	12,60	1,88
Cape Athinios	320	18,50	19,00	20,00	17,00		18,63	1,25
Cape Athinios	360	14,00	15,00	14,00	14,50		14,38	0,48
Cape Athinios	400	13,00	12,00	13,00	11,50		12,38	0,75
Cape Athinios	PHREATOMAGMATIC BREAK							
Cape Athinios	420	10,00	10,00	8,50	8,00		9,13	1,03
Cape Therma	25	6,50	6,00	5,00	6,50	6,50	6,10	0,65
Cape Therma	50	7,00	6,50	9,00	8,00		7,63	1,11
Cape Therma	75	8,50	9,00	9,50			9,00	0,50
Cape Therma	100	8,50	8,00	10,00	11,00		9,38	1,38
Cape Therma	125	11,00	10,00	13,00			11,33	1,53
Cape Therma	150	6,50	7,00	6,50			6,67	0,29
Cape Therma	175	11,00	10,00	7,00	10,00		9,50	1,73
Cape Therma	200	9,00	12,00	16,50	14,00	11,00	12,50	2,87
Cape Therma	225	18,00	20,00	13,00			17,00	3,61
Cape Therma	250	19,00	17,00	14,00	11,50		15,38	3,30
Cape Therma	PHREATOMAGMATIC BREAK							
Cape Therma	270	10,00	8,00	9,00			9,00	1

A-1-1b: Maximum lithic size distribution of all three sections analyzed.

Sample location	height	max lithic					average lithic	Stddev
Phira Quarry	50	3,20	4,00	4,60			3,93	0,70
Phira Quarry	100	3,00					3,00	0,00
Phira Quarry	150	5,00	6,00	6,50	8,50	5,00	6,20	1,44
Phira Quarry	200	12,00	8,00	11,00			10,33	2,08
Phira Quarry	250	3,00	4,50	3,00			3,50	0,87
Phira Quarry	300	4,00	4,50	4,00			4,17	0,29
Phira Quarry	350	7,50	5,00	6,00	5,50	6,00	6,00	0,94
Phira Quarry	400	6,00	9,00	4,00	5,00		6,00	2,16
Phira Quarry	450	5,00	3,00	3,00	5,00		4,00	1,15
Phira Quarry	500	5,00	6,50	4,50	4,00	5,00	5,00	0,94
Phira Quarry	PHREATOMAGMATIC BREAK							
Phira Quarry	555	3,00	2,50				2,75	0,35
Cape Athinios	40	3,00	3,50	2,50			3,00	0,50
Cape Athinios	80	3,50	2,50				3,00	0,71
Cape Athinios	120	3,00	3,00				3,00	0,00
Cape Athinios	160	4,00	3,50	4,00			3,83	0,29
Cape Athinios	200	4,00	4,00	3,00			3,67	0,58
Cape Athinios	240	3,50	3,00				3,25	0,35
Cape Athinios	280	2,50	2,50	3,00			2,67	0,29
Cape Athinios	320	9,00					9,00	0,00
Cape Athinios	360	4,00	3,50	3,00			3,50	0,50
Cape Athinios	400	2,50					2,50	0,00
Cape Athinios	PHREATOMAGMATIC BREAK							
Cape Athinios	420	4,00					4,00	0,00
Cape Therma	25	2,20	2,10	2,30			2,20	0,10
Cape Therma	50	2,60	2,30	2,90			2,60	0,30
Cape Therma	75	3,50	2,80				3,15	0,49
Cape Therma	100			4,00			4,00	0,00
Cape Therma	125			2,60			2,60	0,00
Cape Therma	150		3,80				3,80	0,00
Cape Therma	175	4,20		3,10			3,65	0,78
Cape Therma	200	4,50					4,50	0,00
Cape Therma	225		6,80		4,40		5,60	1,70
Cape Therma	250	5,20	4,70				4,95	0,35
Cape Therma	PHREATOMAGMATIC BREAK							
Cape Therma	270	4,80	3,80				4,30	0,71

A-1-2: Grainsize distribution of the samples taken in Phira Quarry.

Sample Number	Φ –5	Φ –4	Φ –3	Φ –2	Φ –1	Φ 0	Φ 1	Φ 2	Φ 3	Φ 4	Φ 5
MIN-A/SE1a 0-50 cm	18,65	42,93	20,25	6,81	1,70	0,82	0,66	0,78	1,65	0,87	4,88
MIN-A/SE1b 50-100 cm	22,37	33,00	18,19	8,59	3,19	0,95	0,93	0,76	2,25	2,04	7,73
MIN-A/SE1c 100-150 cm	15,90	38,44	21,15	9,34	3,76	1,06	0,97	0,70	1,53	0,69	6,45
MIN-A/SE1d 150-200 cm	8,66	41,43	22,55	8,40	3,98	1,69	1,48	1,52	2,23	1,33	6,75
MIN-A/SE1e 200-250 cm	10,32	31,78	20,79	7,95	5,61	2,20	2,03	1,42	2,23	1,90	13,76
MIN-A/SE1f 250-300 cm	36,99	24,05	18,77	8,04	3,12	1,33	0,99	0,79	0,93	0,70	4,29
MIN-A/SE1g 300-350 cm	5,85	26,82	28,67	10,80	6,70	2,98	2,46	1,50	1,93	1,12	11,17
MIN-A/SE1h 350-400 cm	7,75	25,23	28,28	10,77	7,22	3,18	2,42	1,17	1,40	0,99	11,59
MIN-A/SE1i 400-450 cm	9,80	30,90	24,24	12,46	5,95	2,58	3,79	1,41	1,40	1,08	6,39
MIN-A/SE1j 450-500 cm	9,47	22,78	22,98	13,84	8,75	3,84	5,35	2,15	1,93	1,70	7,20

A-1-3a: Median and sorting coefficient of the complete GSD.

Sample Number	%16	Md	%84	Sorting coefficient
MIN-A/SE1a	-5,00	-4,30	-2,85	1,08
MIN-A/SE1b	-5,00	-4,20	-1,60	1,70
MIN-A/SE1c	-5,00	-4,15	-2,20	1,40
MIN-A/SE1d	-4,85	-4,00	-1,50	1,68
MIN-A/SE1e	-4,80	-3,70	2,60	3,70
MIN-A/SE1f	-5,00	-4,50	-2,60	1,20
MIN-A/SE1g	-4,60	-3,50	0,80	2,70
MIN-A/SE1h	-4,70	-3,40	0,30	2,50
MIN-A/SE1i	-4,80	-3,70	-0,90	1,95
MIN-A/SE1j	-4,70	-3,30	0,30	2,50

A-1-3b: Median and sorting coefficient of the pumice GSD.

Sample Number	Φ%16	Median Φ	Φ%84	Sorting coefficient
MIN-A/SE1a	-4,95	-4,3	-3,2	0,88
MIN-A/SE1b	-5,00	-4,40	-3,05	0,98
MIN-A/SE1c	-5,00	-4,25	-2,95	1,03
MIN-A/SE1d	-4,90	-4,20	-2,85	1,03
MIN-A/SE1e	-4,90	-4,00	-2,20	1,35
MIN-A/SE1f	-5,00	-4,00	-2,55	1,23
MIN-A/SE1g	-4,70	-3,60	-2,00	1,35
MIN-A/SE1h	-4,70	-3,50	-2,50	1,10
MIN-A/SE1i	-4,60	-3,55	-1,60	1,50
MIN-A/SE1j	-4,55	-3,30	-0,80	1,88

A-1-4a: Modal composition of the fall deposit of MIN-A samples. Separated by range size (>32 mm, 32-16 mm, 16-8 mm, 8-4 mm) and combined composition for all size ranges analyzed (global).

>32 mm	Juvenile clasts				Lithic clasts			
Sample No.	pumice	tube pumice	banded pumice	mafic scoria	crystalline clots	lava lithics	hydrothermally altered lithics	misc. Lithics
MIN-A/SE1a	33.95	13.79	0.00	0.00	49.07	0.00	0.00	3.18
MIN-A/SE1b	71.31	22.84	0.00	0.00	0.00	0.00	0.00	5.85
MIN-A/SE1c	61.41	27.80	5.81	0.00	4.98	0.00	0.00	0.00
MIN-A/SE1d	77.95	22.05	0.00	0.00	0.00	0.00	0.00	0.00
MIN-A/SE1e	61.22	38.78	0.00	0.00	0.00	0.00	0.00	0.00
MIN-A/SE1f	13.45	11.38	0.00	0.00	0.00	75.17	0.00	0.00
MIN-A/SE1g	53.09	46.91	0.00	0.00	0.00	0.00	0.00	0.00
MIN-A/SE1h	37.60	44.80	0.00	0.00	0.00	0.00	17.60	0.00
MIN-A/SE1i	15.58	7.79	0.00	31.17	0.00	45.45	0.00	0.00
MIN-A/SE1j	14.77	14.09	0.00	31.54	0.00	0.00	39.60	0.00

32-16 mm	Juvenile clasts				Lithic clasts			
Sample No.	pumice	tube pumice	banded pumice	mafic scoria	crystalline clots	lava lithics	hydrothermally altered lithics	misc. Lithics
MIN-A/SE1a	54.32	24.50	1.89	0.00	12.43	0.00	3.79	3.08
MIN-A/SE1b	69.69	22.95	0.51	0.00	2.23	2.74	0.00	1.88
MIN-A/SE1c	68.76	23.09	0.00	0.00	0.51	2.38	4.24	1.02
MIN-A/SE1d	75.49	13.39	0.00	0.61	1.67	1.37	5.18	2.28
MIN-A/SE1e	78.05	13.97	0.00	1.33	0.00	4.21	2.44	0.00
MIN-A/SE1f	70.29	8.75	1.06	0.00	3.45	3.98	12.47	0.00
MIN-A/SE1g	83.56	9.32	0.00	2.47	1.64	0.00	3.01	0.00
MIN-A/SE1h	67.00	13.40	0.74	12.66	1.74	0.00	4.47	0.00
MIN-A/SE1i	63.68	6.62	0.00	4.91	2.78	6.84	15.17	0.00
MIN-A/SE1j	59.25	8.38	2.02	19.65	0.00	0.00	10.69	0.00

A-1-4b: Modal composition of the fall deposit of MIN-A samples. Separated by range size (>32 mm, 32-16 mm, 16-8 mm, 8-4 mm) and combined composition for all size ranges analyzed (global).

16-8 mm	Juvenile clasts				Lithic clasts			
Sample No.	pumice	tube pumice	banded pumice	mafic scoria	crystalline clots	lava lithics	hydrothermally altered lithics	misc. Lithics
MIN-A/SE1a	73,52	7,71	1,03	1,29	5,66	4,63	6,17	0,00
MIN-A/SE1b	85,27	5,48	1,03	0,00	1,03	4,45	2,74	0,00
MIN-A/SE1c	86,83	5,64	0,00	0,00	0,00	1,25	5,96	0,31
MIN-A/SE1d	82,30	5,90	0,00	4,35	1,55	2,80	2,48	0,62
MIN-A/SE1e	85,03	8,50	0,00	2,04	2,38	1,36	0,68	0,00
MIN-A/SE1f	81,16	3,77	0,00	2,40	1,37	6,51	3,08	1,71
MIN-A/SE1g	81,04	6,23	0,26	3,90	1,04	2,34	5,19	0,00
MIN-A/SE1h	80,78	7,79	2,08	3,38	0,78	2,08	3,12	0,00
MIN-A/SE1i	72,29	8,31	0,00	8,06	0,00	3,78	7,56	0,00
MIN-A/SE1j	55,62	11,24	1,73	14,70	0,86	0,86	14,99	0,00

8-4mm	Juvenile clasts				Lithic clasts			
Sample No.	pumice	tube pumice	banded pumice	mafic scoria	crystalline clots	lava lithics	hydrothermally altered lithics	misc. Lithics
MIN-A/SE1a	70,76	5,88	1,71	1,12	8,56	3,65	8,33	0,00
MIN-A/SE1b	83,57	4,56	0,58	2,24	2,24	3,11	3,69	0,00
MIN-A/SE1c	83,90	5,20	0,56	1,05	2,18	2,53	4,57	0,00
MIN-A/SE1d	73,96	8,14	0,90	1,79	4,56	5,21	5,45	0,00
MIN-A/SE1e	81,32	7,45	1,28	1,71	1,34	2,99	3,91	0,00
MIN-A/SE1f	79,48	4,04	1,27	2,85	1,11	4,91	6,34	0,00
MIN-A/SE1g	77,21	4,88	0,94	3,01	1,78	4,74	7,45	0,00
MIN-A/SE1h	74,18	7,43	1,01	4,80	1,28	5,07	6,23	0,00
MIN-A/SE1i	69,63	5,81	0,72	10,28	2,47	4,06	7,04	0,00
MIN-A/SE1j	57,05	7,91	0,91	11,53	1,72	7,20	13,68	0,00

A-1-4c: Modal composition of the fall deposit of MIN-A samples. Separated by range size (>32 mm, 32-16 mm, 16-8 mm, 8-4 mm) and combined composition for all size ranges analyzed (global).

global	Juvenile clasts				Lithic clasts			
Sample No.	pumice	tube pumice	banded pumice	mafic scoria	crystalline clots	lava lithics	hydrothermally altered lithics	misc. Lithics
MIN-A/SE1a	55,47	17,01	1,28	0,37	18,53	1,31	3,85	2,18
MIN-A/SE1b	74,83	17,35	0,50	0,23	1,39	2,42	0,95	2,33
MIN-A/SE1c	73,52	17,69	1,15	0,12	1,40	1,67	3,91	0,54
MIN-A/SE1d	77,38	11,80	0,09	1,64	1,76	1,99	3,96	1,38
MIN-A/SE1e	78,16	14,89	0,20	1,40	0,87	2,64	1,84	0,00
MIN-A/SE1f	49,47	8,37	0,41	0,77	1,34	34,63	4,65	0,36
MIN-A/SE1g	78,99	10,24	0,28	2,91	1,32	1,80	4,46	0,00
MIN-A/SE1h	69,97	13,59	1,16	6,52	1,14	1,80	5,81	0,00
MIN-A/SE1i	61,35	7,19	0,12	10,14	1,47	10,29	9,45	0,00
MIN-A/SE1j	51,31	10,04	1,42	18,08	0,63	1,72	16,80	0,00

A-1-5a: Density averages, standard deviations and corresponding vesicularity of all pumice clasts analyzed.

Sample No.	Density av (kg/m³)	Stddev (kg/m³)	Vesicularity (%)
MIN-A/SE1a I f.p	831,13	70,95	66,75
MIN-A/SE1a II f.p.	683,60	52,78	72,66
MIN-A/SE1a III f.p.	536,56	17,94	78,54
MIN-A/SE1a IV f.p.	808,88	39,57	67,64
MIN-A/SE1a V f.p.	914,08	160,60	63,44
MIN-A/SE1a VI f.p.	478,91	3,78	80,84
MIN-A/SE1a VII f.p.	914,08	160,60	63,44
MIN-A/SE1a VIII f.p.	635,66	95,77	74,57
MIN-A/SE1a IX f.p.	601,65	9,85	75,93
MIN-A/SE1a X f.p.	469,49	17,99	81,22
MIN-A/SE1b I f.p.	586,82	62,45	76,53
MIN-A/SE1b II f.p.	539,03	49,65	78,44
MIN-A/SE1b III f.p.	759,61	35,34	69,62
MIN-A/SE1b IV f.p.	510,07	49,79	79,60
MIN-A/SE1b V f.p.	398,59	11,15	84,06
MIN-A/SE1b VI f.p.	732,19	29,28	70,71
MIN-A/SE1b VII f.p.	562,29	27,30	77,51
MIN-A/SE1b VIII f.p.	900,74	10,81	63,97
MIN-A/SE1b IX f.p.	893,78	29,26	64,25
MIN-A/SE1b X f.p.	856,09	9,94	65,76
MIN-A/SE1c I f.p.	750,50	59,74	69,98
MIN-A/SE1c II f.p.	748,47	7,03	70,06
MIN-A/SE1c III f.p.	630,37	9,76	74,79
MIN-A/SE1c IV f.p.	907,76	16,29	63,69
MIN-A/SE1c V f.p.	593,15	14,29	76,27
MIN-A/SE1c VI f.p.	917,22	17,23	63,31
MIN-A/SE1c VII f.p.	525,69	13,93	78,97
MIN-A/SE1c VIII f.p.	486,27	14,64	80,55
MIN-A/SE1c IX f.p.	700,35	12,26	71,99
MIN-A/SE1c X f.p.	466,70	8,63	81,33
MIN-A/SE1d I f.p.	381,80	21,02	84,73
MIN-A/SE1d II f.p.	354,68	3,36	85,81
MIN-A/SE1d III f.p.	339,83	19,66	86,41
MIN-A/SE1d IV f.p.	288,01	0,90	88,48
MIN-A/SE1d V f.p.	316,04	2,71	87,36
MIN-A/SE1d VI f.p.	273,02	1,13	89,08
MIN-A/SE1d VII f.p.	247,90	7,76	90,08
MIN-A/SE1d VIII f.p.	352,76	1,46	85,89
MIN-A/SE1d IX f.p.	331,25	1,23	86,75
MIN-A/SE1d X f.p.	371,77	0,99	85,13

A-1-5b: Density averages, standard deviations and corresponding vesicularity of all pumice clasts analyzed.

Sample No.	Density av (kg/m³)	Stddev (kg/m³)	Vesicularity (%)
MIN-A/SE1e I f.p.	253,97	3,30	89,84
MIN-A/SE1e II f.p.	665,12	37,85	73,40
MIN-A/SE1e III f.p.	424,45	2,77	83,02
MIN-A/SE1e IV f.p.	297,82	10,83	88,09
MIN-A/SE1e V f.p.	456,45	4,13	81,74
MIN-A/SE1e VI f.p.	453,04	60,40	81,88
MIN-A/SE1e VII f.p.	267,77	3,19	89,29
MIN-A/SE1e VIII f.p.	435,93	2,12	82,56
MIN-A/SE1e IX f.p.	418,01	3,76	83,28
MIN-A/SE1e X f.p.	460,55	1,29	81,58
MIN-A/SE1f I f.p.	222,01	10,75	91,12
MIN-A/SE1f II f.p.	221,86	10,91	91,13
MIN-A/SE1f III f.p.	327,18	31,92	86,91
MIN-A/SE1f IV f.p.	322,13	5,34	87,11
MIN-A/SE1f V f.p.	256,63	14,00	89,73
MIN-A/SE1f VI f.p.	236,13	6,75	90,55
MIN-A/SE1f VII f.p.	323,22	2,80	87,07
MIN-A/SE1f VIII f.p.	362,43	5,41	85,50
MIN-A/SE1f IX f.p.	319,72	6,99	87,21
MIN-A/SE1f X f.p.	285,94	2,93	88,56
MIN-A/SE1g I f.p.	291,88	1,19	88,32
MIN-A/SE1g II f.p.	425,53	5,82	82,98
MIN-A/SE1g III f.p.	407,31	1,13	83,71
MIN-A/SE1g IV f.p.	299,55	8,25	88,02
MIN-A/SE1g V f.p.	353,42	30,63	85,86
MIN-A/SE1g VI f.p.	209,14	2,80	91,63
MIN-A/SE1g VII f.p.	236,45	2,25	90,54
MIN-A/SE1g VIII f.p.	279,08	3,38	88,84
MIN-A/SE1g IX f.p.	304,22	1,41	87,83
MIN-A/SE1g X f.p.	346,26	3,89	86,15
MIN-A/SE1h I f.p.	269,35	1,85	89,23
MIN-A/SE1h II f.p.	435,13	56,39	82,59
MIN-A/SE1h III f.p.	276,44	1,49	88,94
MIN-A/SE1h IV f.p.	343,82	1,17	86,25
MIN-A/SE1h V f.p.	265,67	2,11	89,37
MIN-A/SE1h VI f.p.	237,32	1,94	90,51
MIN-A/SE1h VII f.p.	346,45	2,86	86,14
MIN-A/SE1h VIII f.p.	313,00	1,40	87,48
MIN-A/SE1h IX f.p.	343,49	14,96	86,26
MIN-A/SE1h X f.p.	204,87	2,34	91,81

A-1-5c: Density averages, standard deviations and corresponding vesicularity of all pumice clasts analyzed.

Sample No.	Density av (kg/m³)	Stddev (kg/m³)	Vesicularity (%)
MIN-A/SE1i I f.p.	317,67	0,63	87,29
MIN-A/SE1i II f.p.	357,66	4,05	85,69
MIN-A/SE1i III f.p.	337,73	4,47	86,49
MIN-A/SE1i IV f.p.	264,03	1,37	89,44
MIN-A/SE1i V f.p.	233,42	2,43	90,66
MIN-A/SE1i VI f.p.	218,71	0,65	91,25
MIN-A/SE1i VII f.p.	326,96	1,16	86,92
MIN-A/SE1i VIII f.p.	409,27	3,26	83,63
MIN-A/SE1i IX f.p.	268,78	0,98	89,25
MIN-A/SE1i X f.p.	408,42	2,45	83,66
MIN-A/SE1j I f.p.	449,17	2,07	82,03
MIN-A/SE1j II f.p.	363,62	1,26	85,46
MIN-A/SE1j III f.p.	269,81	2,71	89,21
MIN-A/SE1j IV f.p.	316,69	2,35	87,33
MIN-A/SE1j V f.p.	354,83	0,93	85,81
MIN-A/SE1j VI f.p.	345,64	4,76	86,17
MIN-A/SE1j VII f.p.	487,56	16,27	80,50
MIN-A/SE1j VIII f.p.	540,13	8,27	78,39
MIN-A/SE1j IX f.p.	349,14	43,36	86,03
MIN-A/SE1j X f.p.	395,74	3,15	84,17

A-1-5d: Average density, standard deviation and vesicularity for all pumice clasts of each stage.

Sample No.	Density av (kg/m³)	Stddev (kg/m³)	Vesicularity (%)
MIN-A/SE1a	687.40	170.60	72.50
MIN-A/SE1b	673.92	177.83	73.04
MIN-A/SE1c	672.65	161.43	73.09
MIN-A/SE1d	325.71	43.99	86.97
MIN-A/SE1e	413.31	120.02	83.47
MIN-A/SE1f	287.72	50.44	88.49
MIN-A/SE1g	315.28	68.92	87.39
MIN-A/SE1h	303.55	66.60	87.86
MIN-A/SE1i	314.26	67.30	87.43
MIN-A/SE1j	387.23	82.26	84.51

A-1-5e: Density averages, standard deviations and corresponding vesicularity of all tube-pumice clasts analyzed.

Sample No.	Density av (kg/m³)	Stddev (kg/m³)	Vesicularity (%)
MIN-A/SE1a I f.tp	817,62	68,60	67,30
MIN-A/SE1a II f.tp	849,33	40,08	66,03
MIN-A/SE1a III f.tp	478,95	22,41	80,84
MIN-A/SE1a IV f.tp	697,28	31,04	72,11
MIN-A/SE1a V f.tp	831,79	27,50	66,73
MIN-A/SE1a VI f.tp	745,82	18,93	70,17
MIN-A/SE1a VII f.tp	527,05	33,20	78,92
MIN-A/SE1a VIII f.tp	425,06	23,60	83,00
MIN-A/SE1a IX f.tp	849,56	59,55	66,02
MIN-A/SE1a X f.tp	822,95	24,80	67,08
MIN-A/SE1b I f.tp	645,54	46,00	74,18
MIN-A/SE1b II f.tp	543,66	7,22	78,25
MIN-A/SE1b III f.tp	484,03	7,11	80,64
MIN-A/SE1b IV f.tp	752,83	14,84	69,89
MIN-A/SE1b V f.tp	569,32	9,35	77,23
MIN-A/SE1b VI f.tp	639,20	7,37	74,43
MIN-A/SE1b VII f.tp	347,28	14,14	86,11
MIN-A/SE1b VIII f.tp	683,67	8,12	72,65
MIN-A/SE1b IX f.tp	711,55	9,02	71,54
MIN-A/SE1b X f.tp	737,05	7,37	70,52
MIN-A/SE1c I f.tp	469,66	24,67	81,21
MIN-A/SE1c II f.tp	236,12	0,80	90,56
MIN-A/SE1c III f.tp	397,42	4,99	84,10
MIN-A/SE1c IV f.tp	340,50	3,87	86,38
MIN-A/SE1c V f.tp	321,44	8,93	87,14
MIN-A/SE1c VI f.tp	290,47	0,97	88,38
MIN-A/SE1c VII f.tp	262,98	9,16	89,48
MIN-A/SE1c VIII f.tp	438,98	7,23	82,44
MIN-A/SE1c IX f.tp	414,89	8,99	83,40
MIN-A/SE1c X f.tp	656,61	4,70	73,74
MIN-A/SE1d I f.tp	259,81	0,86	89,61
MIN-A/SE1d II f.tp	232,98	2,36	90,68
MIN-A/SE1d III f.tp	246,70	13,03	90,13
MIN-A/SE1d IV f.tp	410,09	2,05	83,60
MIN-A/SE1d f.tp	144,59	4,98	94,22
MIN-A/SE1d VI f.tp	305,22	3,51	87,79
MIN-A/SE1d VII f.tp	217,60	1,02	91,30
MIN-A/SE1d VIII f.tp	159,59	0,98	93,62
MIN-A/SE1d IX f.tp	155,71	7,74	93,77
MIN-A/SE1d X f.tp	306,40	10,79	87,74

A-1-5f: Density averages, standard deviations and corresponding vesicularity of all tube-pumice clasts analyzed.

Sample No.	Density av (kg/m³)	Stddev (kg/m³)	Vesicularity (%)
MIN-A/SE1e I f.tp	446,27	1,02	82,15
MIN-A/SE1e II f.tp	508,64	2,10	79,65
MIN-A/SE1e III f.tp	437,48	4,28	82,50
MIN-A/SE1e IV f.tp	420,13	1,20	83,19
MIN-A/SE1e V f.tp	309,82	3,13	87,61
MIN-A/SE1e VI f.tp	401,64	3,00	83,93
MIN-A/SE1e VII f.tp	497,61	1,29	80,10
MIN-A/SE1e VIII f.tp	379,72	1,23	84,81
MIN-A/SE1e IX f.tp	307,09	0,75	87,72
MIN-A/SE1f I f.tp	219,17	3,15	91,23
MIN-A/SE1f II f.tp	283,26	4,08	88,67
MIN-A/SE1f III f.tp	280,19	1,29	88,79
MIN-A/SE1f IV f.tp	368,01	2,08	85,28
MIN-A/SE1f V f.tp	373,36	1,67	85,07
MIN-A/SE1f VI f.tp	360,08	5,90	85,60
MIN-A/SE1f VII f.tp	357,40	1,50	85,70
MIN-A/SE1f VIII f.tp	266,77	2,05	89,33
MIN-A/SE1f IX f.tp	376,33	3,32	84,95
MIN-A/SE1f X f.tp	265,17	3,16	89,39
MIN-A/SE1g I f.tp	219,40	4,18	91,22
MIN-A/SE1g II f.tp	323,26	4,38	87,07
MIN-A/SE1g III f.tp	400,69	1,88	83,97
MIN-A/SE1g IV f.tp	314,52	1,64	87,42
MIN-A/SE1g V f.tp	342,82	2,60	86,29
MIN-A/SE1g VI f.tp	293,44	8,38	88,26
MIN-A/SE1g VII f.tp	268,34	1,41	89,27
MIN-A/SE1g VIII f.tp	332,30	1,76	86,71
MIN-A/SE1g IX f.tp	351,87	3,10	85,93
MIN-A/SE1g X f.tp	274,94	0,60	89,00
MIN-A/SE1h I f.tp	372,28	1,88	85,11
MIN-A/SE1h II f.tp	395,99	6,50	84,16
MIN-A/SE1h III f.tp	444,22	6,04	82,23
MIN-A/SE1h IV f.tp	407,64	4,01	83,69
MIN-A/SE1h V f.tp	159,98	2,47	93,60
MIN-A/SE1h VI f.tp	253,47	1,17	89,86
MIN-A/SE1h VII f.tp	231,19	1,06	90,75
MIN-A/SE1h VIII f.tp	437,60	4,15	82,50
MIN-A/SE1h IX f.tp	253,37	3,34	89,87
MIN-A/SE1h X f.tp	239,24	7,15	90,43

A-1-5g: Density averages, standard deviations and corresponding vesicularity of all tube-pumice clasts analyzed.

Sample No.	Density av (kg/m³)	Stddev (kg/m³)	Vesicularity (%)
MIN-A/SE1i I f.tp	287.37	1.14	88.51
MIN-A/SE1i II f.tp	352.69	2.34	85.89
MIN-A/SE1i III f.tp	210.35	0.81	91.59
MIN-A/SE1i IV f.tp	256.61	2.62	89.74
MIN-A/SE1i V f.tp	210.55	3.28	91.58
MIN-A/SE1i VI f.tp	413.63	3.73	83.45
MIN-A/SE1i VII f.tp	327.98	3.35	86.88
MIN-A/SE1i VIII f.tp	251.07	2.52	89.96
MIN-A/SE1i IX f.tp	253.34	2.92	89.87
MIN-A/SE1i X f.tp	400.15	6.02	83.99
MIN-A/SE1j I f.tp	187.31	1.40	92.51
MIN-A/SE1j II f.tp	238.13	3.05	90.47
MIN-A/SE1j III f.tp	345.99	4.28	86.16
MIN-A/SE1j IV f.tp	225.49	0.83	90.98
MIN-A/SE1j V f.tp	273.93	0.59	89.04
MIN-A/SE1j VI f.tp	318.89	2.40	87.24
MIN-A/SE1j VII f.tp	264.15	0.57	89.43

A-1-5h: Average density, standard deviation and vesicularity for all tube-pumice clasts of each stage.

Sample No.	Density av (kg/m³)	Stddev (kg/m³)	Vesicularity (%)
MIN-A/SE1a	704.54	165.75	71.82
MIN-A/SE1b	611.41	127.07	75.54
MIN-A/SE1c	382.91	123.32	84.68
MIN-A/SE1d	243.87	82.40	90.25
MIN-A/SE1e	412.04	71.73	83.52
MIN-A/SE1f	314.97	57.75	87.40
MIN-A/SE1g	312.16	50.72	87.51
MIN-A/SE1h	319.50	102.38	87.22
MIN-A/SE1i	296.37	73.80	88.15
MIN-A/SE1j	264.84	54.56	89.41

A-1-6a: Permeability of all clasts analyzed.

Sample No	Pressure (hPa)	Flow (dm^3/min)	Density air (kg/m^3)	Core length (m)	Core diameter (m)	Core surface (m^2)	Permeability K_L (m/s)	Viscosity Air (Pa s)	Permeability K_0 (m^2)
MIN-A/SE1a, >32 mm I	5,00	0,13	1,24	0,040	0,025	0,0004909	4,29E-06	1,85E-05	6,53E-12
	6,10	0,16	1,24	0,040	0,025	0,0004909	4,33E-06	1,85E-05	6,59E-12
	7,00	0,17	1,24	0,040	0,025	0,0004909	4,01E-06	1,85E-05	6,10E-12
	8,10	0,19	1,24	0,040	0,025	0,0004909	3,87E-06	1,85E-05	5,89E-12
	9,10	0,21	1,24	0,040	0,025	0,0004909	3,81E-06	1,85E-05	5,80E-12
MIN-A/SE1a, >32 mm II	5,00	0,90	1,23	0,030	0,040	0,0012566	8,65E-06	1,86E-05	1,33E-11
	6,00	1,00	1,23	0,030	0,040	0,0012566	8,01E-06	1,86E-05	1,23E-11
	7,00	1,10	1,23	0,030	0,040	0,0012566	7,55E-06	1,86E-05	1,16E-11
	8,10	1,20	1,23	0,030	0,040	0,0012566	7,12E-06	1,86E-05	1,09E-11
	9,30	1,30	1,23	0,030	0,040	0,0012566	6,72E-06	1,86E-05	1,03E-11
MIN-A/SE1b, >32 mm I	5,10	0,11	1,24	0,065	0,025	0,0004909	5,78E-06	1,85E-05	8,80E-12
	6,10	0,12	1,24	0,065	0,025	0,0004909	5,27E-06	1,85E-05	8,03E-12
	7,40	0,14	1,24	0,065	0,025	0,0004909	5,07E-06	1,85E-05	7,72E-12
	8,40	0,16	1,24	0,065	0,025	0,0004909	5,10E-06	1,85E-05	7,77E-12
	9,40	0,17	1,24	0,065	0,025	0,0004909	4,85E-06	1,85E-05	7,38E-12
MIN-A/SE1b, >32 mm II	5,00	0,17	1,23	0,035	0,040	0,0012566	1,91E-06	1,86E-05	2,93E-12
	6,00	0,19	1,23	0,035	0,040	0,0012566	1,78E-06	1,86E-05	2,73E-12
	7,00	0,22	1,23	0,035	0,040	0,0012566	1,76E-06	1,86E-05	2,71E-12
	8,00	0,25	1,23	0,035	0,040	0,0012566	1,75E-06	1,86E-05	2,69E-12
	9,00	0,27	1,23	0,035	0,040	0,0012566	1,68E-06	1,86E-05	2,59E-12

A-1-6b: Permeability of all clasts analyzed.

Sample No	Pressure (hPa)	Flow (dm^3/min)	Density air (kg/m^3)	Core length (m)	Core diameter (m)	Core surface (m^2)	Permeability K_L (m/s)	Viscosity Air (Pa s)	Permeability K_0 (m^2)
MIN-A/SE1c, >32 mm I	7,00	0,04	1,19	0,035	0,025	0,0004909	7,9E-07	1,86E-05	1,26E-12
	8,00	0,05	1,19	0,035	0,025	0,0004909	8,7E-07	1,86E-05	1,38E-12
	9,10	0,06	1,19	0,035	0,025	0,0004909	9,2E-07	1,86E-05	1,45E-12
	10,00	0,05	1,19	0,035	0,025	0,0004909	6,9E-07	1,86E-05	1,10E-12
	12,10	0,06	1,19	0,035	0,025	0,0004909	6,9E-07	1,86E-05	1,09E-12
	15,70	0,08	1,19	0,035	0,025	0,0004909	7,1E-07	1,86E-05	1,12E-12
	23,60	0,08	1,19	0,035	0,025	0,0004909	4,7E-07	1,86E-05	7,48E-13
	35,90	0,10	1,19	0,035	0,025	0,0004909	3,9E-07	1,86E-05	6,15E-13
MIN-A/SE1c, >32 mm II	5,10	0,10	1,19	0,05	0,04	0,0012566	1,5E-06	1,86E-05	2,41E-12
	6,00	0,11	1,19	0,05	0,04	0,0012566	1,4E-06	1,86E-05	2,26E-12
	7,00	0,13	1,19	0,05	0,04	0,0012566	1,4E-06	1,86E-05	2,29E-12
MIN-A/SE1c, >32 mm III	8,10	0,10	1,24	0,025	0,025	0,0004909	1,3E-06	1,85E-05	1,94E-12
	9,10	0,11	1,24	0,025	0,025	0,0004909	1,2E-06	1,85E-05	1,90E-12
	10,10	0,12	1,24	0,025	0,025	0,0004909	1,2E-06	1,85E-05	1,87E-12
	11,10	0,13	1,24	0,025	0,025	0,0004909	1,2E-06	1,85E-05	1,84E-12
	12,30	0,14	1,24	0,025	0,025	0,0004909	1,2E-06	1,85E-05	1,79E-12
MIN-A/SE1c pu1 I	5,00	0,05	1,23	0,035	0,025	0,0004909	1,4E-06	1,86E-05	2,21E-12
	6,00	0,06	1,23	0,035	0,025	0,0004909	1,4E-06	1,86E-05	2,21E-12
	7,00	0,07	1,23	0,035	0,025	0,0004909	1,4E-06	1,86E-05	2,21E-12
	8,10	0,08	1,23	0,035	0,025	0,0004909	1,4E-06	1,86E-05	2,18E-12
	9,30	0,10	1,23	0,035	0,025	0,0004909	1,5E-06	1,86E-05	2,37E-12
MIN-A/SE1d, >32 mm I	5,00	0,45	1,23	0,040	0,040	0,0012566	5,8E-06	1,86E-05	8,87E-12
	6,00	0,50	1,23	0,040	0,040	0,0012566	5,3E-06	1,86E-05	8,21E-12
	7,00	0,58	1,23	0,040	0,040	0,0012566	5,3E-06	1,86E-05	8,09E-12
	8,00	0,65	1,23	0,040	0,040	0,0012566	5,2E-06	1,86E-05	8,00E-12
	9,00	0,70	1,23	0,040	0,040	0,0012566	5,0E-06	1,86E-05	7,66E-12

A-1-6c: Permeability of all clasts analyzed.

Sample No	Pressure (hPa)	Flow (dm^3/min)	Density air (kg/m^3)	Core length (m)	Core diameter (m)	Core surface (m^2)	Permeability K_L (m/s)	Viscosity Air (Pa s)	Permeability K_0 (m^2)
MIN-A/SE1d pu1 I	5,00	0,24	1,23	0,035	0,040	0,0012566	5,00	2,69E-06	1,86E-05
	6,10	0,28	1,23	0,035	0,040	0,0012566	6,10	2,57E-06	1,86E-05
	7,00	0,32	1,23	0,035	0,040	0,0012566	7,00	2,56E-06	1,86E-05
	8,00	0,35	1,23	0,035	0,040	0,0012566	8,00	2,45E-06	1,86E-05
	9,00	0,40	1,23	0,035	0,040	0,0012566	9,00	2,49E-06	1,86E-05
MIN-A/SE1e, >32 mm I	5,00	0,07	1,24	0,030	0,025	0,0004909	5,00	1,73E-06	1,85E-05
	6,00	0,09	1,24	0,030	0,025	0,0004909	6,00	1,86E-06	1,85E-05
	7,00	0,10	1,24	0,030	0,025	0,0004909	7,00	1,77E-06	1,85E-05
	8,00	0,11	1,24	0,030	0,025	0,0004909	8,00	1,70E-06	1,85E-05
	9,10	0,12	1,24	0,030	0,025	0,0004909	9,10	1,63E-06	1,85E-05
MIN-A/SE1e, >32 mm II	5,00	0,11	1,23	0,030	0,040	0,0012566	5,00	1,06E-06	1,86E-05
	6,10	0,12	1,23	0,030	0,040	0,0012566	6,10	9,46E-07	1,86E-05
	7,10	0,14	1,23	0,030	0,040	0,0012566	7,10	9,48E-07	1,86E-05
	8,10	0,16	1,23	0,030	0,040	0,0012566	8,10	9,50E-07	1,86E-05
	9,30	0,18	1,23	0,030	0,040	0,0012566	9,30	9,30E-07	1,86E-05
MIN-A/SE1f, >32 mm I	1,00	0,50	1,24	0,045	0,025	0,0004909	1,00	9,28E-05	1,85E-05
	2,00	0,83	1,24	0,045	0,025	0,0004909	2,00	7,65E-05	1,85E-05
	3,00	1,15	1,24	0,045	0,025	0,0004909	3,00	7,11E-05	1,85E-05
	4,00	1,35	1,24	0,045	0,025	0,0004909	4,00	6,26E-05	1,85E-05
	5,00	1,55	1,24	0,045	0,025	0,0004909	5,00	5,75E-05	1,85E-05
MIN-A/SE1f, >32 mm II	5,00	0,18	1,23	0,035	0,040	0,0012566	5,00	2,02E-06	1,86E-05
	6,00	0,21	1,23	0,035	0,040	0,0012566	6,00	1,96E-06	1,86E-05
	7,00	0,24	1,23	0,035	0,040	0,0012566	7,00	1,92E-06	1,86E-05
	8,00	0,26	1,23	0,035	0,040	0,0012566	8,00	1,82E-06	1,86E-05
	9,00	0,28	1,23	0,035	0,040	0,0012566	9,00	1,74E-06	1,86E-05

A-1-6d: Permeability of all clasts analyzed.

Sample No	Pressure (hPa)	Flow (dm^3/min)	Density air (kg/m^3)	Core length (m)	Core diameter (m)	Core surface (m^2)	Permeability K_L (m/s)	Viscosity Air (Pa s)	Permeability K_0 (m^2)
MIN-A/SE1f pu1 I	19,30	22,50	1,24	0,035	0,025	0,0004909	5,98E-07	1,85E-05	9,11E-13
	20,30	22,50	1,24	0,035	0,025	0,0004909	6,40E-07	1,85E-05	9,74E-13
	21,30	22,50	1,24	0,035	0,025	0,0004909	6,44E-07	1,85E-05	9,80E-13
	22,20	22,50	1,24	0,035	0,025	0,0004909	6,50E-07	1,85E-05	9,90E-13
	23,30	22,50	1,24	0,035	0,025	0,0004909	6,19E-07	1,85E-05	9,43E-13
MIN-A/SE1f pu1 II	5,00	24,00	1,23	0,060	0,025	0,0004909	7,38E-06	1,86E-05	1,13E-11
	6,00	24,00	1,23	0,060	0,025	0,0004909	7,38E-06	1,86E-05	1,13E-11
	7,10	24,00	1,23	0,060	0,025	0,0004909	6,93E-06	1,86E-05	1,07E-11
	8,00	24,00	1,23	0,060	0,025	0,0004909	6,77E-06	1,86E-05	1,04E-11
	9,00	24,00	1,23	0,060	0,025	0,0004909	6,84E-06	1,86E-05	1,05E-11
MIN-A/SE1g, >32 mm I	5,00	22,50	1,24	0,045	0,025	0,0004909	2,23E-06	1,85E-05	3,39E-12
	6,10	22,50	1,24	0,045	0,025	0,0004909	2,43E-06	1,85E-05	3,71E-12
	7,30	22,50	1,24	0,045	0,025	0,0004909	2,54E-06	1,85E-05	3,87E-12
	8,10	22,50	1,24	0,045	0,025	0,0004909	2,29E-06	1,85E-05	3,49E-12
	9,20	22,50	1,24	0,045	0,025	0,0004909	2,22E-06	1,85E-05	3,38E-12
MIN-A/SE1h, >32 mm I	6,20	22,50	1,24	0,030	0,025	0,0004909	1,40E-06	1,85E-05	2,13E-12
	7,30	22,50	1,24	0,030	0,025	0,0004909	1,52E-06	1,85E-05	2,32E-12
	8,20	22,50	1,24	0,030	0,025	0,0004909	1,51E-06	1,85E-05	2,30E-12
	9,20	22,50	1,24	0,030	0,025	0,0004909	1,34E-06	1,85E-05	2,05E-12
	10,20	22,50	1,24	0,030	0,025	0,0004909	1,33E-06	1,85E-05	2,03E-12
MIN-A/SE1h pu1 I	5,10	24,00	1,23	0,035	0,025	0,0004909	3,94E-06	1,86E-05	6,06E-12
	6,10	24,00	1,23	0,035	0,025	0,0004909	3,77E-06	1,86E-05	5,79E-12
	7,10	24,00	1,23	0,035	0,025	0,0004909	3,64E-06	1,86E-05	5,59E-12
	8,10	24,00	1,23	0,035	0,025	0,0004909	3,55E-06	1,86E-05	5,45E-12
	9,10	24,00	1,23	0,035	0,025	0,0004909	3,47E-06	1,86E-05	5,33E-12

A-1-6e: Permeability of all clasts analyzed.

Sample No	Pressure (hPa)	Flow (dm^3/min)	Density air (kg/m^3)	Core length (m)	Core diameter (m)	Core surface (m^2)	Permeability K_L (m/s)	Viscosity Air (Pa s)	Permeability K_0 (m^2)
MIN-A/SE1i pu1 I	5,00	0,21	1,23	0,025	0,025	0,0004909	4,31E-06	1,86E-05	6,62E-12
	6,00	0,24	1,23	0,025	0,025	0,0004909	4,10E-06	1,86E-05	6,30E-12
	7,00	0,26	1,23	0,025	0,025	0,0004909	3,81E-06	1,86E-05	5,85E-12
	8,00	0,28	1,23	0,025	0,025	0,0004909	3,59E-06	1,86E-05	5,52E-12
	9,00	0,30	1,23	0,025	0,025	0,0004909	3,42E-06	1,86E-05	5,25E-12
MIN-A/SE1i pu1 II	5,00	0,40	1,23	0,035	0,040	0,0012566	4,49E-06	1,86E-05	6,90E-12
	6,00	0,48	1,23	0,035	0,040	0,0012566	4,44E-06	1,86E-05	6,82E-12
	7,00	0,55	1,23	0,035	0,040	0,0012566	4,41E-06	1,86E-05	6,77E-12
	8,00	0,58	1,23	0,035	0,040	0,0012566	4,03E-06	1,86E-05	6,19E-12
	9,10	0,63	1,23	0,035	0,040	0,0012566	3,85E-06	1,86E-05	5,92E-12
MIN-A/SE1j, >32 mm I	10,10	0,09	1,24	0,025	0,025	0,0004909	9,18E-07	1,85E-05	1,40E-12
	11,20	0,10	1,24	0,025	0,025	0,0004909	9,20E-07	1,85E-05	1,40E-12
	12,20	0,10	1,24	0,025	0,025	0,0004909	8,45E-07	1,85E-05	1,29E-12
	13,20	0,11	1,24	0,025	0,025	0,0004909	8,59E-07	1,85E-05	1,31E-12
	14,20	0,12	1,24	0,025	0,025	0,0004909	8,71E-07	1,85E-05	1,33E-12

A-1-6f: Average permeability per sample.

Sample number	Permeability (m^2)
MIN-A/SE1a, >32 mm I	6.12595E-12
MIN-A/SE1a, >32 mm II	1.15942E-11
MIN-A/SE1b, >32 mm I	7.87097E-12
MIN-A/SE1b, >32 mm II	2.70525E-12
MIN-A/SE1c, >32 mm I	1.08759E-12
MIN-A/SE1c, >32 mm II	2.29878E-12
MIN-A/SE1c, >32 mm III	1.84852E-12
MIN-A/SE1c pu1 I	2.21433E-12
MIN-A/SE1d, >32 mm I	8.09324E-12
MIN-A/SE1d pu1 I	3.89202E-12
MIN-A/SE1e, >32 mm I	2.622E-12
MIN-A/SE1e, >32 mm II	1.47168E-12
MIN-A/SE1f, >32 mm I	1.08842E-10
MIN-A/SE1f, >32 mm II	2.88552E-12
MIN-A/SE1f pu1 I	9.51168E-13
MIN-A/SE1f pu1 II	1.07551E-11
MIN-A/SE1g, >32 mm I	3.53496E-12
MIN-A/SE1h, >32 mm I	2.14577E-12
MIN-A/SE1h pu1 I	5.59386E-12
MIN-A/SE1i pu1 I	5.85679E-12
MIN-A/SE1i pu1 II	6.46297E-12
MIN-A/SE1j, >32 mm I	1.33237E-12

A-1-6g: Average permeability per stage.

Stages	Averages/stage
MINA-A/SE1a	8.86005E-12
MINA-A/SE1b	5.28811E-12
MINA-A/SE1c	1.86231E-12
MINA-A/SE1d	5.99263E-12
MINA-A/SE1e	2.04684E-12
MINA-A/SE1f (average including SE1f >32 mm I tube-pumice)	4.86394E-12 3.08584E-11
MINA-A/SE1g	3.53496E-12
MINA-A/SE1h	3.86982E-12
MINA-A/SE1i	6.15988E-12
MINA-A/SE1j	1.33237E-12

A-1-7: Shape parameter (formafactor, solidity, elongation) averages and standard devations.

	Formfactor		Solidity		Elongation	
Sample No.	**average**	**stddev.**	**average**	**stddev.**	**average**	**stddev.**
MIN-A/SE1a	0.8158	0.0728	0.8880	0.0443	1.5396	0.2693
MIN-A/SE1b	0.8264	0.0896	0.8899	0.0451	1.5487	0.3794
MIN-A/SE1c	0.8125	0.0759	0.9023	0.0431	1.4885	0.2664
MIN-A/SE1d	0.8484	0.0782	0.9001	0.0405	1.4857	0.2968
MIN-A/SE1e	0.8505	0.0798	0.9005	0.0474	1.4855	0.2909
MIN-A/SE1f	0.8352	0.0758	0.8979	0.0408	1.4853	0.2780
MIN-A/SE1g	0.8628	0.0610	0.9125	0.0350	1.5014	0.2348
MIN-A/SE1h	0.8711	0.0628	0.9130	0.0340	1.4600	0.2561
MIN-A/SE1i	0.8628	0.0569	0.9075	0.0332	1.4482	0.2357
MIN-A/SE1j	0.8513	0.0660	0.9003	0.0341	1.4891	0.2982

A-1-8a: Volume frequency distribution.

Sample No.	**SE1a**	**SE1b**	**SE1c**	**SE1d**	**SE1e**	**SE1f**	**SE1g**	**SE1h**	**SE1i**	**SE1j**
Thin section	**TS35**	**TS39**	**TS42**	**TS45**	**TS48**	**TS51**	**TS54**	**TS57**	**TS60**	**TS63**
diameter (µm)										
10000	0.000	0.000	0.000	0.000	0.000	0.000	0.000	0.000	0.000	0.000
9000	0.000	0.000	0.000	0.000	0.000	0.000	0.000	0.000	0.000	0.000
8000	0.000	0.000	0.000	0.000	0.000	0.000	0.000	0.000	0.000	0.000
7000	0.000	0.000	0.000	0.000	0.000	0.000	0.000	0.000	0.000	0.000
6000	0.000	0.000	0.000	0.000	0.000	0.000	0.000	0.000	0.000	0.000
5000	0.000	0.000	0.000	0.000	0.000	0.000	0.000	0.000	0.000	0.000
4000	0.000	0.000	0.000	0.000	0.000	0.000	0.000	0.000	0.000	0.000
3000	0.000	0.000	0.477	0.000	0.000	0.000	0.000	0.000	0.000	0.000
2000	0.000	0.000	0.296	0.000	0.000	0.000	0.000	0.623	0.000	0.000
1000	0.000	0.261	0.077	0.418	0.000	0.126	0.524	0.148	0.542	0.350
900	0.000	0.000	0.027	0.000	0.000	0.000	0.025	0.058	0.073	0.057
800	0.000	0.000	0.008	0.105	0.000	0.000	0.035	0.013	0.038	0.000
700	0.000	0.000	0.006	0.043	0.063	0.046	0.070	0.000	0.049	0.030
600	0.083	0.000	0.014	0.046	0.175	0.112	0.073	0.017	0.048	0.038
500	0.159	0.084	0.006	0.017	0.083	0.082	0.031	0.036	0.035	0.046
400	0.157	0.125	0.020	0.086	0.069	0.104	0.036	0.021	0.035	0.107
300	0.113	0.130	0.019	0.063	0.126	0.159	0.053	0.020	0.041	0.066
200	0.187	0.125	0.018	0.080	0.149	0.167	0.059	0.026	0.048	0.106
100	0.181	0.139	0.019	0.083	0.173	0.150	0.056	0.023	0.051	0.125
90	0.023	0.015	0.002	0.009	0.021	0.010	0.005	0.002	0.006	0.014
80	0.020	0.017	0.002	0.009	0.022	0.010	0.006	0.002	0.006	0.014
70	0.023	0.019	0.002	0.009	0.024	0.009	0.006	0.002	0.006	0.013
60	0.021	0.021	0.002	0.009	0.026	0.008	0.005	0.002	0.006	0.013
50	0.015	0.020	0.002	0.009	0.026	0.006	0.005	0.002	0.005	0.011
40	0.010	0.020	0.001	0.007	0.022	0.005	0.004	0.002	0.004	0.006
30	0.005	0.014	0.001	0.005	0.015	0.003	0.004	0.001	0.003	0.003
20	0.002	0.007	0.000	0.002	0.006	0.002	0.002	0.001	0.002	0.001
10	0.000	0.002	0.000	0.000	0.001	0.000	0.001	0.000	0.000	0.000

A-1-8b:Number volume distribution (N_V).

Sample No. Thin section	SE1a TS35	SE1b TS39	SE1c TS42	SE1d TS45	SE1e TS48	SE1f TS51	SE1g TS54	SE1h TS57	SE1i TS60	SE1j TS63
diameter (µm)										
10000	0.00	0.00	0.00	0.00	0.00	0.00	0.00	0.00	0.00	0.00
9000	0.00	0.00	0.00	0.00	0.00	0.00	0.00	0.00	0.00	0.00
8000	0.00	0.00	0.00	0.00	0.00	0.00	0.00	0.00	0.00	0.00
7000	0.00	0.00	0.00	0.00	0.00	0.00	0.00	0.00	0.00	0.00
6000	0.00	0.00	0.00	0.00	0.00	0.00	0.00	0.00	0.00	0.00
5000	0.00	0.00	0.00	0.00	0.00	0.00	0.00	0.00	0.00	0.00
4000	0.00	0.00	0.00	0.00	0.00	0.00	0.00	0.00	0.00	0.00
3000	0.00	0.00	0.44	0.00	0.00	0.00	0.00	0.00	0.00	0.00
2000	0.00	0.00	1.24	0.00	0.00	0.00	0.00	0.71	0.00	0.00
1000	0.00	1.21	4.91	1.71	0.00	0.48	2.40	5.67	5.79	1.13
900	0.00	1.21	8.14	1.71	0.00	0.48	3.36	13.12	10.65	2.08
800	0.00	1.21	9.95	6.76	0.00	0.48	5.56	16.03	14.38	2.08
700	0.00	1.21	11.87	11.20	0.77	2.52	12.48	16.03	22.91	3.20
600	1.58	1.21	20.60	19.12	8.64	15.32	28.89	25.85	37.94	5.88
500	12.67	6.27	28.13	25.13	17.48	40.11	42.12	63.37	61.57	12.66
400	42.77	32.60	79.56	94.42	36.20	127.15	78.82	116.41	111.18	56.15
300	111.03	124.60	230.33	267.07	126.91	543.59	227.02	265.65	276.85	137.27
200	646.10	533.35	791.35	1223.66	648.51	2759.45	913.65	1074.41	1106.84	720.59
100	8025.85	5717.97	7401.59	12344.13	7422.30	21429.98	8200.87	8063.68	11110.18	8517.97
90	11733.66	8110.41	10245.01	17536.28	10956.63	27241.12	11102.82	10857.64	16042.86	12409.95
80	16814.31	12381.72	15404.99	25448.23	17150.28	36004.70	16354.38	15284.82	23619.33	18586.09
70	26553.40	20893.30	23767.37	38152.54	28409.48	47946.45	24570.61	21535.06	36837.43	28324.96
60	42982.32	37497.59	38459.80	61498.62	51063.10	67044.78	38205.84	34401.29	59044.36	45709.24
50	64779.02	70708.22	64806.25	105014.25	97941.01	94034.27	63636.80	56600.92	99783.24	74185.63
40	94518.50	143388.17	104422.72	185442.91	185662.14	138091.99	110054.63	104178.79	172091.56	107266.56
30	130255.35	283511.77	151493.82	319556.21	341524.35	206288.75	207575.35	189263.02	299327.31	138073.25
20	167144.22	525641.40	187750.65	496568.23	521570.24	307245.21	381413.42	311718.57	503144.44	162354.81
10	182644.19	960793.61	215970.99	635343.06	658370.11	471522.08	628698.43	452258.26	828455.40	206256.73

A-1-9a: XRF analyses of pumice clasts. Major elements calculated to water-free base.

		SE1a	SE1b	SE1c	SE1d	SE1e	SE1f	SE1g	SE1h	SE1i
SiO_2	wt%	70.15	70.59	70.90	71.10	71.35	71.46	71.58	71.47	71.40
TiO_2	wt%	0.45	0.43	0.41	0.41	0.40	0.39	0.41	0.39	0.39
AL_2O_3	wt%	14.73	14.62	14.55	14.41	14.37	14.32	14.25	14.38	14.35
Fe_2O_3	wt%	3.31	3.17	3.00	3.01	2.91	2.92	2.98	2.84	2.90
MnO	wt%	0.09	0.08	0.08	0.08	0.08	0.08	0.08	0.07	0.07
MgO	wt%	0.83	0.74	0.73	0.71	0.69	0.65	0.66	0.62	0.66
CaO	wt%	2.38	2.20	2.11	2.08	1.96	1.92	1.83	1.90	2.01
Na_2O	wt%	4.79	4.85	4.87	4.79	4.82	4.82	4.76	4.88	4.76
K_2O	wt%	3.03	3.10	3.12	3.17	3.17	3.23	3.24	3.22	3.22
P_2O_5	wt%	0.09	0.08	0.09	0.09	0.08	0.08	0.08	0.08	0.08
H_2O	wt%	3.51	3.49	3.5	3.54	3.59	3.71	3.7	3.79	3.82
CO_2	wt%	0.04	0	0.02	0.04	0.02	0.01	0	0.01	0.12
Co	ppm	6	7	6	5	4	6	5	6	6
Cr	ppm	<18	<18	<18	<18	<18	<18	<18	<18	<18
Ni	ppm	<2	<2	7	<2	<2	<2	<2	<2	<2
V	ppm	34	32	21	22	23	24	21	20	19
Zn	ppm	50	51	51	51	52	48	51	47	46
Ce	ppm	65	56	52	56	54	73	80	43	58
La	ppm	<14	22	<14	<14	20	<14	<14	<14	<14
Nb	ppm	9	9	11	11	10	12	11	11	14
Ga	ppm	18	13	16	19	14	15	13	17	17
Pb	ppm	13	16	19	17	16	15	10	21	18
Pr	ppm	<4	6	<4	10	6	<4	10	<4	<4
Rb	ppm	100	101	102	104	106	106	107	105	105
Ba	ppm	538	536	540	516	541	516	534	512	520
Sr	ppm	110	99	97	92	91	87	85	87	86
Th	ppm	15	14	14	18	13	21	10	20	19
Y	ppm	42	43	43	44	44	45	45	45	45
Zr	ppm	287	294	292	298	305	300	310	304	308

A-1-9b: XRF analyses of andesitic scoria clasts. Major elements calculated to water-free base.

		SE1e m.s	SE1g m.s	SE1h m.s	SE1i m.s	SE1j m.s
SiO_2	**wt%**	56.06	59.17	58.15	56.56	56.42
TiO_2	**wt%**	0.76	0.82	0.82	0.83	0.83
AL_2O_3	**wt%**	17.86	16.90	17.12	17.22	17.26
Fe_2O_3	**wt%**	8.17	7.68	7.94	8.56	8.53
MnO	**wt%**	0.14	0.14	0.14	0.14	0.14
MgO	**wt%**	4.25	2.97	3.33	3.88	3.95
CaO	**wt%**	7.92	6.48	6.94	7.67	7.78
Na_2O	**wt%**	3.32	3.91	3.79	3.53	3.49
K_2O	**wt%**	1.27	1.65	1.52	1.34	1.32
P_2O_5	**wt%**	0.12	0.13	0.13	0.12	0.12
H_2O	**wt%**	1.26	1.69	1.65	1.41	1.39
CO_2	**wt%**	0.03	0.02	0.01	0.01	0.02
Co	**ppm**	26.00	16.00	20.00	24.00	24.00
Cr	**ppm**	<18	<18	<18	<18	<18
Ni	**ppm**	5.00	<2	<2	<2	<2
V	**ppm**	201.00	189.00	197.00	226.00	231.00
Zn	**ppm**	67.00	67.00	74.00	71.00	67.00
Ce	**ppm**	31.00	20.00	42.00	35.00	34.00
La	**ppm**	<14	<14	<14	<14	<14
Nb	**ppm**	5.00	8.00	9.00	7.00	7.00
Ga	**ppm**	19.00	16.00	17.00	15.00	20.00
Pb	**ppm**	11.00	7.00	10.00	5.00	11.00
Pr	**ppm**	<4	<4	<4	<4	<4
Rb	**ppm**	35.00	52.00	47.00	40.00	41.00
Ba	**ppm**	335.00	411.00	365.00	352.00	366.00
Sr	**ppm**	243.00	221.00	230.00	239.00	236.00
Th	**ppm**	6.00	8.00	9.00	8.00	7.00
Y	**ppm**	25.00	30.00	28.00	24.00	27.00
Zr	**ppm**	109.00	142.00	129.00	114.00	112.00

A-2 Laacher See eruption

Field descriptions
Maximum clast size
Median and sorting coefficient
Modal composition
Density
Shape parameter
Chemistry

A-2-1: Field descriptions, preliminary modal analyses and samples taken of the LST section in the Nickenich pit.

LLST Fallout

Sequence begins in the deepest part of the pit, next to the little pool with the uppermost fallout of the LLST. It is easily to identify because of the prominent slate enriched layer at the top (LLSTe). A fine bedded, dark gray clay lies below the fallout sequence of LLST, which has a 5 cm, brown-gray hardened top, possibly baked by the overlying hot fallout. The LLST was separated by grain-size and modal characteristic in 6 beds, labeled LLSTa to LLSTf. The pumice clasts are subangular to angular in the medium-coarse lapilli size range and the fine ones rounded to subrounded. Modal composition of the pumice clasts clearly predominated by tube pumice from LLSTb on and from LLSTc on minor (>1%) banded pumice occur, increasing in abundance toward the top. Pumice with round to ovoid bubbles are virtually absent and occur occasionally.

LLSTa

A 9 cm fine, light brown lapilli bed. It is water saturated and it was necessary to dig down to the clay bed below LLST to sample it. Modal description and maximum clast size determination were not possible.

Samples: NU01-45 (bulk sample)

LLSTb

A 43 cm thick brownish fine lapilli bed with minor medium to coarse lapilli. The major pumice type is tube pumice both in fine and in medium to coarse lapilli size-range. Lithic clasts make up less than 1% of the deposit. Maximum clast sizes are 4.6 cm for pumice and 3.7 cm for lithics.

Samples: NU01-44 (bulk sample)

LLSTc

A 52 cm thick, white fine lapilli bed with medium to coarse lapilli. Major pumice type is also tube pumice in all size ranges. Minor banded pumice (<1%) occurs from this bed on up to the top of the entire LLST fallout. Lithics make up <5% of the deposit. Maximum clast sizes are 6.4 cm for pumice and 7.2 cm for lithics.

Samples: NU01-43 (bulk sample)

LLSTd

A 6 cm thick, white fine to medium lapilli bed with coarse lapilli. The bed is quite diffuse and in part hardly to recognize in the deposit, but the conspicuous change in grain-size led to a differentiation of this bed. Pumice clasts are dominated by tube pumice. Maximum clast sizes are 4.3 cm for pumice and 4.2 cm for lithics.

Samples: NU01-42 (bulk sample)

LLSTe

A 30 cm thick white fine to medium lapilli bed with minor coarse lapilli. The dominating pumice type is tube pumice (as below). Lithics make up ~5% of the deposit. Maximum clast sizes are 4.2 cm for pumice and 5.2 cm for lithics.

Samples: NU01-41 (bulk sample)

LLSTf

The 15 cm thick, very marking Double Devonian slate layer, finishing the LLST fallout sequence. It is white-black and enriched in lithic clasts (40-50%), mainly slate. The pumice clasts are predominated by tube pumice. Maximum clast sizes are 5.7 cm for pumice and 6.3 cm for lithics.

Samples: NU01-40 (bulk sample)

Hauptbritzbank (Main Britzbank; HBB) and associated fallout deposits

The LLST fallout is followed by the Hauptbritzbank (HBB, a series of fine-coarse grained intercalations, HBB-IV), which is ending in a thick valley-filling ignimbrite (Trass, HBB-III), topped by two thin fallout layers (HBB-I/II), enriched in accretionary lapilli (Schmincke pers. comm.).

HBB-IV (MLST A)

Is a144 cm thick sequence of interbedded brown ashy and medium to coarse pumice lapilli beds. No samples were taken.

HBB-III (MLST B)

An up to 5 m thick, light brown ignimbrite with pockets enriched in Pumice and lithic clasts. Further degassing pipes were observed in the deposit. No flow units were distinguished in the field.

Samples: NU01-46 (pumice clasts of the upper 2.1 m of the ignimbrite)

HBB-II

A 4 cm thick fine to medium lapilli bed, with about 5% lithic clasts. Maximum clast size was estimatetd roughly to be ~3.5 cm for pumice and ~3 cm for lithics.

Samples: NU01-39 (bulk sample)

HBB-I

A 6 cm, light brown ashy bed, with accretionary lapilli. No sample taken.

Upper Britzbank (Obere Britzbank - OBB) and associated fallout deposits

The HBB is overlain by a 55 cm thick fallout deposit (OBB-D/E), enriched in lithics at the lowermost 14 cm. The following Upper Britzbank (OBB-A to C) is a double layer of fine-grained (ashy) beds (OBB-A/C), separated by a 2 cm lapilli layer (OBB-B). The entire sequence was labeled as OBB-A to OBB-E starting, with E at the base.

OBB-E

The 14 cm thick, lithic-rich base layer of an fallout bed between the HBB and OBB. The pumice clasts are angular to subrounded and have predominantly round to ovoid bubbles (T1) and only 10% tube pumice. Bombs are very rare. Lithic fragments make up about 40% of the deposit and are mainly slate and lava fragments. Maximum clast sizes are 7.5 cm for pumice and 7.5 cm for lithic clasts.

Samples: NU01-38 (bulk sample)

OBB-D

A 41 cm thick, white bed of medium to coarse lapilli with high content of fine lapilli in interstitial space. Pumice clasts are angular to subrounded and have predominantly round to ovoid bubbles (T1) and only 10% tube pumice. Bombs are very rare. Lithic are less abundant than in OBB-E and make up only 5-10% and are predominantly slate. Maximum clast sizes are 8.5 cm and 8.4 cm for lithics.

Samples: NU01-37 (bulk sample)

OBB-C

A 17 cm thick, brown ash bed, with minor pumice clasts. No samples were taken out of this Britzbank.

OBB-B

A 3 cm thick medium lapilli bed. The pumice clasts are angular to subangular and abundant tube pumice in the medium lapilli size range. The fine lapilli are predominantly rounded to subrounded. The lithic clasts make up less than 5% of the deposit. Maximum clast sizes are 6.6 cm for pumice and 4.1 cm for lithics.

Samples: NU01-36 (bulk sample)

OBB-A

An 8 cm thick, brown ash bed, with minor pumice clasts. No samples were taken out of this Britzbank.

Fallout Sequence above OBB (MLST B/C)

Above the UBB the main fallout sequence of the MLST is cropping out at all the walls around the pit. The sequence itself was separated in distinct beds, by grain-size, modal, pumice population and color characteristics, determined in the field, and easily applicable to other locations. So it should be possible to correlate the different fallout beds over the three different facies types, described by (Bogaard and Schmincke, 1984). In the upper part of the fallout section three, up to 3 m thick, ignimbrites are intercalated, their distribution is confined to palaeovalleys and they are wedging out in the outcrop.

The main fallout sequence above UBB is separated in 10 distinguishable beds, which were labeled by roman numbers I to X. They are easily distinguishable by color and average grain-size and fines content. The beds are consistently cropping out at all walls of the pit.

Field layer I:

A 55 cm thick, dirty white, medium to coarse lapilli bed with high interstitial fine lapilli content. the maximum clasts (bomb sized) are enriched in the basal 9 cm. The medium to coarse lapilli are mainly angular to subangular pumice with round to ovoid bubbles, while the fine ones are rounded to subrounded.. Pumice with elongated bubbles and banded pumice was only observed in bomb size range. The lithics make up less than 10% of the deposit and are mainly slate clasts. Maximum Clast sizes are 9.3 cm for pumice and 5.5 cm for lithic clasts.

Samples: NU01-23 (bulk sample) and NU01-24 (bombs)

Field layer II

This about 5-6 cm thick bed mainly consists of fine lapilli to coarse ash and is therefore brownish in color. The rarely occurring larger, white pumice clasts (medium/coarse lapilli) are angular to subangular in contrast to the subrounded fine lapilli. No banded pumice was observed in the bed. Lithic clasts make up less than 10% and are dominated by slate clasts in fine lapilli size. Maximum clast sizes are 3.2 cm for pumice and 1.8 cm for lithics.

Samples: NU01-25 (bulk sample)

Field layer III

An about 12 to 13 cm thick, white bed of medium to coarse lapilli with an upward increase of fine lapilli. The medium to coarse lapilli are enriched in the lower 10 cm while the fine lapilli are enriched in the upper 2 cm. The majority (~99%) of the pumices are angular to subangular of two types (T1 and T2), with angular to subangular clasts, round bubbles in the first and angular clasts, ovoid to elongated bubbles in the second type. Only about <1 % of the pumices are banded/mixed pumice. The lithic fragments make up 10-20% of the deposit and are mainly slate clasts. Maximum clast sizes are 8.8 cm for pumice and 7.2 cm for lithics.

Samples: NU01-26 (bombs); NU01-27 (bulk sample)

Field layer IV

A 14 cm thick, brownish layer of medium lapilli enriched in fine lapilli and ash. The basal 4 cm is both enriched in ash and shows a band of medium lapilli. The bed is well cemented. Pumice clasts of medium to coarse lapilli size are mainly white, angular to subangular, round to ovoid bubbles. Tube pumice occurs also in this size range and make up about 20 % of the deposit. Fine lapilli are rounded to subrounded. Lithics are less enriched in this bed and make up <5%, with mainly slate. Maximum clasts sizes are 6.5 cm for pumice and 5.1 cm for lithics.

Samples: NU01-28 (bulk sample)

Field layer V

This about 29 cm thick, white bed consists of coarse lapilli with an high content of fine lapilli in the interstitial space. The coarse pumice lapilli are mainly angular to subangular and have round to ovoid bubbles. About 20-30% are tube pumice and minor (<5%) banded pumice. The fine pumice lapilli are subangular to subrounded, but also rounded pumice occur. Few dense gray clasts were observed in the deposit (<<1%). Lithics constitute about 5-10 % of the deposit and are mainly slate and lava clasts. Maximum clast sizes are 13.7 cm for pumice and 10.5 for lithics.

Samples: NU01-29 (bombs); NU01-30 (bulk sample)

Field layer VI (MLST C)

A 18-19 cm thick, brownish bed of medium to minor coarse lapilli with fine lapilli in interstitial space. The medium lapilli are angular to subangular and mainly (>>50%) have round to ovoid bubbles, 20-30% are tube pumices, 10% banded pumice and 1-5% dense gray pumice. The fine lapilli are subrounded to subangular and also minor dense gray pumice occur in this size range. The lithic clasts make up about 5% and are mainly slate and lava fragments. Maximum clast sizes are 12.7 cm for pumice and 7.9 cm for lithics.

Samples: NU01-31 (bulk sample)

Field layer VII

An about 9 cm thick, white medium to coarse lapilli bed with increasing content of fine lapilli in the upper 2-3 cm. The medium lapilli are mainly angular to subangular, with round to ovoid bubbles (70-80%), tube pumice (10-20%), banded pumice (5-10%) and occasional dense gray (<1%). The coarse lapilli and bombs are in contrast subrounded to subangular (broken clasts) and the majority (90-100%) have round to ovoid bubbles and only about <10% are tube and banded pumice. Lithic make up about 5% of the deposit and are mainly slate and lava clasts. Maximum clast sizes are 15.6 cm for pumice and 7.1 cm for lithics.

Samples: NU01-32 (bulk sample)

Field layer VIII

An about 9 cm thick, brownish white bed of fine to medium lapilli with few coarse lapilli and bombs. The fine an medium lapilli are subangular to subrounded and few broken angular clasts, 90% have round to ovoid bubbles, 5% tube pumice and <5% banded and dense gray pumice. The coarse lapilli and bombs are in contrast angular to subangular, with minor coliform bombs, 70-80% with round to ovoid bubbles, <10% tube pumice, 10-20% banded pumice and denser pumice of T2 and no dense gray pumice. The lithic content of this bed is higher than in previous below, with 10-20%, mainly slate and lava clasts. Maximum clasts sizes are 7.4 cm for pumice and 5.6 cm for lithics.

Samples: NU01-33 (bulk sample)

Field layer IX

A 10 cm thick bed of medium to coarse lapilli, with minor fine lapilli in interstitial space, increasing upward. The medium to coarse lapilli are subangular to subrounded. Pumice clasts of T1 and T2 with round to ovoid bubbles makes up 80-90% of the pumice population (T1:T2=3:1), tube pumice, banded pumices and dense gray pumice make up only <5% respectively. Fine lapilli are mainly subrounded. The lithic clasts constitute about 5% and are dominated by slate and lava fragments. Maximum clast sizes are 10.7 cm for pumice and 7.9 cm for lithics.

Samples: NU01-34 (bulk sample)

Field layer X

A 9 cm thick medium to coarse lapilli bed rich in fine lapilli. Except the increased amount of fine lapilli in the interstitial space the modal composition of this layer is comparable to that of Layer IX. Maximum clast sizes decrease to 6.4 cm for pumice and 3.8 cm for lithics.

Samples: NU01-35 (bulk sample)

MLST C3

The overlying MLST C3 is a very characteristic, widespread fallout layer (55 cm thick) of the MLST, being extremely enriched in dense gray pumice clasts. Determination of the modal composition in the outcrop showed that the deposit itself is separated in two distinct beds (Tab1):

- the lower 12 cm of the C3 fall deposit are more fine-grained (medium to coarse lapilli, ~3-4 cm) than the upper part, less lithic clasts and dense gray/banded pumice.
- the main part of C3 to ~50% constitutes of gray/banded, dense pumice clasts (coarse lapilli, ~4-5 cm)and about 10% of lithic clasts.

In the field four different pumice types were distinguished by color, bubble shape, vesicularity and clast shape:

1. banded, gray-white, vesicles <40vol%, round (<1 mm), elongated to round (>2 mm), subrounded to subangular, irregular shape/surfaces, XX <5%

2. white, vesicles >50%, round (<1 mm) elongated to ovoid (>3 mm), subangular, XX <<5%
3. white, vesicles <50%, round (<1 mm), round-ovoid (>2 mm), angular, XX <5%
4. gray-greenish, vesicles <10% to vesicle free, angular, XX 5-10%, bread-crust surfaces observed

Table 1: Variation of modal composition of essential pumice clasts in C3				
Stratigraphic Position	Pumice Type 1	Pumice Type 2	Pumice Type 3	Pumice Type 4
Main C3	11.9 %	16.9 %	27.1 %	44.1 %
Lowermost 12 cm	3.0 %	33.3%	42.4 %	21.2 %

The modal composition of the lithic clasts in the deposit was also determined in the outcrop and are slate (22.6%), sandy slate (22.6%), sandstone (29%), mafic lava (12.9%), mafic scoria (9.7%) and contact metamorphites (3.2%).
The maximum clast-sizes are in average 14.2 cm for pumice and 8.7 cm for lithic clasts.

Samples: NU01-18 to NU01-22, NU01-21 and NU01-22 (bulk samples)

Flow I

An up to 120 cm thick ignimbrite cropping out only in few places of the pit (Location of section 1 is missing now) lacking visible flow units. The ignimbrite forms a valley filling and is wedging out very quick, also in the section 1 locality.

Samples: NU01-50 pumice clasts of lower 20 cm

Transitional C3 (field layer (7))

This 14 cm thick layer is maybe the transitional part of C3, marking the change of the depositional characteristics from C3 to the overlying bedded fallout sequence between the two ash flows (flow I and II). It is lying on top of the flow I, where this was deposited, but the differences in structure are also obvious at parts of the outcrop where flow I is not present. The most significant difference between C3 and (7) is the increasing amount of fine lapilli (0.5-1 cm), in the space between the essential, coarse lapilli (4-5 cm) population. Next to this grain-size criteria the amount of lithic clasts is decreasing to 5-10%.
In the field three different pumice types were distinguished and counted:

1. gray-greenish (in part banded), vesicles ~5%, angular to subangular, in part irregular surfaces (47.6%)
2. white, vesicles >50%, round (<1 mm) elongated to ovoid (>3 mm), subrounded to subangular, irregular shapes (14.3%)
3. white, vesicles >50%, round (<1 mm), round-ovoid (>2 mm), subangular to angular (38.1%)

The modal composition of the lithic clasts: slate (33.3%), sandy slate (5.6%), sandstone (22.2%), mafic lava (27.8%), mafic scoria (11.1%) and contact metamorphites (0%).
The maximum clast size is 8.8 cm for pumice and 3.2 cm for lithics.

Samples: NU01-14 (bulk slample), NU01-15 (single clasts)

A-2-2a: Maximum pumice clast size variation of the Nickenich pit.

Stratigraphic position	Max. pumice					Average	Stddev.
M-LST C3 top	9.5	8.0	8.5	9.0		8.75	0.65
M-LST C3 main part	13.5	12.5	14.0	14.5	16.5	14.20	1.48
X	6.8	5.0	7.7	6.4	6.0	6.38	1.00
IX	9.9	8.4	16.0	10.5	8.9	10.74	3.05
VIII	8.6	8.9	7.4	6.4	5.7	7.40	1.38
VII	8.6	8.9	7.4	6.4	5.7	7.40	1.38
VI	18.0	14.3	12.1	9.3	9.8	12.70	3.57
V	14.0	11.7	12.4	17.5	12.8	13.68	2.29
IV	5.0	6.8	7.8	6.4	6.5	6.50	1.00
III	8.0	7.9	7.1	11.1	9.2	8.66	1.56
II	3.2	3.2	3.0	3.1	3.6	3.22	0.23
I	7.0	10.0	9.7	10.5	9.5	9.34	1.36
OBB-B	10.0	4.0	3.9	8.5	6.5	6.58	2.70
OBB-D	12.5	7.5	8.0	7.8	6.5	8.46	2.33
OBB-E	8.3	7.4	7.7	7.9	6.2	7.50	0.80
L-LST f	5.1	11.9	3.4	3.7	4.3	5.68	3.54
L-LST e	3.7	3.8	4.0	4.7	4.7	4.18	0.49
L-LST d	4.5	4.4	4.3	3.9	4.3	4.28	0.23
L-LST c	8.0	6.8	6.7	5.2	5.5	6.44	1.12
L-LST b	5.2	4.5	3.9	5.1	4.4	4.62	0.54
L-LST a	0.0	0.0	0.0	0.0	0.0	0.00	0.00

A-2-2b: Maximum lithic clast size variation of the Nickenich pit.

Stratigraphic position	Max lithic					Average	Std Dev
M-LST C3 top	3,0	2,8	4,2	2,7		3,18	0,69
M-LST C3 main part	8,2	7,6	8,5	12,0	7,0	8,66	1,95
X	3,3	4,4	3,6			3,77	0,57
IX	7,9	7,5	7,2			7,53	0,35
VIII	6,2	5,5	5,0			5,57	0,60
VII	5,9	5,8	5,7	10,8		7,05	2,50
VI	9,8	7,1	6,8			7,90	1,65
V	10,5	9,0	12,0			10,50	1,50
IV	5,6	4,6	5,4	4,9		5,13	0,46
III	6,2	6,6	8,8			7,20	1,40
II	1,5	1,8	2,1			1,80	0,30
I	6,5	3,9	6,5			5,63	1,50
OBB-B	3,7	4,0	4,6			4,10	0,46
OBB-D	7,1	8,4	9,6			8,37	1,25
OBB-E	6,7	8,9	6,9			7,50	1,22
L-LST f	5,9	6,1	7,0			6,33	0,59
L-LST e	6,8	4,7	4,7			5,40	1,21
L-LST d	4,0	3,1	5,6			4,23	1,27
L-LST c	6,4	10,5	4,7			7,20	2,98
L-LST b	3,4	4,4	3,2			3,67	0,64
L-LST a	0,0	0,0	0,0	0,0	0,0	0,00	0,00

A-2-3: Grain size distribution of the samples taken in the Nickenich Pit.

Sample Number	Φ -5	Φ -4	Φ -3	Φ -2	Φ -1	Φ 0	Φ 1	Φ 2	Φ 3	Φ 4	Φ 5
NU01-14	9,01	25,73	32,71	20,34	8,34	2,07	0,84	0,21	0,10	0,06	0,58
NU01-21	2,46	41,47	27,10	13,08	3,12	0,93	0,56	0,32	0,21	0,15	10,60
NU01-22	2,81	23,35	43,40	21,96	5,47	1,01	0,42	0,26	0,20	0,13	1,00
NU01-35	2,90	11,11	27,22	30,79	18,48	5,57	0,83	0,28	0,20	0,14	2,48
NU01-34	0,00	13,84	31,36	30,53	15,27	3,04	2,30	0,25	0,64	0,01	2,78
NU01-33	0,00	7,34	27,77	27,80	21,81	9,52	2,55	0,37	0,22	0,15	2,46
NU01-32	2,81	26,52	36,34	19,45	7,92	3,57	1,27	0,27	0,18	0,13	1,54
NU01-31	0,00	18,45	32,27	24,11	15,14	5,80	1,49	0,32	0,22	0,16	2,05
NU01-30	0,00	14,58	40,35	25,92	11,40	3,97	1,02	0,43	0,13	0,00	2,20
NU01-28	1,27	10,74	23,07	24,30	18,51	9,97	4,28	0,83	0,72	0,65	5,66
NU01-27	0,00	11,43	31,70	30,09	16,38	6,38	1,61	0,29	0,22	0,16	1,74
NU01-25	0,00	1,15	22,54	30,88	21,97	13,66	5,48	0,62	0,47	0,42	2,81
NU01-23	0,00	18,13	23,47	25,07	18,27	8,20	2,78	0,44	0,30	0,25	3,11
NU01-36	0,00	12,25	24,99	24,29	12,15	6,83	3,10	1,79	1,67	1,17	11,75
NU01-37	2,65	6,28	25,67	28,55	19,15	9,60	3,41	0,62	0,28	0,19	3,61
NU01-38	2,16	27,73	29,75	24,94	8,40	2,66	1,27	0,68	0,35	0,21	1,85
NU01-40	0,00	13,41	42,14	30,71	9,82	1,62	0,54	0,35	0,17	0,09	1,14
NU01-41	0,00	4,71	23,08	30,14	22,57	9,15	5,05	0,59	0,14	0,09	4,48
NU01-42	0,00	9,55	24,68	28,23	20,32	10,41	3,29	0,54	0,18	0,11	2,68
NU01-43	0,00	4,32	18,23	16,74	26,49	16,25	5,72	0,91	0,24	0,15	10,95
NU01-44	1,35	2,97	15,62	24,76	26,63	17,76	6,77	1,12	0,17	0,11	2,74
NU01-45	0,00	1,95	10,96	23,13	25,93	17,84	8,16	2,88	2,27	1,03	5,85

A-2-4a: Median and sorting coefficient of complete GSD.

Sample No.	Φ %16	Md Φ	Φ %84	Sorting coefficient
NU01-14	-4,70	-3,60	-2,30	1,20
NU01-21	-4,70	-3,80	-2,10	1,30
NU01-22	-4,40	-3,50	-2,45	0,98
NU01-35	-4,00	-2,70	-1,40	1,30
NU01-34	-4,00	-2,90	-1,60	1,20
NU01-33	-3,65	-2,50	-1,10	1,28
NU01-32	-4,50	-3,45	-2,10	1,20
NU01-31	-4,10	-3,00	-1,50	1,30
NU01-30	-3,95	-3,15	-1,80	1,08
NU01-28	-3,80	-2,45	-0,50	1,65
NU01-27	-3,80	-2,80	-1,50	1,15
NU01-25	-3,30	-2,20	-0,60	1,35
NU01-23	-4,10	-2,65	-1,10	1,50
NU01-36	-3,80	-2,50	1,15	2,48
NU01-37	-3,70	-2,50	-0,85	1,43
NU01-38	-4,50	-3,30	-2,05	1,23
NU01-40	-3,90	-3,15	-2,15	0,88
NU01-41	-3,45	-2,30	-0,80	1,33
NU01-42	-3,70	-2,50	-0,95	1,38
NU01-43	-3,35	-1,60	0,20	1,78
NU01-44	-3,20	-1,80	-0,40	1,40
NU01-45	-2,85	-1,50	0,40	1,63

A-2-4b: Median and sorting coefficient of pumice GSD.

Sample No.	Φ %16	Md Φ	Φ %84	Sorting coefficient
NU01-14	-4,75	-3,55	-2,20	1,28
NU01-21	-4,80	-4,10	-2,60	1,10
NU01-22	-4,45	-3,40	-2,40	1,03
NU01-35	-3,90	-2,60	-1,50	1,20
NU01-34	-3,80	-2,70	-1,65	1,08
NU01-33	-3,50	-2,30	-1,10	1,20
NU01-32	-4,50	-3,30	-2,00	1,25
NU01-31	-4,10	-2,80	-1,50	1,30
NU01-30	-4,00	-2,90	-1,80	1,10
NU01-28	-3,50	-2,30	-0,85	1,33
NU01-27	-3,80	-2,60	-1,45	1,18
NU01-25	-3,15	-2,10	-0,70	1,23
NU01-23	-3,90	-2,50	-1,20	1,35
NU01-36	-3,85	-2,60	1,10	2,48
NU01-37	-3,55	-2,35	-1,00	1,28
NU01-38	-4,30	-2,80	-1,90	1,20
NU01-40	-3,50	-2,60	-1,90	0,80
NU01-41	-3,20	-2,20	-0,95	1,13
NU01-42	-3,45	-2,30	-1,00	1,23
NU01-43	-3,15	-1,65	-0,50	1,33
NU01-44	-3,10	-1,80	-0,80	1,15
NU01-45	-2,75	-1,60	-0,20	1,28

A-2-5: Modal composition of essential lapilli size range of the samples taken at Nickenich pit.

Sample No.	Type 1	Type 2	Type 3	Type 4	Type 5	other types	lithics
NU01-14	22.35	16.70	18.13	37.81	0.00	0.00	5.01
NU01-21	16.47	11.44	15.85	43.68	0.00	0.00	12.55
NU01-22	27.69	21.06	20.45	17.17	0.00	5.48	8.15
NU01-35	20.96	27.65	34.39	0.00	0.00	0.00	17.00
NU01-34	38.12	26.96	5.42	3.35	0.77	0.00	25.38
NU01-33	30.47	18.86	25.33	10.21	0.00	0.00	15.13
NU01-32	29.07	23.19	12.23	0.00	8.02	0.00	27.48
NU01-31	30.74	22.62	14.26	3.49	4.73	0.00	24.15
NU01-30	42.58	27.18	5.69	7.07	3.62	0.00	13.86
NU01-28	25.74	13.37	0.00	0.00	4.42	0.00	56.47
NU01-27	33.65	28.87	13.48	0.00	7.42	0.00	16.57
NU01-25	100.00	0.00	0.00	0.00	0.00	0.00	0.00
NU01-23	30.13	26.67	9.23	0.00	0.85	0.00	33.11
NU01-36	50.94	30.46	0.00	0.00	0.00	0.00	18.59
NU01-37	41.36	18.20	1.80	0.00	15.73	0.00	22.91
NU01-38	17.20	18.00	3.32	0.00	5.42	0.00	56.07
NU01-40	5.34	0.00	6.34	4.41	11.94	0.00	71.97
NU01-41	19.96	0.00	18.40	0.00	28.15	0.00	33.49
NU01-42	21.92	8.96	0.00	0.00	23.00	0.00	46.12
NU01-43	19.05	9.02	2.23	0.00	29.65	0.00	40.05
NU01-44	27.31	0.00	5.34	0.00	67.35	0.00	0.00
NU01-45	55.48	0.00	0.00	0.00	44.52	0.00	0.00

A-2-6a: Density of all pumice type 1 clasts analyzed.

Sample number	Density av. (kg/m³)	Stddev. (kg/m³)
NU01-14(T1), >32 mm I	368,52	12,84
NU01-14(T1), >32 mm II	486,87	11,73
NU01-14(T1), 32-16 mm I	734,45	67,47
NU01-14(T1), 32-16 mm II	391,94	4,86
NU01-14(T1), 32-16 mm III	364,06	6,64
NU01-14(T1), 32-16 mm IV	335,75	1,11
NU01-14(T1), 32-16 mm V	335,28	1,06
NU01-14(T1), 32-16 mm VI	319,70	5,93
NU01-14(T1), 32-16 mm VII	379,54	3,36
NU01-14(T1), 32-16 mm VIII	279,21	2,50
NU01-14(T1), 32-16 mm IX	409,10	4,22
NU01-14(T1), 32-16 mm X	326,00	2,51
NU01-21(T1), >32 mm	432,69	10,32
NU01-21(T1), 32-16 mm I	599,42	27,66
NU01-21(T1), 32-16 mm II	330,17	4,91
NU01-21(T1), 32-16 mm III	352,23	2,80
NU01-21(T1), 32-16 mm IV	408,59	2,77
NU01-21(T1), 32-16 mm V	448,61	2,16
NU01-21(T1), 32-16 mm VI	369,91	4,65
NU01-21(T1), 32-16 mm VII	369,06	7,00
NU01-21(T1), 32-16 mm VIII	357,48	6,16
NU01-21(T1), 32-16 mm IX	502,93	6,67
NU01-21(T1), 32-16 mm X	367,33	6,43
NU01-22(T1), 32-16 mm I	432,35	21,73
NU01-22(T1), 32-16 mm II	309,05	3,46
NU01-22(T1), 32-16 mm III	298,32	1,43
NU01-22(T1), 32-16 mm IV	345,53	7,88
NU01-22(T1), 32-16 mm V	298,33	2,75
NU01-22(T1), 32-16 mm VI	327,17	5,12
NU01-22(T1), 32-16 mm VII	315,19	5,35
NU01-22(T1), 32-16 mm VIII	336,63	3,57
NU01-22(T1), 32-16 mm IX	318,83	2,08
NU01-35(T1), 32-16 mm I	333,13	5,96
NU01-35(T1), 32-16 mm II	345,83	1,78
NU01-35(T1), 32-16 mm III	382,21	74,04
NU01-35(T1), 32-16 mm IV	392,24	8,20
NU01-35(T1), 32-16 mm V	381,16	4,54
NU01-35(T1), 32-16 mm VI	345,26	6,29

A-2-6b: Density of all pumice type 1 clasts analyzed.

Sample number	Density av. (kg/m³)	Stddev. (kg/m³)
NU01-34(T1), 32-16 mm I	312,81	3,74
NU01-34(T1), 32-16 mm II	412,94	2,17
NU01-34(T1), 32-16 mm III	256,75	4,96
NU01-34(T1), 32-16 mm IV	320,09	5,88
NU01-34(T1), 32-16 mm V	368,65	2,19
NU01-34(T1), 32-16 mm VI	324,93	4,70
NU01-34(T1), 32-16 mm VII	352,50	5,17
NU01-34(T1), 32-16 mm VIII	296,87	1,20
NU01-34(T1), 32-16 mm IX	345,22	5,51
NU01-33(T1), 32-16 mm I	403,26	7,71
NU01-33(T1), 32-16 mm II	256,60	6,88
NU01-33(T1), 32-16 mm III	367,12	6,24
NU01-33(T1), 32-16 mm IV	341,19	2,97
NU01-33(T1), 32-16 mm V	395,53	6,42
NU01-33(T1), 32-16 mm VI	376,44	39,03
NU01-33(T1), 32-16 mm VII	237,24	3,75
NU01-33(T1), 32-16 mm VIII	380,45	4,09
NU01-33(T1), 32-16 mm IX	275,98	3,78
NU01-33(T1), 32-16 mm X	245,80	3,64
NU01-31(T1), 32-16 mm I	292,42	8,68
NU01-31(T1), 32-16 mm II	520,88	9,91
NU01-31(T1), 32-16 mm III	341,01	2,51
NU01-31(T1), 32-16 mm IV	309,80	7,55
NU01-31(T1), 32-16 mm V	325,59	3,12
NU01-31(T1), 32-16 mm VI	323,84	3,87
NU01-31(T1), 32-16 mm VII	301,58	3,39
NU01-31(T1), 32-16 mm VIII	313,12	6,46
NU01-31(T1), 32-16 mm IX	303,15	5,59
NU01-31(T1), 32-16 mm X	297,40	5,86
NU01-30(T1), 32-16 mm I	426,09	4,99
NU01-30(T1), 32-16 mm II	249,96	3,77
NU01-30(T1), 32-16 mm III	364,75	2,20
NU01-30(T1), 32-16 mm IV	392,92	5,49
NU01-30(T1), 32-16 mm V	262,80	2,50
NU01-30(T1), 32-16 mm VI	386,84	15,94
NU01-30(T1), 32-16 mm VII	451,97	5,13
NU01-30(T1), 32-16 mm VIII	436,71	9,11
NU01-30(T1), 32-16 mm IX	396,88	6,13
NU01-30(T1), 32-16 mm X	262,09	8,39

A-2-6c: Density of all pumice type 1 clasts analyzed.

Sample number	Density av. (kg/m³)	Stddev. (kg/m³)
NU01-28(T1), 32-16 mm I	329,60	6,32
NU01-28(T1), 32-16 mm II	338,75	3,92
NU01-28(T1), 32-16 mm III	269,86	3,29
NU01-28(T1), 32-16 mm IV	321,91	5,95
NU01-28(T1), 32-16 mm V	267,45	5,32
NU01-28(T1), 32-16 mm VI	342,79	5,63
NU01-28(T1), 32-16 mm VII	280,12	10,39
NU01-28(T1), 32-16 mm VIII	289,35	3,75
NU01-28(T1), 32-16 mm IX	359,79	3,66
NU01-28(T1), 32-16 mm X	267,18	3,01
NU01-27(T1), 32-16 mm I	364,36	4,90
NU01-27(T1), 32-16 mm II	376,58	4,45
NU01-27(T1), 32-16 mm III	395,19	8,73
NU01-27(T1), 32-16 mm IV	400,75	9,28
NU01-27(T1), 32-16 mm V	327,92	3,60
NU01-27(T1), 32-16 mm VI	360,14	5,43
NU01-27(T1), 32-16 mm VII	346,94	3,82
NU01-27(T1), 32-16 mm VIII	282,30	4,85
NU01-27(T1), 32-16 mm IX	332,34	2,42
NU01-27(T1), 32-16 mm X	315,80	2,45
NU01-25(T1), 32-16 mm I	304,00	3,41
NU01-23(T1), 32-16 mm I	323,97	5,71
NU01-23(T1), 32-16 mm II	307,09	2,49
NU01-23(T1), 32-16 mm III	327,58	6,12
NU01-23(T1), 32-16 mm IV	292,24	5,04
NU01-23(T1), 32-16 mm V	191,74	1,50
NU01-23(T1), 32-16 mm VI	230,94	3,97
NU01-23(T1), 32-16 mm VII	232,06	2,07
NU01-23(T1), 32-16 mm VIII	283,10	4,24
NU01-23(T1), 32-16 mm IX	340,96	3,19
NU01-23(T1), 32-16 mm X	288,26	2,88
NU01-40(T1), 32-16 mm I	344,06	1,88
NU01-40(T1), 32-16 mm II	313,85	5,55
NU01-40(T1), 32-16 mm III	308,31	4,34
NU01-40(T1), 32-16 mm IV	301,97	3,99
NU01-41(T1), 32-16 mm I	312,34	3,62
NU01-41(T1), 32-16 mm II	250,24	1,46
NU01-41(T1), 32-16 mm III	249,62	1,60
NU01-41(T1), 32-16 mm IV	317,21	4,75
NU01-41(T1), 32-16 mm V	323,14	2,54
NU01-41(T1), 32-16 mm VI	336,50	2,66
NU01-41(T1), 32-16 mm VII	332,48	1,99

A-2-6d: Density of all pumice type 1 clasts analyzed.

Sample number	Density av. (kg/m³)	Stddev. (kg/m³)
NU01-42(T1), 32-16 mm I	308.43	4.41
NU01-42(T1), 32-16 mm II	253.57	1.72
NU01-42(T1), 32-16 mm III	295.54	6.46
NU01-42(T1), 32-16 mm IV	264.13	6.24
NU01-42(T1), 32-16 mm V	351.60	3.29
NU01-42(T1), 32-16 mm VI	350.73	4.32
NU01-44(T1), 32-16 mm I	299.44	1.73
NU01-44(T1), 32-16 mm II	264.57	5.46
NU01-44(T1), 32-16 mm III	249.74	2.62
NU01-44(T1), 32-16 mm IV	309.23	1.54
NU01-44(T1), 32-16 mm V	302.81	2.40

A-2-6e: Density of all pumice type 2 clasts analyzed.

Sample number	Density av. (kg/m³)	Stddev. (kg/m³)
NU01-14(T2), >32 mm	949,71	69,98
NU01-14(T2), 32-16 mm I	776,90	56,03
NU01-14(T2), 32-16 mm II	361,04	1,61
NU01-14(T2), 32-16 mm III	465,42	9,43
NU01-14(T2), 32-16 mm IV	1040,87	5,58
NU01-14(T2), 32-16 mm V	361,59	2,28
NU01-14(T2), 32-16 mm VI	391,33	12,35
NU01-14(T2), 32-16 mm VII	372,50	2,35
NU01-14(T2), 32-16 mm VIII	514,59	9,86
NU01-14(T2), 32-16 mm IX	585,88	3,19
NU01-14(T2), 32-16 mm X	430,32	11,12
NU01-21(T2), 32-16 mm I	705,65	43,57
NU01-21(T2), 32-16 mm II	593,54	2,61
NU01-21(T2), 32-16 mm III	327,58	2,07
NU01-21(T2), 32-16 mm IV	434,58	1,35
NU01-21(T2), 32-16 mm V	545,71	8,03
NU01-21(T2), 32-16 mm VI	419,32	3,32
NU01-21(T2), 32-16 mm VII	824,24	3,84
NU01-21(T2), 32-16 mm VIII	566,72	10,48
NU01-21(T2), 32-16 mm IX	459,77	4,49
NU01-21(T2), 32-16 mm X	386,25	5,84

A-2-6f: Density of all pumice type 2 clasts analyzed.

Sample number	Density av. (kg/m³)	Stddev. (kg/m³)
NU01-22(T2), 32-16 mm I	936,69	41,47
NU01-22(T2), 32-16 mm II	532,17	10,45
NU01-22(T2), 32-16 mm III	411,93	1,46
NU01-22(T2), 32-16 mm VI	616,57	8,67
NU01-22(T2), 32-16 mm V	425,52	3,52
NU01-22(T2), 32-16 mm VI	431,73	3,95
NU01-22(T2), 32-16 mm VII	437,27	3,98
NU01-22(T2), 32-16 mm VIII	419,12	7,34
NU01-22(T2), 32-16 mm IX	404,10	2,66
NU01-22(T2), 32-16 mm X	416,85	6,27
NU01-35(T2), 32-16 mm I	464,60	7,64
NU01-35(T2), 32-16 mm II	495,71	4,22
NU01-35(T2), 32-16 mm III	462,66	4,56
NU01-35(T2), 32-16 mm IV	463,68	5,86
NU01-35(T2), 32-16 mm V	378,01	43,62
NU01-35(T2), 32-16 mm VI	446,73	4,17
NU01-35(T2), 32-16 mm VII	439,22	4,85
NU01-34(T2), 32-16 mm I	477,10	7,97
NU01-34(T2), 32-16 mm II	461,57	4,39
NU01-34(T2), 32-16 mm III	470,56	3,42
NU01-34(T2), 32-16 mm IV	513,13	3,16
NU01-34(T2), 32-16 mm V	498,55	4,99
NU01-34(T2), 32-16 mm VI	468,61	6,21
NU01-34(T2), 32-16 mm VII	536,22	41,73
NU01-34(T2), 32-16 mm VIII	422,28	4,65
NU01-34(T2), 32-16 mm IX	455,22	3,99
NU01-34(T2), 32-16 mm X	468,61	5,13
NU01-33(T2), 32-16 mm I	424,41	4,35
NU01-33(T2), 32-16 mm II	340,67	7,15
NU01-33(T2), 32-16 mm III	514,13	7,37
NU01-33(T2), 32-16 mm IV	421,03	5,23
NU01-33(T2), 32-16 mm V	468,78	4,13
NU01-32(T2), 32-16 mm I	311,02	1,78
NU01-32(T2), 32-16 mm II	257,08	1,66
NU01-32(T2), 32-16 mm III	460,63	12,21
NU01-32(T2), 32-16 mm IV	335,08	6,19
NU01-32(T2), 32-16 mm V	267,77	1,85
NU01-32(T2), 32-16 mm VI	294,93	6,28
NU01-32(T2), 32-16 mm VII	250,65	6,95
NU01-32(T2), 32-16 mm VIII	238,48	3,13
NU01-32(T2), 32-16 mm IX	273,25	1,53
NU01-32(T2), 32-16 mm X	313,11	1,20

A-2-6g: Density of all pumice type 2 clasts analyzed.

Sample number	Density av. (kg/m³)	Stddev. (kg/m³)
NU01-31(T2), 32-16 mm I	500,57	15,68
NU01-31(T2), 32-16 mm II	530,46	107,40
NU01-31(T2), 32-16 mm III	478,02	6,10
NU01-31(T2), 32-16 mm IV	454,70	7,81
NU01-31(T2), 32-16 mm V	584,54	16,32
NU01-31(T2), 32-16 mm VI	497,12	15,79
NU01-31(T2), 32-16 mm VII	511,83	7,27
NU01-31(T2), 32-16 mm VIII	489,50	14,18
NU01-31(T2), 32-16 mm IX	479,64	8,57
NU01-31(T2), 32-16 mm X	492,36	10,64
NU01-30(T2), 32-16 mm I	585,50	8,41
NU01-30(T2), 32-16 mm II	470,75	6,34
NU01-30(T2), 32-16 mm III	437,29	8,37
NU01-30(T2), 32-16 mm IV	447,69	14,01
NU01-30(T2), 32-16 mm V	493,35	12,88
NU01-30(T2), 32-16 mm VI	462,49	6,66
NU01-30(T2), 32-16 mm VII	449,81	7,39
NU01-30(T2), 32-16 mm VIII	496,86	6,35
NU01-30(T2), 32-16 mm IX	463,90	9,77
NU01-30(T2), 32-16 mm X	482,56	5,26
NU01-28(T2), 32-16 mm I	447,50	10,06
NU01-28(T2), 32-16 mm II	480,22	6,36
NU01-28(T2), 32-16 mm III	444,92	5,21
NU01-28(T2), 32-16 mm IV	438,51	5,68
NU01-28(T2), 32-16 mm V	416,12	11,56
NU01-28(T2), 32-16 mm VI	474,13	5,10
NU01-27(T2), 32-16 mm I	503,78	6,46
NU01-27(T2), 32-16 mm II	307,80	2,02
NU01-27(T2), 32-16 mm III	310,21	2,16
NU01-27(T2), 32-16 mm VI	317,79	2,53
NU01-27(T2), 32-16 mm V	397,02	2,40
NU01-27(T2), 32-16 mm VI	319,64	2,70
NU01-27(T2), 32-16 mm VII	314,10	7,27
NU01-27(T2), 32-16 mm VIII	432,57	3,83
NU01-27(T2), 32-16 mm IX	284,13	11,00
NU01-27(T2), 32-16 mm X	304,31	3,17

A-2-6h: Density of all pumice type 2 clasts analyzed.

Sample number	Density av. (kg/m³)	Stddev. (kg/m³)
NU01-23(T2), 32-16 mm I	323,97	5,71
NU01-23(T2), 32-16 mm II	521,11	7,40
NU01-23(T2), 32-16 mm III	514,44	13,47
NU01-23(T2), 32-16 mm IV	452,91	2,62
NU01-23(T2), 32-16 mm V	445,80	3,30
NU01-23(T2), 32-16 mm VI	484,76	3,89
NU01-23(T2), 32-16 mm VII	492,65	8,92
NU01-23(T2), 32-16 mm VIII	480,18	9,51
NU01-23(T2), 32-16 mm IX	505,65	8,91
NU01-23(T2), 32-16 mm X	431,69	4,10
NU01-42(T2), 32-16 mm I	314,27	13,51
NU01-42(T2), 32-16 mm II	440,09	2,38
NU01-43(T2), 32-16 mm I	415,44	5,12
NU01-43(T2), 32-16 mm II	414,55	7,44
NU01-43(T2), 32-16 mm III	469,81	4,77

A-2-6i: Density of all pumice type 3 clasts analyzed.

Sample number	Density av. (kg/m³)	Stddev. (kg/m³)
NU01-14(T3), >32 mm	597,45	15,96
NU01-14(T3), 32-16 mm I	576,26	42,73
NU01-14(T3), 32-16 mm II	324,87	3,76
NU01-14(T3), 32-16 mm III	722,42	7,06
NU01-14(T3), 32-16 mm IV	323,13	2,11
NU01-14(T3), 32-16 mm V	1086,91	25,69
NU01-14(T3), 32-16 mm VI	314,78	2,69
NU01-14(T3), 32-16 mm VII	327,51	2,45
NU01-14(T3), 32-16 mm VIII	397,13	4,60
NU01-14(T3), 32-16 mm IX	388,27	2,40
NU01-14(T3), 32-16 mm X	333,36	3,62
NU01-21(T3), 32-16 mm I	573,41	44,18
NU01-21(T3), 32-16 mm II	547,66	1,30
NU01-21(T3), 32-16 mm III	901,79	7,51
NU01-21(T3), 32-16 mm IV	390,57	3,15
NU01-21(T3), 32-16 mm V	711,16	8,01
NU01-21(T3), 32-16 mm VI	496,55	4,55
NU01-21(T3), 32-16 mm VII	342,05	3,43
NU01-21(T3), 32-16 mm VIII	304,53	1,58
NU01-21(T3), 32-16 mm IX	366,63	2,09
NU01-21(T3), 32-16 mm X	386,95	16,60

A-2-6j: Density of all pumice type 3 clasts analyzed.

Sample number	Density av. (kg/m³)	Stddev. (kg/m³)
NU01-22(T3), 32-16 mm I	775,44	23,29
NU01-22(T3), 32-16 mm II	323,36	3,71
NU01-22(T3), 32-16 mm III	929,80	22,06
NU01-22(T3), 32-16 mm IV	842,19	12,59
NU01-22(T3), 32-16 mm V	905,66	22,45
NU01-22(T3), 32-16 mm VI	757,26	27,82
NU01-22(T3), 32-16 mm VII	795,71	10,08
NU01-22(T3), 32-16 mm VIII	899,37	16,98
NU01-22(T3), 32-16 mm IX	815,30	33,03
NU01-22(T3), 32-16 mm X	857,67	28,61
NU01-35(T3), 32-16 mm I	943,44	9,57
NU01-35(T3), 32-16 mm II	912,85	18,21
NU01-35(T3), 32-16 mm III	974,89	4,36
NU01-34(T3), 32-16 mm I	854,09	13,76
NU01-34(T3), 32-16 mm II	782,57	18,23
NU01-34(T3), 32-16 mm III	935,95	39,73
NU01-33(T3), 32-16 mm I	734,56	26,64
NU01-33(T3), 32-16 mm II	740,89	4,41
NU01-33(T3), 32-16 mm III	489,42	30,35
NU01-33(T3), 32-16 mm IV	735,35	12,77
NU01-32(T3), 32-16 mm I	345,93	2,04
NU01-32(T3), 32-16 mm II	302,55	7,94
NU01-32(T3), 32-16 mm III	398,74	2,47
NU01-32(T3), 32-16 mm IV	405,85	9,18
NU01-32(T3), 32-16 mm V	390,98	30,46
NU01-32(T3), 32-16 mm VI	323,34	3,54
NU01-30(T3), 32-16 mm I	647,63	29,57
NU01-30(T3), 32-16 mm II	815,84	36,22
NU01-30(T3), 32-16 mm III	869,27	15,90
NU01-30(T3), 32-16 mm IV	612,42	22,10
NU01-30(T3), 32-16 mm V	802,69	12,08
NU01-30(T3), 32-16 mm VI	696,31	27,31
NU01-27(T3), 32-16 mm I	654,60	4,70
NU01-27(T3), 32-16 mm II	467,43	7,22
NU01-27(T3), 32-16 mm III	458,76	6,02
NU01-27(T3), 32-16 mm IV	473,70	11,12
NU01-40(T3), 32-16 mm I	467,79	3,31
NU01-40(T3), 32-16 mm II	332,66	6,05
NU01-40(T3), 32-16 mm III	392,20	15,76
NU01-40(T3), 32-16 mm IV	345,46	3,41
NU01-40(T3), 32-16 mm V	504,20	10,98

A-2-6k: Density of all pumice type 3 clasts analyzed.

Sample number	Density av. (kg/m³)	Stddev. (kg/m³)
NU01-41(T3), 32-16 mm I	516.25	4.41
NU01-41(T3), 32-16 mm II	472.60	6.43
NU01-41(T3), 32-16 mm III	410.76	5.30
NU01-41(T3), 32-16 mm IV	379.18	5.16
NU01-41(T3), 32-16 mm V	518.35	4.89

A-2-6l: Density of all pumice type 4 clasts analyzed.

Sample number	Density av. (kg/m³)	Stddev. (kg/m³)
NU01-14(T4), >32 mm	1685,05	35,64
NU01-14(T4), 32-16 mm I	1092,72	51,06
NU01-14(T4), 32-16 mm II	846,15	11,14
NU01-14(T4), 32-16 mm III	1112,43	14,48
NU01-14(T4), 32-16 mm IV	980,83	5,33
NU01-14(T4), 32-16 mm V	836,59	7,31
NU01-14(T4), 32-16 mm VI	1145,39	23,66
NU01-14(T4), 32-16 mm VII	865,86	5,77
NU01-14(T4), 32-16 mm VIII	579,51	5,51
NU01-14(T4), 32-16 mm IX	884,04	7,60
NU01-14(T4), 32-16 mm X	861,39	2,03
NU01-21(T4), >32 mm	1063,61	28,47
NU01-21(T4), 32-16 mm I	1301,87	45,66
NU01-21(T4), 32-16 mm II	851,72	1,30
NU01-21(T4), 32-16 mm III	753,65	5,42
NU01-21(T4), 32-16 mm IV	944,03	2,43
NU01-21(T4), 32-16 mm V	988,59	2,99
NU01-21(T4), 32-16 mm VI	980,93	5,62
NU01-21(T4), 32-16 mm VII	977,19	4,84
NU01-21(T4), 32-16 mm VIII	966,23	9,59
NU01-21(T4), 32-16 mm IX	1032,03	13,65
NU01-21(T4), 32-16 mm X	1055,26	3,75
NU01-22(T4), 32-16 mm I	1049,63	32,02
NU01-22(T4), 32-16 mm II	1262,53	18,71
NU01-22(T4), 32-16 mm III	1115,22	30,59
NU01-22(T4), 32-16 mm IV	1246,90	50,42
NU01-22(T4), 32-16 mm V	1387,64	36,82
NU01-22(T4), 32-16 mm VI	996,20	4,50
NU01-22(T4), 32-16 mm VII	1238,14	30,45
NU01-22(T4), 32-16 mm VIII	1544,67	37,80
NU01-22(T4), 32-16 mm IX	1,34	1,33
NU01-22(T4), 32-16 mm X	0,98	0,99

A-2-6m: Density of all pumice type 5 clasts analyzed.

Sample number	Density av. (kg/m³)	Stddev. (kg/m³)
NU01-32 (T5) 32-16 mm I	794,84	34,71
NU01-32 (T5) 32-16 mm II	443,71	3,35
NU01-32 (T5) 32-16 mm III	281,20	2,28
NU01-32 (T5) 32-16 mm IV	693,46	17,52
NU01-32 (T5) 32-16 mm V	539,91	15,05
NU01-31 (T5) 32-16 mm I	499,09	5,39
NU01-31 (T5) 32-16 mm II	503,23	9,89
NU01-31 (T5) 32-16 mm III	517,69	7,43
NU01-31 (T5) 32-16 mm IV	463,08	9,46
NU01-30 (T5) 32-16 mm I	867,50	25,88
NU01-30 (T5) 32-16 mm II	888,87	42,23
NU01-30 (T5) 32-16 mm III	903,68	21,40
NU01-30 (T5) 32-16 mm IV	822,78	43,92
NU01-30 (T5) 32-16 mm V	795,95	29,63
NU01-27 (T5) 32-16 mm I	416,40	14,07
NU01-27 (T5) 32-16 mm II	453,41	7,95
NU01-27 (T5) 32-16 mm III	359,61	5,10
NU01-27 (T5) 32-16 mm IV	415,25	4,07
NU01-40 (T5) 32-16 mm I	901,89	21,53
NU01-40 (T5) 32-16 mm II	885,66	14,90
NU01-40 (T5) 32-16 mm III	881,72	11,94
NU01-40 (T5) 32-16 mm IV	926,41	37,85
NU01-40 (T5) 32-16 mm V	453,87	6,47
NU01-40 (T5) 32-16 mm VI	636,53	22,01
NU01-40 (T5) 32-16 mm VII	761,53	16,42
NU01-41 (T5) 32-16 mm I	692,86	15,38
NU01-41 (T5) 32-16 mm II	898,85	27,72
NU01-41 (T5) 32-16 mm III	748,86	20,61
NU01-41 (T5) 32-16 mm IV	818,19	16,71
NU01-41 (T5) 32-16 mm V	660,02	24,84
NU01-41 (T5) 32-16 mm VI	766,58	23,34
NU01-41 (T5) 32-16 mm VII	765,74	17,82
NU01-41 (T5) 32-16 mm VIII	798,56	23,75
NU01-41 (T5) 32-16 mm IX	892,04	23,30
NU01-41 (T5) 32-16 mm X	794,77	19,33
NU01-42 (T5) 32-16 mm I	446,88	18,39
NU01-42 (T5) 32-16 mm II	919,01	15,60
NU01-42 (T5) 32-16 mm III	708,27	20,05
NU01-42 (T5) 32-16 mm IV	722,39	13,49
NU01-42 (T5) 32-16 mm V	884,50	16,65
NU01-42 (T5) 32-16 mm VI	732,39	25,20

A-2-6n: Density of all pumice type 5 clasts analyzed.

Sample number	Density av. (kg/m³)	Stddev. (kg/m³)
NU01-43 (T5) 32-16 mm I	803,38	13,37
NU01-43 (T5) 32-16 mm II	644,38	12,56
NU01-43 (T5) 32-16 mm III	527,36	29,13
NU01-43 (T5) 32-16 mm IV	907,37	6,33
NU01-43 (T5) 32-16 mm V	822,98	22,51
NU01-43 (T5) 32-16 mm VI	774,71	29,25
NU01-43 (T5) 32-16 mm VII	433,70	17,42
NU01-43 (T5) 32-16 mm VIII	765,13	21,69
NU01-43 (T5) 32-16 mm IX	689,73	16,65
NU01-43 (T5) 32-16 mm X	686,14	24,44
NU01-44 (T5) 32-16 mm I	783,97	6,97
NU01-44 (T5) 32-16 mm II	775,42	48,50
NU01-44 (T5) 32-16 mm III	650,24	33,80
NU01-44 (T5) 32-16 mm IV	807,37	25,26
NU01-44 (T5) 32-16 mm V	865,52	25,74
NU01-44 (T5) 32-16 mm VI	867,84	10,44
NU01-44 (T5) 32-16 mm VII	828,40	16,38
NU01-44 (T5) 32-16 mm VIII	924,86	8,43
NU01-44 (T5) 32-16 mm IX	732,79	26,43
NU01-45 (T5) 32-16 mm I	826,48	19,64
NU01-45 (T5) 32-16 mm II	673,70	19,91

A-2-6o: Average density of all pumice type 1 clasts of each bed of LST.

Sample number	Density av. (kg/m³)	Stddev. (kg/m³)
NU01-14(T1)	394.20	119.35
NU01-21(T1)	412.58	80.02
NU01-22(T1)	331.80	38.83
NU01-35(T1)	363.31	24.72
NU01-34(T1)	334.25	42.54
NU01-33(T1)	327.96	66.52
NU01-31(T1)	332.88	67.68
NU01-30(T1)	363.10	76.70
NU01-28(T1)	306.68	35.55
NU01-27(T1)	350.23	36.81
NU01-25(T1)	304.00	3.41
NU01-23(T1)	281.80	48.69
NU01-40(T1)	317.05	18.65
NU01-41(T1)	303.08	37.24
NU01-42(T1)	304.00	41.65
NU01-44(T1)	285.16	26.33

A-2-6p: Average density of all pumice type 2 clasts of each bed of LST.

Sample number	Density av. (kg/m³)	Stddev. (kg/m³)
NU01-14(T2)	568.20	245.04
NU01-21(T2)	526.34	153.06
NU01-22(T2)	503.20	166.59
NU01-35(T2)	450.09	36.42
NU01-34(T2)	477.18	31.91
NU01-33(T2)	433.81	64.42
NU01-32(T2)	300.20	64.26
NU01-31(T2)	501.87	35.44
NU01-30(T2)	479.02	42.19
NU01-28(T2)	450.23	23.69
NU01-27(T2)	349.13	71.27
NU01-23(T2)	465.32	57.87
NU01-42(T2)	377.18	88.97
NU01-43(T2)	433.26	31.65

A-2-6q: Average density of all pumice type 3 clasts of each bed of LST.

Sample number	Density av. (kg/m³)	Stddev. (kg/m³)
NU01-14(T3)	490.19	241.88
NU01-21(T3)	502.13	188.37
NU01-22(T3)	790.18	173.81
NU01-35(T3)	943.73	31.02
NU01-34(T3)	857.53	76.75
NU01-33(T3)	675.05	123.79
NU01-32(T3)	361.23	43.35
NU01-30(T3)	740.69	103.06
NU01-27(T3)	513.62	94.18
NU01-40(T3)	408.46	75.27
NU01-41(T3)	459.43	62.62

A-2-6r: Average density of all pumice type 4 clasts of each bed of LST.

Sample number	Density av. (kg/m³)	Stddev. (kg/m³)
NU01-14(T4)	990.00	280.85
NU01-21(T4)	992.28	136.59
NU01-22(T4)	1216.31	182.81

A-2-6s: Average density of all pumice type 5 clasts of each bed of LST.

Sample number	Density av. (kg/m³)	Stddev. (kg/m³)
NU01-32 (T5)	550.62	202.60
NU01-31 (T5)	495.77	23.21
NU01-30 (T5)	855.76	45.27
NU01-27 (T5)	411.17	38.67
NU01-40 (T5)	778.23	175.62
NU01-41 (T5)	783.65	75.95
NU01-42 (T5)	735.57	167.39
NU01-43 (T5)	705.49	142.38
NU01-44 (T5)	804.04	81.40
NU01-45 (T5)	750.09	108.03

A-2-6t: Weighted average of all pumice types of LST

Sample number	Density (kg/m³)	stddev. (kg/m³)
NU01-14	725.10	230.12
NU01-21	683.07	137.64
NU01-22	690.03	116.01
NU01-35	632.72	31.23
NU01-34	429.11	41.10
NU01-33	472.45	85.42
NU01-32	321.28	57.04
NU01-31	480.35	73.40
NU01-30	412.58	61.28
NU01-28	406.53	32.89
NU01-27	381.68	58.17
NU01-25	304.00	3.41
NU01-23	281.80	48.69
NU01-40	574.70	113.19
NU01-41	549.75	60.64
NU01-42	650.82	129.34
NU01-43	521.67	100.79
NU01-44	654.33	65.51
NU01-45	750.09	108.03

A-2-7: Shape parameters (formfactor, solidity and elongation) averages for each bed of LST.

	Formfactor		Solidity		Elongation	
Sample No.	**Averages**	**Stddev.**	**Averages**	**Stddev.**	**Averages**	**Stddev.**
NU01-14	0.890	0.047	0.919	0.029	1.395	0.196
NU01-21	0.821	0.066	0.881	0.048	1.501	0.263
NU01-22	0.866	0.060	0.902	0.037	1.392	0.196
NU01-35	0.901	0.045	0.949	0.018	1.384	0.195
NU01-34	0.902	0.044	0.951	0.015	1.404	0.214
NU01-33	0.912	0.043	0.957	0.012	1.383	0.182
NU01-32	0.914	0.043	0.956	0.015	1.382	0.184
NU01-31	0.902	0.046	0.954	0.013	1.394	0.171
NU01-30	0.904	0.052	0.955	0.016	1.393	0.189
NU01-28	0.894	0.048	0.955	0.016	1.435	0.203
NU01-27	0.901	0.059	0.953	0.016	1.365	0.215
NU01-25	0.909	0.048	0.957	0.016	1.381	0.184
NU01-23	0.914	0.039	0.961	0.009	1.397	0.189
NU01-36	0.920	0.048	0.960	0.012	1.361	0.227
NU01-37	0.917	0.037	0.960	0.014	1.357	0.152
NU01-38	0.890	0.073	0.953	0.028	1.475	0.269
NU01-40	0.825	0.087	0.932	0.033	1.595	0.364
NU01-41	0.899	0.050	0.961	0.014	1.471	0.247
NU01-42	0.910	0.044	0.960	0.012	1.424	0.197
NU01-43	0.900	0.053	0.958	0.016	1.470	0.214
NU01-44	0.904	0.052	0.962	0.011	1.454	0.231
NU01-45	0.900	0.051	0.958	0.014	1.439	0.250

A-2-8: Chemical composition of the LST (major elements calculated on water free basis) after Wörner and Schmincke (1984)

LST STAGE		LLST	LLST	MLST	MLST	MLST
Sample No		1002	1017	1034	1044	1050
ıtigrafic stage		LLSTa	LLSTf	Stage II	Stage VII	stage X
SiO_2	wt%	56.64	58.48	59.52	59.72	59.62
TiO_2	wt%	0.12	0.17	0.28	0.48	0.61
Al_2O_3	wt%	20.93	21.59	20.60	20.05	19.84
Fe_2O_3	wt%	1.87	1.36	1.55	1.77	1.76
FeO	wt%	0.49	0.39	0.62	0.98	1.14
MnO	wt%	0.53	0.09	0.22	0.19	0.14
MgO	wt%	0.23	0.12	0.19	0.32	0.44
CaO	wt%	1.15	0.89	1.45	1.88	2.38
Na_2O	wt%	12.18	11.11	8.90	7.62	6.72
K_2O	wt%	5.83	5.76	6.62	6.89	7.23
P_2O_5	wt%	0.03	0.04	0.05	0.09	0.12
H_2O	wt%	2.10	2.70	2.10	2.70	2.00
CO_2	wt%	0.04	0.02	0.02	0.02	0.01
Cl	wt%	0.26	0.33	0.30	0.27	0.23
F	wt%	0.70	0.40	0.21	0.14	0.11
S	wt%	0.03	0.04	0.04	0.12	0.16
Cr	ppm	5	5	5	5	6
Co	ppm	4	16	5	23	11
Ni	ppm	7	6	6	3	4
Cu	ppm	49	75	25	51	21
Zn	ppm	309	209	126	114	76
Rb	ppm	712	464	322	216	168
Sr	ppm	5	35	60	274	468
Y	ppm	43	28	22	21	21
Zr	ppm	2614	1407	854	550	400
Nb	ppm	413	235	161	135	120
Ba	ppm	20	47	49	199	556

Appendix B – Model calculations and velocity profiles

B-1-1 Minoan eruption velocity profiles

B-2-1 Laacher See velocity profiles

B-1-1: Velocity profiles of the upper 1000 m of the MIN-A conduit models.

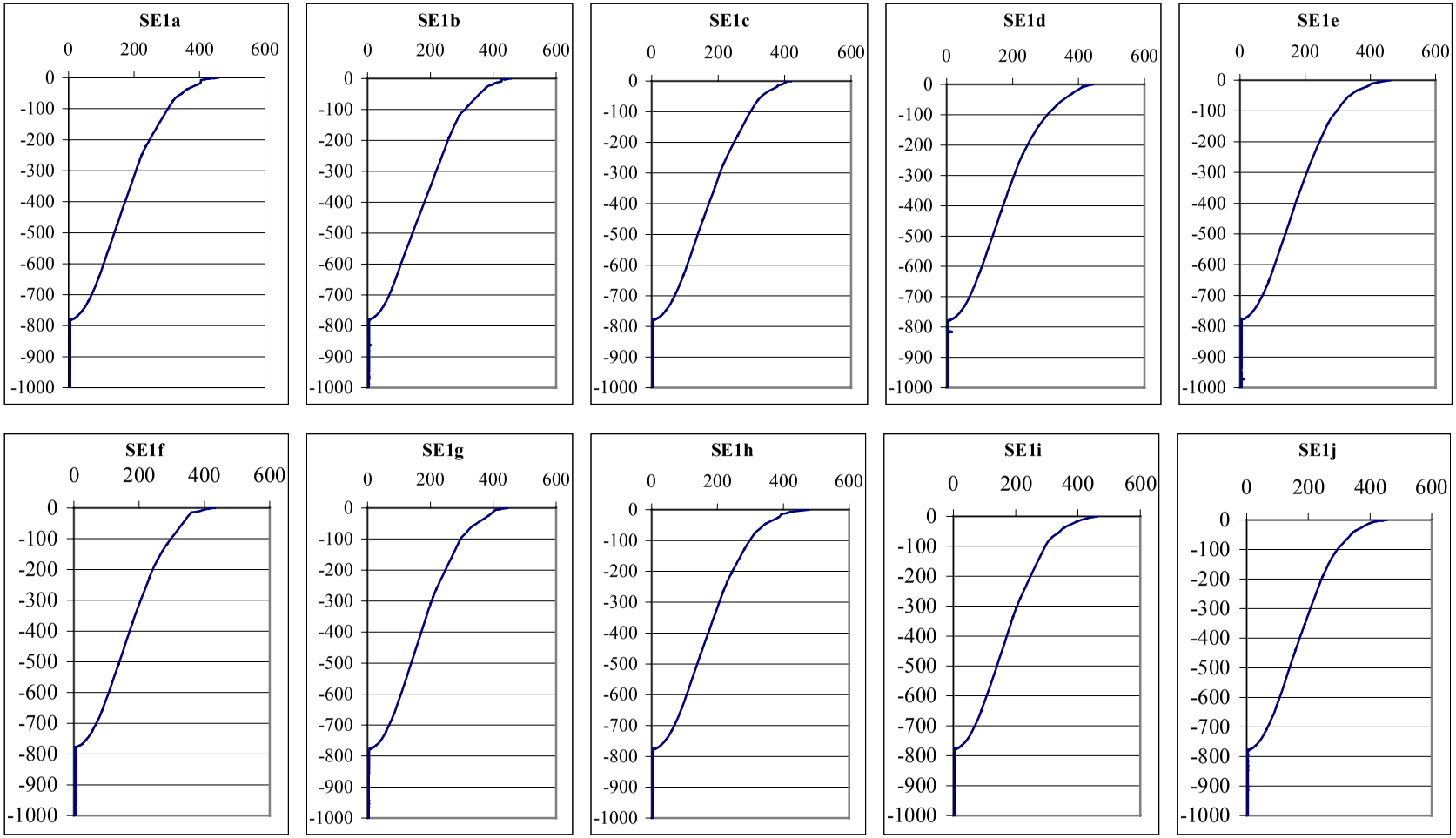

B-2-1: Velocity profiles of the upper 600 m of the LST conduit models.